Three dimensional SPH numerical modeling of a bar/rip channel system and turbulent vortex structures under broken water waves in the surf zone region

by

Rozita Jalali Farahani

A dissertation submitted to The Johns Hopkins University in conformity with the requirements for the degree of Doctor of Philosophy.

Baltimore, Maryland

December, 2013

Abstract

A Lagrangian numerical method called Smoothed Particle Hydrodynamics (SPH) is used to analyze two different coastal problems. The first problem is a simplified bar/rip channel system on a beach. Prior studies have shown that SPH models propagating water waves well, including breaking waves; here we show that the SPH also models the mean wave-induced near-shore circulation created by breaking waves. Model predictions are compared to the previous laboratory measurements and show good agreement, including mean velocity profiles, mean surface elevation, and cross-shore velocity components over the rip channel. The alongshore variation of different components of radiation stress and the resulting alongshore force that acts as a feeder for the rip current are obtained from the numerical results. The second problem concerns numerical modeling of water waves in the surf zone and related three dimensional turbulent vortical structures generated under the broken waves. The 3D SPH method is used to model solitary waves both spilling and plunging and the numerical model predicts water surface evolution as well as horizontal velocity very well in comparison with the experimental results. In case of spilling solitary

ABSTRACT

wave, the numerical results show organized coherent structures characterized as reversed horseshoe (hairpin) vortices, traveling downward and they appear to be the previously found obliquely descending eddies. The reversed horseshoe structures are associated with the turbulence motion of sweep events (downwelling motion). These reversed horseshoe coherent structures transport momentum and turbulent kinetic energy downward into the water column and likely have a significant role in bed and beach erosion. The mechanism of the generation of large-scale reversed horseshoe structures from the spanwise roller and the vortex stretching are studied. Vortex stretching and vortex bending play an important role on the generation and evolution of reversed horseshoe structures. In case of a plunging solitary wave, the vortex structures are generated under the broken wave and are carried towards the shore by the run-up but no reversed horseshoe structure is observed at the back of the broken wave. Periodic plunging waves are also numerically modeled using 3D SPH method. Three types of vortex structures are detected under broken periodic plunging waves: (1) horizontal rollers with axis of rotation parallel to the waves; (2) vertical counter-rotating vortex structures at the toe of the plunging jets (Known as downbursts); (3) reversed horseshoe structures at the back of the broken waves.

Acknowledgments

I would like to thank my advisor Dr. Robert A. Dalrymple for his invaluable insights and support throughout my doctoral research. He constantly guided me and provided me with an exceptional mentoring. I always look up to him for his deep knowledge in science as well as his professional and sincere manners.

I am thankful to Dr. Alexis Hérault for extending an invitation to work with him at Conservatoire National des Arts et Métiers and Istituto Nazionale di Geofisica e Vulcanologia, Sezione di Catania, Osservatorio Etneo. I would also like to extend my thanks to Dr. Giuseppe Bilotta and Dr. Eugenio Rustico for valuable discussions on GPUSPH model and GPU parallel programming. I am grateful to Dr. Billy Edge for inviting me to his workshops on smoothed particle hydrodynamics method. I had the pleasure to meet people working on various projects and have fruitful collaborations.

I would like to thank Dr. Tak Igusa and Dr. Jamie Guest for agreeing to be in my thesis committee and for constantly providing scientific insights during my doctoral research. I would also thank Dr. Behzad Ataie Ashtiani who introduced me to the smoothed particle hydrodynamics method during my master's dissertation at Sharif

ACKNOWLEDGMENTS

University and encouraged me to pursue my education.

I am greatly thankful to Debbie Lantry, Lisa Wetzelberger, LaTanya Waith, and Vessela Vassileva-Clarke for their kind assistance with departmental procedures during my doctoral program at Johns Hopkins University.

I would like to thank my friends and labmates Younes, Muthukumar, Varjola for their constant support and encouragement during these years. I would also like to thank Xiaobo, Brian, Noura, and Xiaoyu who have been great friends and labmates.

I am extremely grateful to Leili, Arghavan, Mazdak, Bahman, Mohsen, and Akrita who became my first friends in Baltimore and constantly helped me through different stages. I would like to extend my thanks to my great friends Zoya, Shiva, Shadi, Mehdi, Arash, Sahar, Reza, Maral, Hooman, Daniel, Hyeyun, and Vahid who always warm my heart with their exceptional kindness.

I would like to extend my great respect to the scientists and developers all around the world who offer open-source scientific models such as GPUSPH and high quality tools such as GNU/Linux, LATEX, and ParaView, with universal access via free license. These people were greatly influential in my research and I admire their great work as well as their free sharing approaches.

Dedication

To my parents Mrs. Farideh Nabiyouni and Mr. Ali Jalali Farahani who always valued education and taught me determination, hard work, patience, modesty, integrity, and honesty and to my inspirational sisters Mrs. Bahar Jalali Farahani and Mrs. Sahar Jalali Farahani and to my lovely nephew Alborz Khorsandi.

Contents

List of Tables

List of Figures

Chapter 1

Introduction

1.1 Motivations

This dissertation addresses the three-dimensional numerical modeling of coastal processes including rip current system due to alongshore variation of bed bathymetry, water waves breaking in the surf zone, and the three-dimensional vortex structures that are generated after the waves are broken.

A rip current is "a strong water-surface current of shore duration flowing seaward from the shore" as defined in the Glossary of Meteorology (1959). Rip currents accounted for more than 80% of lifeguard rescues in Florida, United States, and are considered as a natural hazard for swimmers and beach goers (Lushine, 1991, MacMahan et al., 2005, Dalrymple et al. 2011). Lushine (1991) reported that many drownings, specially along the Gulf of Mexico beaches and United States east coast

regions, occur when a person gets trapped in a rip current system due to nearshore sand bars and pulled into deeper water by the rip current. He also reported that an estimated 150 persons annually drown in rip currents in the United States.

Rip currents are created in a variety of ways that can be classified in three major classes: bathymetric variations, wave-wave interactions, and instabilities of alongshore currents and/or shear instabilities (Dalrymple et al., 2011). In this study, we focused on the rip currents created by the bathymetric variations. A 3D numerical model is investigated that presents one-half of a rip current system, represented by two sand bars with a rip channel in between (using symmetry about the sidewalls). The numerical method is called the Smoothed Particle Hydrodynamics (SPH) method, which is a mesh-free, Lagrangian particle method. The numerical bed bathymetry and the wave parameters are inspired by an experimental study performed by Drønen et al., 2002. The three-dimensional structure of flow, particle trajectories, and mean depth-averaged fluid properties are investigated.

Another topic studied in this dissertation is water waves breaking in the surf zone and the related three-dimensional coherent vortex structures, created under the broken waves. Wave breaking including tsunami wave breaking and the associated turbulence lead to three-dimensional vortex structures, which have a crucial role on sediment transportation, mixing processes beneath the free surface, and thermal diffusion. These three-dimensional vortex structures have an important effect on the safety of vessels and structures located in the surf zone (Banner and Peregrine, 1993).

First a solitary wave both spilling and plunging, which can be considered as a first approximation to a tsunami wave, is numerically studied using SPH method. Obliquely descending vortex structures in the form of horseshoe structures are detected at the back of the broken wave. Then periodic plunging waves are numerically modeled and related vortex structures are detected.

1.2 Objectives

The objectives of this study are:

1. Perform a three-dimensional numerical study of rip current systems due to alongshore bathymetry variations using the GPUSPH model. (http://www.ce.jhu.edu/dalrymple/GPUSPH/Home.html)

2. Study the mean wave-induced nearshore circulations, mean surface elevations, radiation stresses, and the alongshore force that acts as a feeder for the rip current.

3. Add necessary features to the existing GPUSPH model in order to study depth-averaged quantities as well as the three-dimensional structure of flow.

4. Compare the numerical results of rip current system with the experimental results of Drønen et al., (2002) in terms of mean velocities and the mean water surface elevations.

5. Study water particle trajectory tracking, three-dimensional velocity profiles as well as depth-averaged velocity and vorticity profiles to investigate the rip current flow and the nearshore circulations.

6. Perform a three-dimensional numerical study of solitary water waves both spilling and plunging in the surf zone area.

7. Detect coherent vortex structures under the broken waves and study the configuration of the vortex structures.

8. Investigate the evolution, propagation, and configuration of the coherent vortex structures under the broken waves by studying the vorticity equations.

9. Study the turbulent kinetic energy and turbulent momentum flux being transferred by the coherent vortex structures.

10. Compare the numerical results of the solitary broken wave with the experimental results of Ting 2006 in terms of mean velocity, water surface distribution, and turbulent velocities.

11. Perform a three-dimensional numerical study of periodic plunging water waves, breaking in the surf zone area and study the vortex structures that are generated under broken waves.

Chapter 2

Smoothed Particle Hydrodynamics Method

2.1 Introduction

The Smoothed Particle Hydrodynamics (SPH) numerical method, a Lagrangian, mesh-free particle method, was first introduced by Lucy (1977) and Gingold and Monaghan (1977) to solve gas dynamical problems of astronomical interest. SPH was developed as mesh-based methods were found to be unsuitable for problems with large deformations and lack of defined boundaries. Decades later SPH was used to model a vast range of fluid mechanics problems and was shown to be capable of modeling flows with complicated surface deformations. The computational domain is represented by numerous discrete particles that carry fluid parameters/variables

and have no predefined connectivity. Monaghan (1994) first modeled free surface problems using SPH and the Navier-Stokes equations. He implemented SPH to model a dam-break as well as water waves. Later SPH was used to model a wide range of free surface problems including wave-related problems such as solitary waves on beaches (Monaghan and Kos, 1999), Scott Russell's wave generator (Monaghan and Kos, 2000), breaking waves (Colagrossi and Landrini, 2003; Monaghan et al., 2003), impact of wave on structures (Dalrymple et al., 2002; Gómez-Gesteira and Dalrymple, 2004), wave overtopping on the offshore platforms (Gómez-Gesteira et al., 2005), and waves in the surf zone (Dalrymple and Rogers, 2006a). Various other applications are mentioned in Monaghan (2005) review paper.

This chapter presents the SPH formulation and mathematical representation. The discrete forms of three-dimensional Navier-Stokes equations in SPH representation and the corresponding boundary treatments are presented. The numerical considerations including XSPH correction, kernel renormalization, Shepard filtering, and linked-list neighboring particle search algorithm will be discussed.

2.2 SPH, a Lagrangian, mesh-free, particle method

Physical governing equations can be defined in two fundamental specifications: Eulerian method and Lagrangian method. Eulerian method has a spatial description,

where the governing equations are discretized by defining the value of parameters at computational fixed points in space. On the other hand, the Lagrangian method has a material description, where the parameters are defined at computational points or particles that are moving with the problem field. For instance, momentum equation in the fluid mechanics is written in an Eulerian description as:

$$\frac{\partial \vec{u}}{\partial t} + (\vec{u}.\nabla)\vec{u} = -\frac{1}{\rho}\nabla P + \vec{g} + \vec{\Theta} \tag{2.1}$$

where $\vec{u}$ is the velocity, P is the pressure, ρ is the density, $\vec{g}$ is the gravitational acceleration, and $\vec{\Theta}$ is the viscous term. In the Lagrangian description, the momentum equation is written as:

$$\frac{D\vec{u}}{Dt} = -\frac{1}{\rho}\nabla P + \vec{g} + \vec{\Theta} \tag{2.2}$$

where $\frac{D}{Dt}$ is the total time derivative and in Eulerian description, it consists of the local derivative and the convective derivative as:

$$\frac{D}{Dt} = \frac{\partial}{\partial t} + \vec{u}.\nabla \tag{2.3}$$

The local derivative $\frac{\partial}{\partial t}$ defines the time rate of change at a fixed point, while the convective derivative $\vec{u}.\nabla$ defines the change due to the movement of the fluid element from one location to the another location in the flow field. In the Lagrangian methods, the total derivative is computed and there is no need to compute the local and convective derivatives separately since the computational nodes or particles are moving with the fluid. This leads to simpler computational codes and no computational effort is necessary to deal with the nonlinear convective terms (G. R. Liu and

M. B. Liu, 2003). In addition, the time history of the field variables can be obtained more conveniently in the Lagrangian methods since a material point can be easily tracked.

Grid-based numerical methods such as Finite Difference Method (FDM) and Finite Element Method (FEM) have been widely used to model various problems. However, they suffer from some limitations and difficulties when modeling many problems. Mesh generation and mesh rezoning are computationally expensive especially for the problems with the free surfaces, large deformations, and deformable boundaries and may introduce additional inaccuracy into the problem solution. A number of mesh-free numerical methods have been introduced during the past decades among which Smoothed Particle Hydrodynamics (SPH) has been widely applied for various problems including solid and fluid mechanics problems. SPH belongs to mesh-free particle methods, which is a class of mesh-free methods that employ a set of discrete moving particles with no fixed connectivity to represent the problem domain. Particles possess the material properties and move according to the governing equations.

2.3 SPH formulations

In the SPH method, a kernel approximation is used to represent the integral form of the governing equations. However for numerical computation, the kernel approximation is then approximated at each discrete particle using summations over

all the corresponding values at the neighboring particles that are located with the support domain of the particle of interest. Using these approximations, the partial differential equations (PDEs) are converted to ordinary differential equations (ODEs) in discretized form with respect to time only. The ODEs are then solved using an integration algorithm for each time step and the field variables are computed for all the particles.

2.3.1 Integral representation of a function and kernel interpolation

Any arbitrary field $A(\vec{r}, t)$ can be defined as a spatial convolution product with the Dirac delta function as:

$$A(\vec{r}, t) = \int_{-\infty}^{+\infty} A(\vec{r'}, t)\delta(\vec{r'} - \vec{r})\,\mathrm{d}r' \tag{2.4}$$

Dirac delta function is approximated by a kernel interpolation function as $W(|\vec{r} - \vec{r'}|, h)$.

$$A(\vec{r}, t) \simeq A_c(\vec{r}, t) = \int_{\Omega_r} A(\vec{r'}, t)W(|\vec{r} - \vec{r'}|, h)\,\mathrm{d}r' \tag{2.5}$$

In this equation $A_c(\vec{r}, t)$ denote the interpolated field and Ω_r is the $\vec{r}$ point-centered domain where kernel function gives non-zero values. The parameter h is the smoothing length of the kernel function, which indicates the support domain of the kernel function. In order to determine the accuracy of this approximation, we use the Taylor

series expansion about the point $\vec{r}$.

$$A(\vec{r'},t) = A(\vec{r},t) + \frac{\partial A}{\partial r}(\vec{r'} - \vec{r}) + \mathcal{O}(|\vec{r'} - \vec{r}|^2) \tag{2.6}$$

Then this Taylor series is substituted in equation 2.5:

$$\begin{aligned} A_c(\vec{r},t) = A(\vec{r},t)\int_{\Omega_r} W(|\vec{r} - \vec{r'}|,h)\,\mathrm{d}r' - \frac{\partial A}{\partial r}\int_{\Omega_r}(\vec{r} - \vec{r'})W(|\vec{r} - \vec{r'}|,h)\,\mathrm{d}r' \\ + \int_{\Omega_r}\mathcal{O}(|\vec{r} - \vec{r'}|^2)W(|\vec{r} - \vec{r'}|,h)\,\mathrm{d}r' \end{aligned} \tag{2.7}$$

For the approximation of $A_c(\vec{r},t) \simeq A(\vec{r},t)$ to be accurate to the first order the following conditions should be satisfied (Violeau, 2012).

$$\int_{\Omega_r} W(|\vec{r} - \vec{r'}|,h)\,\mathrm{d}r' = 1 \tag{2.8}$$

and

$$\int_{\Omega_r}(\vec{r} - \vec{r'})W(|\vec{r} - \vec{r'}|,h)\,\mathrm{d}r' = 0 \tag{2.9}$$

The first condition is the normalization condition where indicates that the average of kernel function (similar to Dirac delta function) should be equal to one. For the second condition, we denote $\tilde{r} = \vec{r} - \vec{r'}$. Then applying a variable change as $\tilde{r'} = -\tilde{r}$ results in:

$$\begin{aligned} \int_{\Omega_r}\tilde{r}W(\tilde{r},h)\,\mathrm{d}\tilde{r} &= \int_{\Omega - r}\tilde{r'}W(\tilde{r'},h)\,\mathrm{d}\tilde{r'} \\ &= -\int_{\Omega_r}\tilde{r}W(-\tilde{r},h)\,\mathrm{d}\tilde{r} \end{aligned} \tag{2.10}$$

In the above equation if the symmetry condition of :

$$\forall\tilde{r}, W(\tilde{r},h) = W(-\tilde{r},h) \tag{2.11}$$

then the condition (2.9) is true. Equation (2.11) leads to an antisymmetry property of:

$$\nabla W(-\tilde{r}, h) = -\nabla W(\tilde{r}, h) \tag{2.12}$$

The gradient of a scalar field A can be approximated using equation (2.5):

$$\begin{aligned}[\nabla A]_c(\vec{r}, t) &= \int_{\Omega_r} \frac{\partial A(\vec{r'}, t)}{\partial \vec{r'}} W(|\vec{r} - \vec{r'}|, h)\, \mathrm{d}r' \\ &= \int_{\Omega_r} \frac{\partial}{\partial \vec{r'}} [A(\vec{r'}, t) W(|\vec{r} - \vec{r'}|, h)]\, \mathrm{d}r' \\ &\quad - \int_{\Omega_r} A(\vec{r'}, t) \frac{\partial W(|\vec{r} - \vec{r'}|, h)}{\partial \vec{r'}}\, \mathrm{d}r'\end{aligned} \tag{2.13}$$

Considering the property of (2.12) and turning the volume integral to a surface integral using Gauss theorem, we get:

$$\begin{aligned}[\nabla A]_c(\vec{r}, t) &= \oint_{\partial\Omega_r} A(\vec{r'}, t) W(|\vec{r} - \vec{r'}|, h) \vec{n}(\vec{r'})\, \mathrm{d}\Gamma \\ &\quad + \int_{\Omega_r} A(\vec{r'}, t) \frac{\partial W(|\vec{r} - \vec{r'}|, h)}{\partial \vec{r}}\, \mathrm{d}r'\end{aligned} \tag{2.14}$$

In the above equation $\partial\Omega_r$ is the surface surrounding our domain and $\vec{n}(\vec{r'})$ is the normal vector to surface $\partial\Omega_r$ at point r' directing to the outside. The first integral in (2.14) is computed on the boundary $\partial\Omega_r$ therefore, if point r is sufficiently far from the surrounding surface $\partial\Omega_r$, the boundary integral vanishes and (2.14) can be written as:

$$[\nabla A]_c(\vec{r}, t) = \int_{\Omega_r} A(\vec{r'}, t) \nabla_r W(|\vec{r} - \vec{r'}|, h)\, \mathrm{d}r' \tag{2.15}$$

From the property (2.12) one can conclude:

$$\int_{\Omega_r} \nabla_r W(|\vec{r} - \vec{r'}|, h)\, \mathrm{d}r' = 0 \tag{2.16}$$

The same process can be pursued to interpolate the divergence of a vector field $\vec{A}$ as:

$$[\nabla.\vec{A}]_c(\vec{r},t) = \int_{\Omega_r} \vec{A}(\vec{r'},t).\nabla_r W(|\vec{r}-\vec{r'}|,h)\,\mathrm{d}r' \tag{2.17}$$

2.3.2 Kernel interpolation functions

Kernel functions $W(|\vec{r}-\vec{r'}|,h)$, which are used as the interpolation functions in the SPH method, should support the following conditions:

1. Compact support: Kernel function should equals zero at a finite distance in order to be computationally feasible. The dimension of compact support is defined by the smoothing length h.

2. Normalization condition: This condition proposes that the kernel average should be equal to one (similar to Dirac delta function). This condition is mentioned in the equation (2.8) in order to gain first order accuracy.

3. Symmetry condition: Kernel function should be an even function.This condition is indicated in the equation (2.11) for first order accuracy.

4. Positivity condition: Kernel function should be positive for any point inside the support domain of the particle of interest. If the particle of interest is denoted by r and r' is any particle inside the support domain of particle r, then $W(|r-r'|,h) >= 0$.

5. Decay condition: The value of kernel function should monotonically decrease

with increasing distance from the particle of interest. Therefore the particles, which are closer to the particle of interest, contribute more than the particles that are far from the particle of interest.

6. Dirac delta function property: The kernel function should approach Dirac delta function as the smoothing length approaches to zero as $\lim_{h\to 0}(W|r-r'|,h) = \delta(|r-r'|)$.

7. Smoothness: The kernel function should be sufficiently smooth to provide continuous derivatives.

Different kernel functions have been used in the SPH literature. Lucy (1977) used the following bell-shaped function as the interpolation function:

$$W(q,h) = \alpha_D \begin{cases} (1+3q)(1-q)^3 & q \leq 1; \\ 0 & q > 1. \end{cases} \tag{2.18}$$

where α_D is equal to $5/(4h)$, $5/(\pi h^2)$ and $105/(16\pi h^3)$ for one, two and three dimensional space respectively. Parameter α_D is defined in a way that normalization condition can be satisfied. Parameter q is defined as $\frac{|\tilde{r}|}{h}$ where $|\tilde{r}|$ is the distance between the two particles.

Gingold and Monaghan (1977)used the following Gaussian kernel as the interpolation function:

$$W(q,h) = \alpha_D e^{-q^2} \tag{2.19}$$

where α_D is equal to $1/(\pi^{1/2}h)$, $1/(\pi h^2)$ and $1/(\pi^{3/2}h^3)$ for one, two and three dimensional space respectively to satisfy the normalization condition. This kernel doesn't go to zero theoretically unless q approaches to infinity but it goes to zero numerically so it can be assumed to have a compact support. However a longer distance may be needed for the kernel function to approach zero. Therefore a larger number of particles are considered as neighboring particles for the particle of interest and the computational expense may be increased.

Monaghan (1985) proposed the following cubic spline function as the interpolation function:

$$W(q,h) = \alpha_D \begin{cases} \frac{2}{3} - q^2 + \frac{1}{2}q^3 & 0 \leq q < 1; \\ \frac{1}{6}(2-q)^3 & 1 \leq q < 2; \\ 0 & q \geq 2. \end{cases} \tag{2.20}$$

where α_D is equal to $1/h$, $15/(7\pi h^2)$ and $3/(2\pi h^3)$ for one, two and three dimensional space respectively. This kernel has been used in several SPH studies. However, it is defined in different pieces, which makes it slightly more difficult to use in comparison to the one-piece functions. In addition, the second derivative of this kernel is a linear function. Therefore, the smoothness condition is not completely satisfied and may result into instability.

Morris (1996) proposed higher order (quartic and quintic) piecewise spline functions. The piecewise quartic function is defined as:

$$W(q,h) = \alpha_D \begin{cases} (q+2.5)^4 - 5(q+1.5)^4 + 10(q+0.5)^4 & 0 \le q < 0.5; \\ (2.5-q)^4 - 5(1.5-q)^4 & 0.5 \le q < 1.5; \\ (2.5-q)^4 & 1.5 \le q < 2.5; \\ 0 & q > 2.5. \end{cases} \tag{2.21}$$

where α_D is equal to $1/(24h)$ in one dimensional space. The piecewise quintic function is defined as:

$$W(q,h) = \alpha_D \begin{cases} (3-q)^5 - 6(2-q)^5 + 15(1-q)^5 & 0 \le q < 1; \\ (3-q)^5 - 6(2-q)^5 & 1 \le q < 2; \\ (3-q)^5 & 2 \le q < 3; \\ 0 & q > 3. \end{cases} \tag{2.22}$$

where α_D is equal to $120/h$, $7/(478\pi h^2)$ and $3/(359\pi h^3)$ for one, two and three dimensional space respectively. These functions still suffer from being in several pieces.

The Wendland kernel function (1995) has the advantage of being based on one algebraic equation and having a compact support.

$$W(q,h) = \alpha_D \begin{cases} (1-\frac{q}{2})^4(1+2q) & 0 \le q \le 2; \\ 0 & q > 2. \end{cases} \tag{2.23}$$

where α_D is equal to $3/(4h)$, $7/(4\pi h^2)$ and $21/(16\pi h^3)$ for one, two and three dimensional space respectively.

Johnson et al. (1996) used the following quadratic kernel function as the smoothing function.

$$W(q,h) = \alpha_D \begin{cases} \frac{3}{16}q^2 - \frac{3}{4}q - \frac{3}{4} & 0 \le q \le 2; \\ 0 & q > 2. \end{cases} \tag{2.24}$$

where α_D is equal to $1/h$, $2/(\pi h^2)$ and $5/(4\pi h^3)$ for one, two and three dimensional space respectively. Unlike other kernel functions, the first derivative of this kernel always increases as the particles approach each other and always decreases as the particles move apart. This characteristic was reported to improve the compressive instability. However, this function does not satisfy the smoothness condition completely.

In our study, the Wendland kernel function (1995) was chosen for the numerical computation. Figure 2.1 illustrate the Wendland kernel function and its first derivative. The kernel function has a maximum at zero and it decays as q increases. The first derivative of the kernel function is always negative and at first it decreases as q increases and reaches a minimum, then it increases and reaches zero value.

2.3.3 Discrete forms of governing equations

In the SPH method, a continuous medium is represented as a set of particles that carry kinematic and thermodynamic quantities of that medium. These particles have a fixed mass m_a and their volume can be defined as:

$$V_a = \frac{m_a}{\rho_a} \tag{2.25}$$

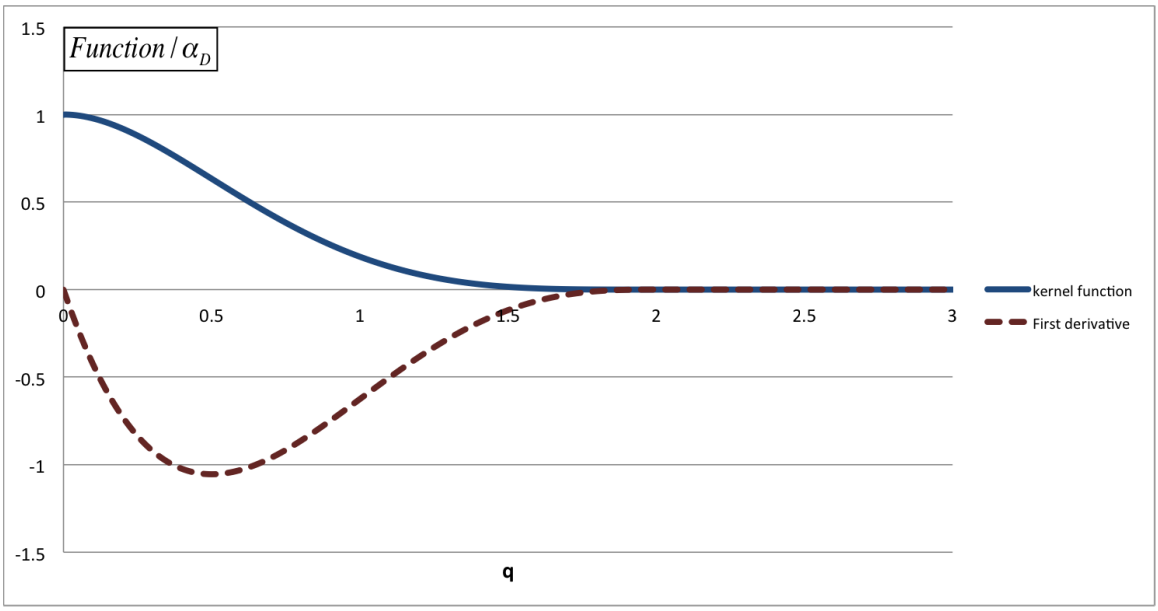

Figure 2.1: Wendland kernel function and its first derivative

(In the case of multi-fluid flows, the particle masses are constant for each fluid.) Particles are first introduced at the vertices of a grid and the initial distance between particles is defined as δp. This item is usually chosen first and the initial volume of the particles is calculated. Then the mass of particles is calculated using equation (2.25). The smoothing length of the kernel function, which was mentioned in the previous section, is defined using the initial particle spacing δp as:

$$\frac{h}{\delta p} = 1.0 \sim 2.0 \tag{2.26}$$

Each particle a located at $\vec{r_a}$ moves with a velocity $\vec{u_a}$:

$$\forall a, \frac{d\vec{r_a}}{dt} = \vec{u_a} \tag{2.27}$$

In order to discretize the equations, integrals are approximated through discrete sums using Riemann sum concept. Using equation 2.5 for a field A, the quantity $A_c(\vec{r}, t)$

at position $\vec{r}$ any field as A can be calculated as:

$$A_c(\vec{r},t) = \int_{\Omega_r} A(\vec{r'},t)W(|\vec{r}-\vec{r'}|,h)\,\mathrm{d}r' \simeq \sum_b A(\vec{r_b},t)W(|\vec{r}-\vec{r_b}|,h)V_b \tag{2.28}$$

If $\frac{h}{\delta p}$ increases, the number of particles involved in the sum estimation will increase and the statistical accuracy of this estimation will increase (Violeau, 2012). On the other hand, when h increases, particles, which are far from the particle of interest, are considered in the interpolation leading to greater errors. The reason is that as h decreases and approaches towards zero, the kernel function approaches a Dirac delta function and a better kernel approximation is achieved. Therefore, there exists two contradictory requirements of the smoothing length h here, where h should approach towards zero whereas $\frac{h}{\delta p}$ should tend towards infinity. Consequently, an optimal value for $\frac{h}{\delta p}$ needs to be considered. In our study this value is taken as $\frac{h}{\delta p} = 1.3$ (Monaghan, 2005).

2.3.3.1 Conversation of mass

The differential form of the conservation of mass equation is given as:

$$\frac{\partial \rho}{\partial t} + \rho(\nabla.\vec{u}) = 0 \tag{2.29}$$

The SPH approximation of divergence of a parameter $\vec{A}$ can be defined as (Monaghan, 1992):

$$\nabla.\vec{A} = \rho\nabla.(\frac{\vec{A}}{\rho}) + \frac{\vec{A}}{\rho}.\nabla(\rho) \tag{2.30}$$

Using the above equation, SPH form of conservation of mass equation can be written as:

$$\frac{\partial \rho_a}{\partial t} = -\rho_a \sum_b \frac{m_b}{\rho_b}(\vec{u}_a + \vec{u}_b)\nabla_a W(r_{ab}) \tag{2.31}$$

This form of SPH approximation can result in an artificial density decrease near the fluid interface. Therefore a new SPH form of conservation of mass equation was proposed by rewriting divergence of velocity as (Monaghan, 1994):

$$\frac{\partial \rho}{\partial t} + \nabla.(\rho\vec{u}) - \vec{u}\nabla\rho = 0 \tag{2.32}$$

Then the SPH form of conservation of mass equation can be written as:

$$\begin{aligned} \frac{\partial \rho_a}{\partial t} &= -\sum_b m_b \vec{u}_b \nabla_a W(r_{ab}) + \vec{u}_a \sum_b m_b \nabla_a W(r_{ab}) \\ &= \sum_b m_b(\vec{u}_a - \vec{u}_b)\nabla_a W(r_{ab}) \end{aligned} \tag{2.33}$$

The gradient of kernel function can be computed as:

$$\nabla_a W(r_{ab}) = W'(r_{ab})\frac{(\vec{r_a} - \vec{r_b})}{r_{ab}} \tag{2.34}$$

Particle density can also be calculated using the original SPH interpolation equation (2.28) as:

$$\rho_a = \sum_b m_b W(r_{ab}) \tag{2.35}$$

However, this approach leads to some stability problem specially for the free surfaces (Monaghan, 1994).

2.3.3.2 Conversation of momentum

The differential form of the momentum equation is given as:

$$\frac{D\vec{v}}{Dt} = -\frac{1}{\rho}\nabla P + \vec{g} + \vec{\Theta} \tag{2.36}$$

The first term on the right hand side of the above equation is the pressure gradient term that can be written as:

$$-\frac{1}{\rho}\nabla P = -[\nabla(\frac{P}{\rho}) + \frac{P}{\rho^2}\nabla\rho] \tag{2.37}$$

The SPH form of the pressure term is given as:

$$\begin{aligned} -[\sum_b (\frac{P_b}{\rho_b})\frac{m_b}{\rho_b}\nabla_a W(r_{ab}) + \frac{P_a}{\rho_a^2}\sum_b \rho_b \frac{m_b}{\rho_b}\nabla_a W(r_{ab})] = \\ -\sum_b (\frac{P_a}{\rho_a^2} + \frac{P_b}{\rho_b^2}) m_b \nabla_a W(r_{ab}) \end{aligned} \tag{2.38}$$

The second term on the right hand side of the equation (2.36) is the gravitational acceleration, which is defined as: $\vec{g} = (0, 0, 9.81)\frac{m}{s^2}$. The third term on the right hand side of the equation (2.36) is the viscous term that has been computed using several methods as follows:

(1) Artificial viscosity: Monaghan (1992) proposed the artificial viscosity where the diffusion term of the momentum equation is given as:

$$-\sum_b m_b \Pi_{ab} \nabla_a W(r_{ab}) \tag{2.39}$$

The term Π_{ab} represents the viscosity term that has the general form of:

$$\Pi_{ab} = \begin{cases} \frac{-\alpha \bar{c_{ab}} \mu_{ab}}{\bar{\rho_{ab}}} & \vec{v_{ab}} \cdot \vec{r_{ab}} < 0 \\ 0 & \vec{v_{ab}} \cdot \vec{r_{ab}} > 0 \end{cases} \tag{2.40}$$

where

$$\mu_{ab} = \frac{h\vec{v_{ab}} \cdot \vec{r_{ab}}}{\vec{r_{ab}}^{\,2} + \eta^2} \tag{2.41}$$

and $\vec{r_{ab}} = \vec{r_a} - \vec{r_b}$, $\vec{v_{ab}} = \vec{v_a} - \vec{v_b}$, c=speed of sound and the bar over it shows the average of speed of sound between two particles a and b ($\bar{c_{ab}} = \frac{c_a + c_b}{2}$). $\bar{\rho_{ab}}$ is the average of density between two particles a and b ($\bar{\rho_{ab}} = \frac{\rho_a + \rho_b}{2}$) Parameter $\eta^2 = 0.01h^2$ is chosen to prevent the denominator becoming zero. Parameter α is chosen according for each particular problem. Monaghan and Kos (1999) showed that the artificial viscosity is defined in a way that it will have the form of the viscous term of Navier-Stokes equations when the number of particles increases to infinity.

(2) Laminar viscosity: Morris et al. (1997) proposed the viscous term to be computed similar to the heat conduction term in Cleary and Monaghan (1999) studies. Lo and Shao (2002) used the same approach and discretized the viscous term as:

$$(\nu_0 \nabla^2 \vec{u})_a = \sum_b \frac{4m_b(\mu_a + \mu_b)\vec{r_{ab}}.\nabla_a W(r_{ab})}{(\rho_a + \rho_b)^2(|\vec{r_{ab}}|^2 + \eta^2)}(\vec{u_a} - \vec{u_b}) \tag{2.42}$$

where ν_0 is the kinetic viscosity of laminar flow.

(3) Laminar viscosity and Sub-Particle Scale (SPS) turbulence: In this approach the effect of turbulence is considered in the SPH method using a model similar to the Sub-Grid Scale (SGS) turbulence model in the Large Eddy Simulation (LES) method (Dalrymple and Rogers, 2006a). In LES method, large eddies are explicitly computed using governing equations (conservation of mass and conservation of momentum), while small eddies are implicitly accounted using a universal model. This method is based on the theory of self similarity that defines large eddies dependent on the

geometry and characteristics of the flow while small eddies act more universally. Large eddies are computed by applying a LES filter operator on the velocity field. Filtering kernel (G) is similar to a convolution operation that can be applied as:

$$\bar{u_i}(\vec{x},t) = \int u_i(\acute{x},t)G(x-\acute{x},t)d\acute{x} \tag{2.43}$$

Therefore the velocity field is mathematically integrated into two components: resolved(filtered) component denoted with a bar and sub-grid (sub-filtered) component denoted with a prime.

$$u_i = \bar{u_i} + \acute{u_i} \tag{2.44}$$

The filtered momentum equation can be written as:

$$\frac{\partial \bar{u_i}}{\partial t} + \frac{\partial \overline{(u_i u_j)}}{\partial x_j} = -\frac{1}{\rho}\frac{\partial \bar{P}}{\partial x_i} + \nu\frac{\partial^2 \bar{u_i}}{\partial^2 x_j} \tag{2.45}$$

The filtered advection term ($\overline{u_i u_j}$) is difficult to obtain since it needs the value of unfiltered velocity field, which is unknown. To solve this problem, the nonlinear term is rewritten using shear stress tensor as :

$$\overline{u_i u_j} = \overline{u_i u_j} - \bar{u_i}\bar{u_j} + \bar{u_i}\bar{u_j} = \tau_{ij} + \bar{u_i}\bar{u_j} \tag{2.46}$$

Therefore the filtered momentum equation can be written as:

$$\frac{\partial \bar{u_i}}{\partial t} + \frac{\partial (\bar{u_i}\bar{u_j})}{\partial x_j} = -\frac{1}{\rho}\frac{\partial \bar{P}}{\partial x_i} + \nu\frac{\partial^2 \bar{u_i}}{\partial^2 x_j} - \frac{\partial \tau_{ij}}{\partial x_j} \tag{2.47}$$

Momentum transfer caused by turbulent eddies can be modeled with an artificial eddy viscosity model which relates shear tensor with strain-rate tensor assuming an

equilibrium between energy production and dissipation for small eddies. Smagorinsky (1963) proposed a model, in which the effects of turbulence at small scales are related to a turbulent viscosity and dissipation of kinetic energy at sub-grid scales are assumed to be analogous to molecular diffusion.:

$$\tau_{ij} - \frac{1}{3}\tau_{kk}\delta_{ij} = -2\nu_T(\bar{S_{ij}} - \frac{1}{3}\bar{S_{kk}}\delta ij) \tag{2.48}$$

$$\nu_T = (C_s\Delta)^2|\bar{S}| \tag{2.49}$$

where C_s is Smagorinsky coefficient and Δ is filter width. Strain rate-tensor and its magnitude are defined as:

$$\bar{S_{ij}} = \frac{1}{2}(\frac{\partial\bar{u_i}}{\partial x_j} + \frac{\partial\bar{u_j}}{\partial x_i}) \tag{2.50}$$

$$|\bar{S}| = (2\bar{S_{ij}}\bar{S_{ij}})^{\frac{1}{2}} \tag{2.51}$$

For incompressible flows, the second term of left hand side of equation (5.14) will be zero. So the incompressible and compressible form of Smagorinsky model can be written as the following two equations respectively:

$$\tau_{ij} = -2(C_s\Delta)^2|\bar{S}|(\bar{S_{ij}}) \tag{2.52}$$

$$\tau_{ij} - \frac{1}{3}\tau_{kk}\delta_{ij} = -2(C_s\Delta)^2|\bar{S}|(\bar{S_{ij}} - \frac{1}{3}\bar{S_{kk}}\delta ij) \tag{2.53}$$

Yoshizawa (1986) suggested the following expression for second term of left hand side of equation(2.53):

$$\tau_{kk} = 2C_I\Delta^2|\bar{S}|^2 \tag{2.54}$$

So the turbulent shear stress in equation(2.47) can be expressed as:

$$\tau_{ij} = -2\nu_T \bar{S_{ij}} + \frac{2}{3}\nu_T \bar{S_{kk}}\delta ij + \frac{2}{3}C_I \Delta^2 |\bar{S}|^2 \delta ij \tag{2.55}$$

SPH form of turbulent shear stress term of momentum equation can discretized using Lo and Shao (2002) expression:

$$\frac{1}{\rho}\nabla.\tau_{ij}|_i = \sum_j m_j (\frac{\tau_{ij}|_i}{\rho_i^2} + \frac{\tau_{ij}|_j}{\rho_j^2}).\nabla_i W_{ij} \tag{2.56}$$

where summation is made within the neighboring particles of the particle of interest. Smagorinsky model has a good reputation for modeling the isotropic small scale eddies. However it leads to an excessive damping of large scale motions where there is a transition from boundary layers to turbulent flows. This can happen in near-wall regions. Therefore it is not possible to model transitional and turbulent flows properly with a constant universal model. This fact led to the application of dynamic methods of finding Smagorinsky coefficient that can be varied according to the flow characteristics (Meneveau et al., 1996). In our study we used the SPS approach of Dalrymple and Rogers, (2006a) with constant Smagorinsky coefficient.

2.3.3.3 Equation of state

In weakly compressible SPH, the fluid is assumed to be a weakly compressible fluid, with a very small density fluctuations. This assumption allows the pressure to be calculated from an equation of state as:

$$P = \beta[(\frac{\rho}{\rho_0})^\gamma - 1] \tag{2.57}$$

where ρ_0 is the initial density, γ is chosen to be equal to 7, and parameter β is calculated as:

$$\beta = \frac{\rho_0 c^2}{\gamma} \tag{2.58}$$

The speed of sound c in a fluid does not affect surface wave properties (except in the extreme cases of impact) and real sound speeds lead to very small computational time steps. We get around that problem by using a slower sound speed that satisfies the weakly compressible condition by setting the speed of sound to be to at least 10 times larger than the largest velocity in the model (Monaghan and Kos, 1999; Dalrymple and Rogers 2006b). Density variation in low mach number fluid fields is proportional to Mach number squared (M^2). In order to keep the density fluctuation to 0.01, Mach number needs to be equal to 0.1.

2.3.4 Boundary conditions

Several boundary treatments have been proposed to model the boundary conditions in the SPH method that will be discussed in the following sections.

2.3.4.1 Ghost Particles

In this approach, boundary condition is represented by stationary particles that are set along the boundary outside of the fluid. They have the same density and pressure as the fluid particles on the other side of the boundary but their velocity has

either the opposite sign (no slip boundary condition) or the same sign (slip boundary condition). These ghost particles do not contribute in the equations of motion. The advantage of this approach is that no extra repulsive forces need to be considered in the momentum equation and the computational treatment of this method is simple. On the other hand, it may not be applicable in some complicated problems where the direction of boundaries changes sharply. (Dalrymple and Knio, 2001)

2.3.4.2 Repulsive Boundary Particle Forces

Monaghan (1994) implemented the Lennard-Jones repulsive forces into the SPH method. In this approach, boundaries are modeled by boundary particles that exert repulsive forces on fluid particles. These repulsive forces prevent penetration of fluid particles into boundary particles and are in the form of forces between molecules. That is analogous to the fundamental molecular basis that the atoms of the fluid do not penetrate the atoms of the solid boundaries because of the repulsive atomic forces between fluid and solid atoms. The repulsive force per unit mass between boundary particle denoted as b and fluid particle denoted as i, can be expressed as the following Lennard-Jones equation:

$$\vec{f_{ib}} = D((\frac{r_0}{r_{ib}})^{P_1} - (\frac{r_0}{r_{ib}})^{P_2})\frac{\vec{r_{ib}}}{r_{ib}^2} \tag{2.59}$$

where r_{ib} is the distance between the fluid particle i and the boundary particle b and r_0 is the initial particle spacing. The total force acting on a fluid particle i in the neighborhood of boundary particles b, can be obtained as the sum of the above forces.

This summation will be included in the momentum equation:

$$\vec{f_i} = \sum_b \vec{f_{ib}} \tag{2.60}$$

The coefficient D implies physical configuration of the problem. It is usually chosen to be equal to $5gH$ where H is the depth of the water. Coefficient $P1$ and $P2$ satisfy the condition of : $P1 > P2$ and are chosen to be: $P1 = 12$ and $P2 = 6$ (Monaghan, 1994). r_0 is the initial spacing between the particles.

Monaghan et al. (1999) proposed a new form of repulsive forces where the forces from neighboring boundary particles to the fluid are in the form of a repulsive force normal to the boundary. They showed that this new form leads to a repulsive force that only depends on the perpendicular distance of the fluid particle from the boundary surface. The repulsive force is computed using two components. The first component is a function of normal distance from the boundary (denoted by y) and the second is a function of tangential distance from the boundary (denoted by x). The force per unit mass on a fluid particle from a boundary particle is obtained as follows:

$$\vec{f} = \vec{n} R(y) P(x) \tag{2.61}$$

where $\vec{n}$ is the local normal vector points from the boundary into the fluid. R(y) is defined to be equal to $R(y) = A\frac{1}{\sqrt{q}}(1-q)$ if $(q = y/h) < 1$ and otherwise $R(y) = 0$. Parameter A in the above equation is defined as:

$$A = \frac{1}{h}(0.01c^2 + \beta c^2 \vec{v_{ib}} \cdot \vec{n_b}) \tag{2.62}$$

The second term avoid penetration of fluid particles into the boundary particles and β is 1 if the fluid particles are approaching the boundary; otherwise it is zero.

Later Monaghan et al. (2003) introduced another form of repulsive boundary forces in the form of:

$$\vec{f_{ib}} = \frac{m_b}{m_i + m_b} B(x, y)\vec{n_b} \tag{2.63}$$

where y and x are perpendicular and tangential distances from the boundary particle to the fluid particle respectively. $\vec{n_b}$ is the normal at boundary particle b directed from the boundary to the fluid and m is mass of particle. Total amount of force which is applied to momentum equation is equal to $\sum_b \vec{f_{ib}}$. $B(x, y)$ is defined as follow:

$$B(x, y) = \Gamma(y)\chi(x) \tag{2.64}$$

where $\Gamma(y)$ has the form of gradient of kernel function and is presented as a function of $q = y/h$.

$$\chi(x) = \begin{cases} (1 - \frac{x}{\Delta p}) & \text{if } 0 < x < \Delta p \\ 0 & \text{Otherwise} \end{cases} \tag{2.65}$$

where Δp = boundary particle spacing.

$$\Gamma(y) = \begin{cases} \frac{2}{3}\beta & \text{if } 0 < q < \frac{2}{3} \\ \beta(2q - \frac{3}{2}q^2) & \text{if } \frac{2}{3} < q < 1 \\ \frac{1}{2}\beta(2 - q)^2 & \text{if } 1 < q < 2 \\ 0 & \text{Otherwise} \end{cases} \tag{2.66}$$

where $\beta = 0.02\frac{c^2}{y}$.

Monaghan and Kajtar (2009) introduced repulsive forces as a type of radial forces and showed that these forces are dependent only on the perpendicular distance of the fluid particle from the boundary surface and are independent of the discrete nature of boundary particle forces. Also the tangential component of these forces is negligible. Since local normals of boundary particles are not computed in this method, it is more suitable for complicated boundary conditions such as concave surfaces where local normals can cross so the direction is ambiguous. Repulsive forces in this approach are defined as:

$$\vec{f_{ib}} = \frac{K}{\beta}\frac{\vec{r_{ib}}}{r_{ib}^2}W(r_{ib}, h)\frac{2m_b}{m_i + m_b} \tag{2.67}$$

where r_{ib} is the distance between the fluid particle i and the boundary particle b. Parameter β is related to the boundary particle spacing. Usually boundary particle spacing is considered to be twice as fluid particle spacing and β is set to be equal to two. Parameter K is related to physical characteristics of the problem and is considered to be equal to gH where H is the depth of the fluid. b and i are denoted to any boundary and fluid particle respectively. Implementation of repulsive forces in the momentum equation is given as:

$$\frac{d\vec{u_i}}{dt} = -\sum_j m_j(\frac{P_i}{\rho_i^2} + \frac{P_j}{\rho_j^2} + \Pi_{ij})\nabla_i W_{ij} + \sum_{k=1}^{N_b}\sum_{b\in S_k}[\vec{f_{ib}} - m_b\Pi_{ib}\nabla_i W_{ib}] \tag{2.68}$$

In our study, we used Lennard-Jones repulsive forces to treat the boundary particles.

2.3.5 Time integration

Different time integration techniques can be used to find the fluid parameters at the next time step. In the following section a couple of these techniques are discussed.
(1) Predictor-Corrector Scheme: In this method, fluid parameters are first predicted at the half of the the time step as:

$$\begin{aligned} \vec{u_a}^{n+\frac{1}{2}} &= \vec{u}_a^n + \frac{\Delta t}{2}\vec{F}_a^n \\ \vec{r_a}^{n+\frac{1}{2}} &= \vec{r}_a^n + \frac{\Delta t}{2}\vec{v}_a^n \\ {\rho_a}^{n+\frac{1}{2}} &= \rho_a^n + \frac{\Delta t}{2}D_a^n \end{aligned} \tag{2.69}$$

where Δt = time step, $\vec{F}_a = \frac{d\vec{u}_a}{dt}$, $D_a = \frac{d\rho_a}{dt}$ and $\vec{v}_a = \frac{d\vec{r}_a}{dt}$. Then they are corrected in the correction step as:

$$\begin{aligned} \vec{u_a}^{n+\frac{1}{2}} &= \vec{u}_a^n + \frac{\Delta t}{2}\vec{F}_a^{n+\frac{1}{2}} \\ \vec{r_a}^{n+\frac{1}{2}} &= \vec{r}_a^n + \frac{\Delta t}{2}\vec{v}_a^{n+\frac{1}{2}} \\ {\rho_a}^{n+\frac{1}{2}} &= \rho_a^n + \frac{\Delta t}{2}D_a^{n+\frac{1}{2}} \end{aligned} \tag{2.70}$$

Pressure at the half of the time step is calculated using the equation of state (equation (2.57)) as $P_a^{n+\frac{1}{2}} = f(\rho_a^{n+\frac{1}{2}})$. Fluid parameters at the end of the time step are then calculated as:

$$\begin{aligned} \vec{u}_a^{n+1} &= 2\vec{u}_a^{n+\frac{1}{2}} - \vec{u}_a^n \\ \vec{r}_a^{n+1} &= 2\vec{r}_a^{n+\frac{1}{2}} - \vec{r}_a^n \\ \rho_a^{n+1} &= 2\rho_a^{n+\frac{1}{2}} - \rho_a^n \end{aligned} \tag{2.71}$$

Pressure at the end of the time step is calculated using the equation of state (equation (2.57)) as $P_a^{n+1} = f(\rho_a^{n+1})$. This method is accurate to $\mathcal{O}(\Delta^2)$ (G. R. Liu and M. B.

Liu, 2003)

(2) Verlet Scheme (Verlet, 1967): In this method, fluid parameters for each time step are calculated as:

$$\begin{aligned} \vec{u_a}^{n+1} &= \vec{u}_a^{n-1} + 2\Delta t \vec{F}_a^n \\ \vec{r_a}^{n+1} &= \vec{r}_a^n + \Delta t \vec{u}_a^n + 0.5\Delta t^2 \vec{F}_a^n \\ {\rho_a}^{n+1} &= \rho_a^{n-1} + 2\Delta t D_a^n \end{aligned} \tag{2.72}$$

Once every M time steps (in order of 50 time steps) fluid parameters are calculated as:

$$\begin{aligned} \vec{v_a}^{n+1} &= \vec{v}_a^n + \Delta t \vec{F}_a^n \\ \vec{r_a}^{n+1} &= \vec{r}_a^n + \Delta t \vec{v}_a^n + 0.5\Delta t^2 \vec{F}_a^n \\ {\rho_a}^{n+1} &= \rho_a^n + \Delta t D_a^n \end{aligned} \tag{2.73}$$

This method is accurate to $\mathcal{O}(\Delta^2)$.

(3) Modified Beeman scheme: In the predictor step, the fluid parameters are computed as (Panizzo et al., 2006):

$$\begin{aligned} \vec{v_a}^{n+\frac{1}{2}} &= \vec{v}_a^n + \frac{3}{2}\Delta t \vec{F}_a^n - \frac{1}{2}\Delta t \vec{F}_a^{(n-1)} \\ \vec{r_a}^{n+\frac{1}{2}} &= \vec{r}_a^n + \Delta t \vec{v}_a^n + \frac{2}{3}\Delta t^2 \vec{F}_a^n - \frac{1}{6}\Delta t^2 \vec{F}_a^{(n-1)} \\ {\rho_a}^{n+\frac{1}{2}} &= \rho_a^n + \frac{3}{2}\Delta t D_a^n - \frac{1}{2}\Delta t D_a^{(n-1)} \end{aligned} \tag{2.74}$$

In the corrector step:

$$\begin{aligned} \vec{v}_a^{n+1} &= \vec{v}_a^n + \frac{5}{12}\Delta t \vec{F}_a^{n+\frac{1}{2}} + \frac{8}{12}\Delta t \vec{F}_a^n - \frac{1}{12}\Delta t \vec{F}_a^{n-1} \\ \vec{r}_a^{n+1} &= \vec{r}_a^n + \vec{v}_a^n \Delta t + \frac{1}{6}\Delta t^2 \vec{F}_a^{n+\frac{1}{2}} + \frac{1}{3}\Delta t^2 \vec{F}_a^n \\ \rho_a^{n+1} &= \rho_a^n + \frac{5}{12}\Delta t D_a^{n+\frac{1}{2}} + \frac{8}{12}\Delta t D_a^n - \frac{1}{12}\Delta t D_a^{n-1} \end{aligned} \tag{2.75}$$

This method is accurate to $\mathcal{O}(\Delta^4)$.

In our study, the predictor-corrector scheme is used for the time integration. The explicit time integration schemes are limited by the Courant-Friedrichs-Lewy (CFL) condition for the stability. This condition is considered to assure that the maximum speed of numerical propagation exceeds the maximum speed of physical propagation in order to model the physical domain correctly (Anderson, 1995; Hirsch, 1988). Therefore, when the numerical resolution become finer, the upper limit for the time step decreases as well. In SPH formulation, Monaghan and Kos (1999) combined the CFL condition with viscous dissipation condition and proposed the following condition:

$$\Delta t_{cv} = min_a \frac{h}{C_s + max_b |\frac{h\vec{v}_{ab}\vec{r}_{ab}}{\vec{r}_{ab}^2}|} \tag{2.76}$$

$$\Delta t_f = min_a (\frac{h_a}{|f_a|})^{\frac{1}{2}} \tag{2.77}$$

$$\Delta t = 0.3.min(\Delta t_f, \Delta t_{cv}) \tag{2.78}$$

where $|f_a|$ is the force per unit mass of particle a and h_a is the smoothing length of particle a.

2.3.6 Density reinitialization-Shepard filtering

On of the difficulties in the SPH method is the boundary deficiency problem (Monaghan, 1992; Randles and Libersky, 1996). The particles that are close to the boundaries or the free surface have truncated summations due to the insufficient particles in their support domain since no particles exist beyond the boundary or the free surface. The boundary deficiency problem results in lower density close to the boundaries and the free surface and consequently spurious pressure gradients (Morris et al. 1997). Different approaches have been proposed to treat this problem. A zeroth-order Shepard filter (Shepard, 1968) can be implemented to reinitialized the density once every M time steps (we use M = 30) as:

$$\rho_a = \frac{\sum_b \rho_b W_{ab} V_b}{\sum_b W_{ab} V_b} \tag{2.79}$$

Shepard filtering ensures that the free surfaces are smooth and physically acceptable (Dalrymple and Rogers, 2006). Amicarelli et al. (2010) reported that by applying Shepard filtering the relative error between interpolated function and the actual value of the function tends to zero with h^2 for fluid particles and with h for wall particles where h is the smoothing length of the kernel function.

2.3.7 XSPH correction

For free surface flows, Monaghan (1994) suggested the XSPH correction to update the particle position as:

$$\begin{aligned} (\frac{d\vec{r}}{dt})_a &= \vec{u}_a + \epsilon \Delta u_i \\ \Delta u_i &= \sum_b \frac{m_b}{\rho_b}(u_b - u_i) W_{ab} \end{aligned} \tag{2.80}$$

where ϵ is a constant coefficient ranging from 0 to 1. The goal of this correction is to use a corrected velocity, which relates the particle's velocity with the velocity of its neighboring particles and results into smoother particle movement. XSPH correction is reported to maintain the movement of particles and to prevent the particle penetration problem.

2.3.8 Linked-list neighboring particles search algorithm

SPH formulations are based on the interpolation over the neighboring particles. Thus, an efficient search algorithm for neighbors can decrease the computational expenses dramatically. Monaghan and Gingold (1983) indicated that the linked-list searching algorithm performs well for the SPH computations. In the linked-list algorithm, a temporary grid is constructed on the problem domain. The grid spacing is equal to the compact support of the kernel function. For instance, for a kernel function with the compact support of $2h$, the mesh spacing would be equal to $2h$

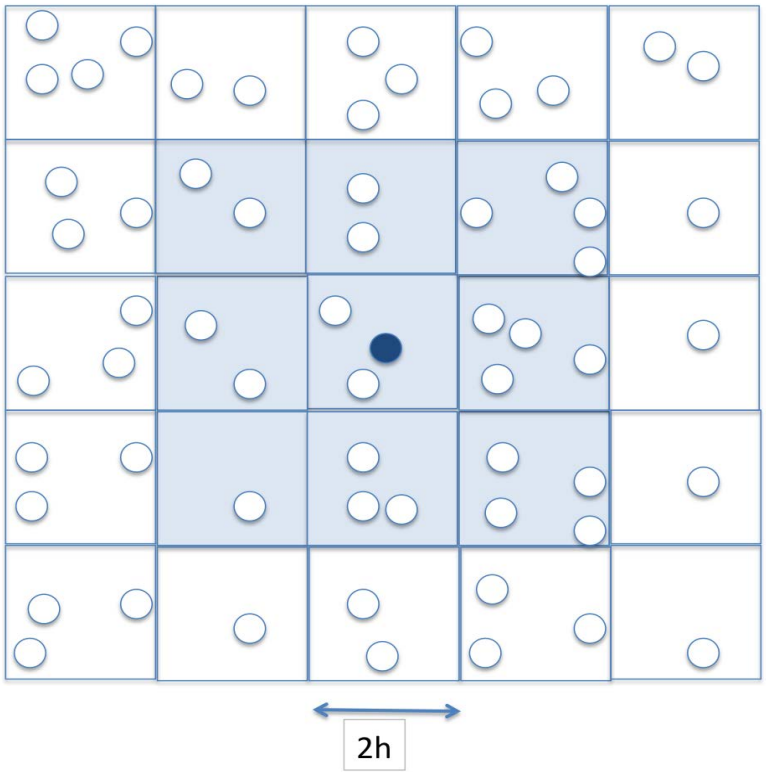

Figure 2.2: Linked-list algorithm for searching the neighboring particles in a two-dimensional space

where h is the smoothing length of the kernel function. Each particle is assigned to a cell according to its coordinate position. For a particle of interest a, the neighboring particles can only be located in the same grid cell or the immediately adjoining cells. Therefore, the search is confined only over 3, 9, or 27 cells for one-, two-, and three-dimensional problems respectively (figure 2.2). Linked-list search algorithm is of order of $\mathcal{O}(N)$, where N is the number of particles. However, not using a search algorithm results into a $O(N)^2$ order.

Chapter 3

GPUSPH

3.1 Introduction

Three-dimensional SPH is computationally intensive, especially for large and complicated cases, requiring the use of parallel computing, which is usually done on a cluster of multiple Central Processing Units (CPUs). Recently advances in computer technology permit the use of Graphics Processing Units (GPUs) for parallel computing with high computational power and low expenses. GPU cards developed primarily for video gaming, so they have a massively parallel structure. On the other hand, the data-parallel nature of SPH method makes it perform well on the multithreaded GPU. GPU programming can be traced back to General-Purpose computation on GPU (GPGPU). The older methods required programmers to understand graphic programming languages in order to do numerical computations. In 2007, a new GPU

parallel architecture is introduced by Nvidia as Compute Unified Device Architecture (CUDA), which uses high-level languages such as C, C++, and Fortran to program the graphic cards so computation on the GPU has become easier.

In this chapter a brief description of general-purpose GPU programming and CUDA architecture will be reviewed. The GPUSPH model, which implements SPH calculations on GPUs, was first introduced by Alexis Hérault (Hérault et al. 2010), and its various features will be discussed.

In our study, two additional features have been added to the existing GPUSPH package. The first feature is fluid parameter computation at Eulerian nodes, which enables us to perform a more comprehensive comparison between numerical and Eulerian experimental results. The second feature is free-surface particles detection, which enables us to accurately calculate the depth-averaged velocity profiles. These two features will be discussed in detail in chapter 4.

3.2 General-Purpose Graphics Processing Units (GPGPU)

Graphics Processing Units (GPUs) are high-performance multi-core processors that have a parallel nature and can be used to perform parallel computing for a variety of applications. On 2006, Compute Unified Device Architecture (CUDA) was introduced that was designed for general-purpose computations on GPUs. CUDA platform

is accessible through extensions to the standard programming languages such as C, C++, and FORTRAN. GPU multiprocessors use blocks of threads. These blocks consist of one-dimensional, two-dimensional, or three-dimensional grids of thread as shown in figure 3.1. A problem can be divided into sub-problems that can be solved

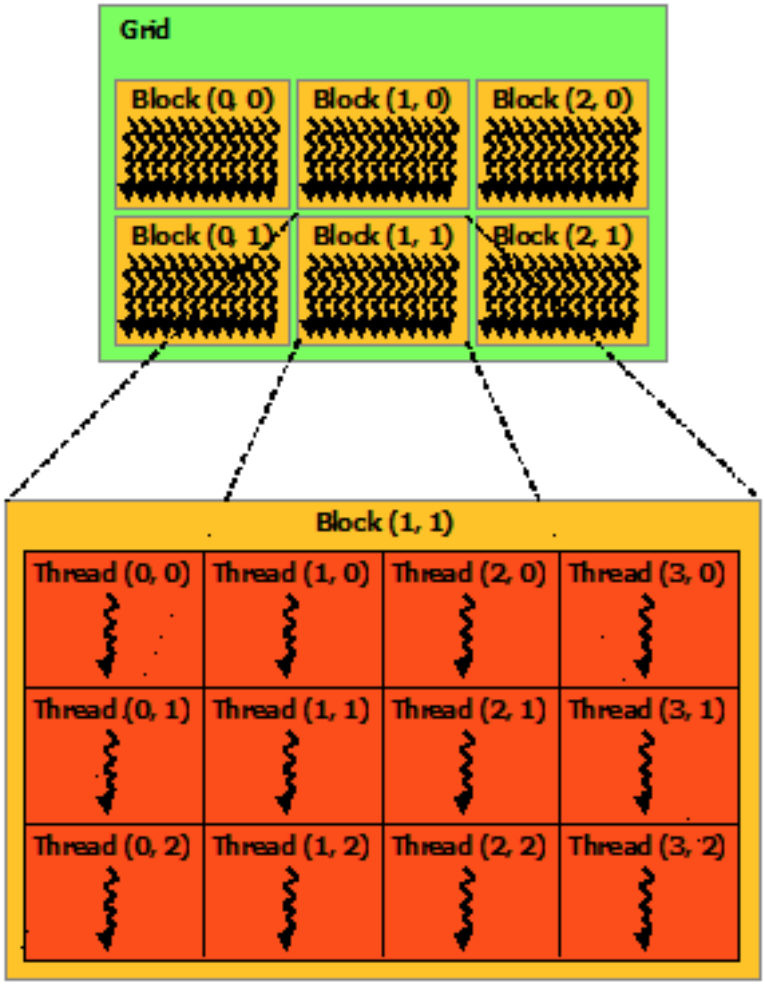

Figure 3.1: Architecture of a grid in a GPU, a grid consists of several blocks and each block consists of several threads. (www.nvidia.com)

independently in parallel by blocks of threads (task parallelism). Each sub-problem

can be solved cooperatively in parallel by threads of a block (data parallelism). Figure 3.2 illustrates a multithreaded CUDA program and the different ways it can be executed on a GPU depending on the number of the streaming multiprocessors (SMs) of that GPU.

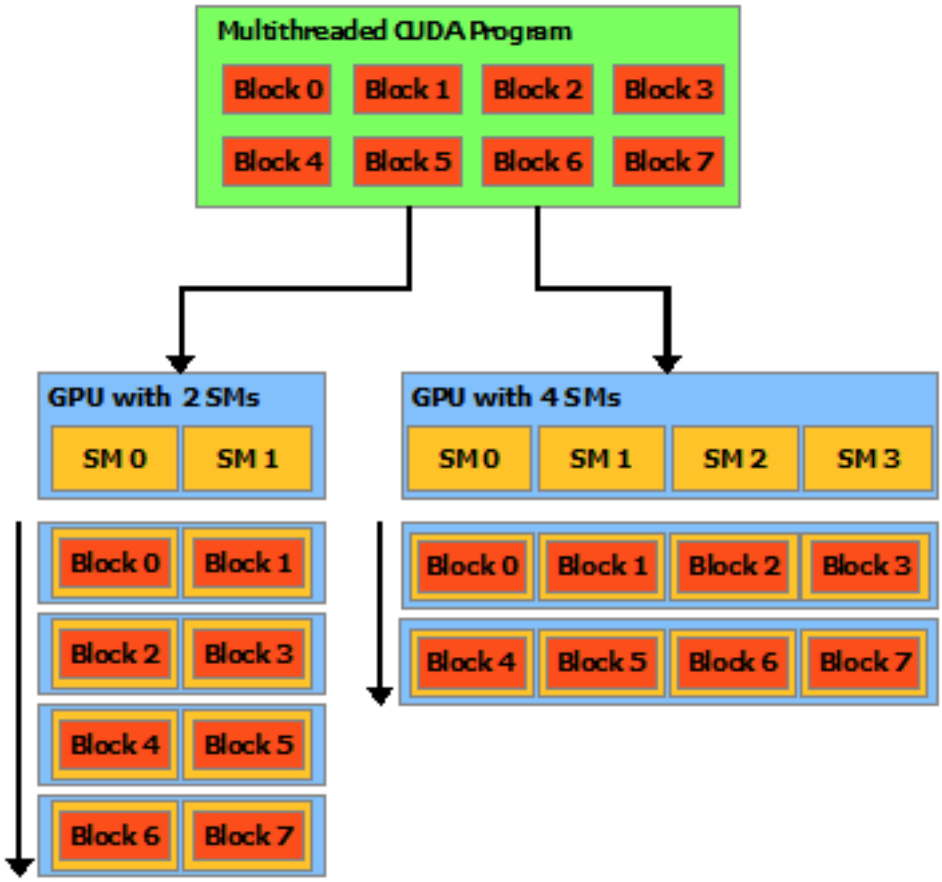

Figure 3.2: Automatic scalability of a CUDA program on GPUs with different numbers of Streaming Multiprocessors (SMs) (www.nvidia.com)

The CUDA program automatically scales according to the number of SMs. There is a limit to the maximum number of threads in a block, since all threads of a block

are located on the same processor core and share the shared memory of that core. For the present GPUs, this limit is equal to 1024 threads per block. However, the same task can be executed by multiple equally-shaped blocks and in this case the total number of threads will be equal to the number of threads per block times the number of blocks.

Different memory spaces are accessible by the threads. Each thread has a local memory space. Each block has a shared memory that is accessible by all of the threads of that block. GPU also has a global memory that is accessible by all the threads. In addition, threads may access two read-only memory as constant and texture memory spaces. Figure 3.3 illustrates the different memory spaces. Each of these memory spaces may be used depending on the particular problem and considering the optimized memory usage.

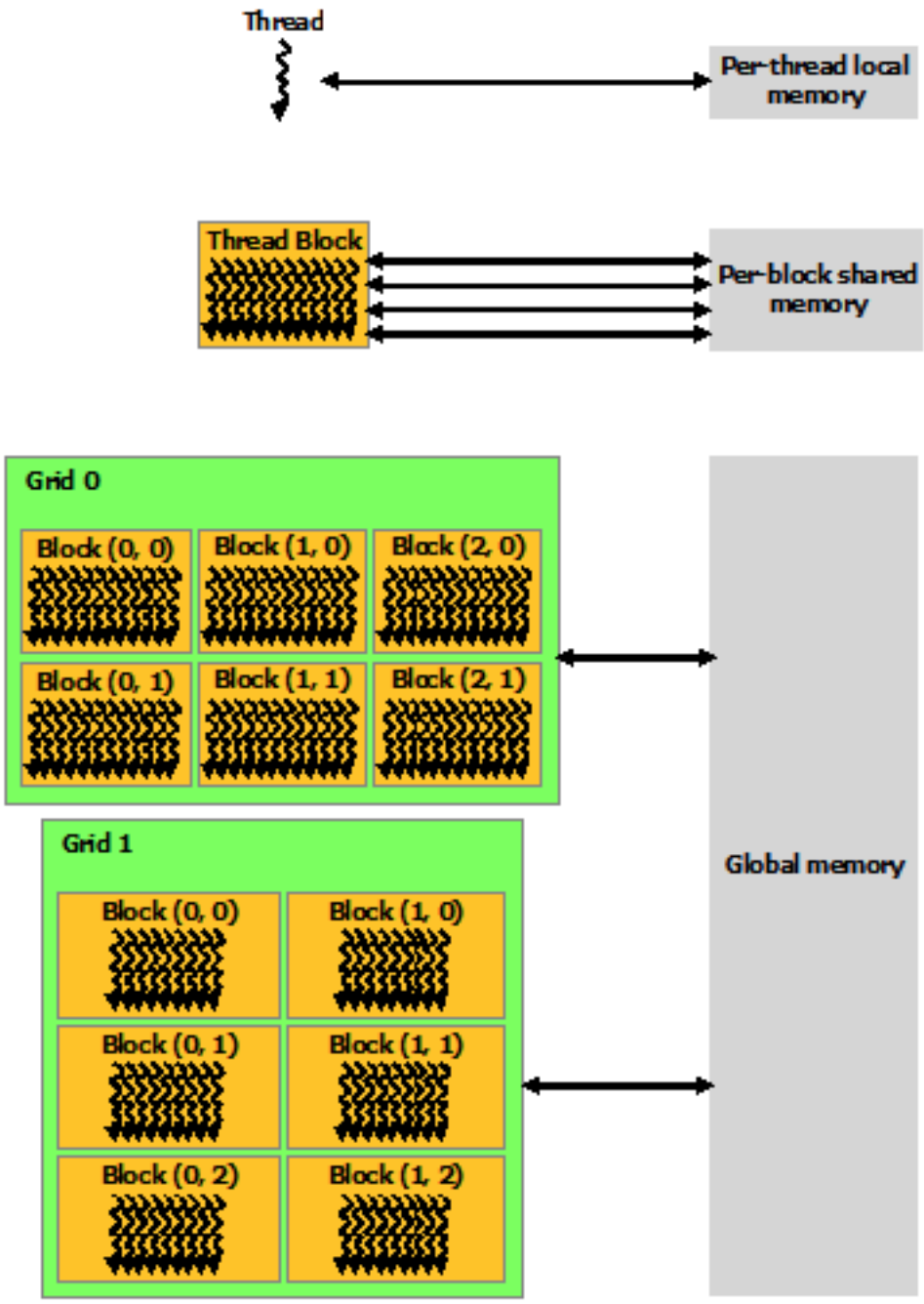

Figure 3.3: Per-thread local memory, per-block shared memory, and global memory spaces in a GPU (www.nvidia.com)

3.3 Getting Started with CUDA

In this section, the prerequisites to developing a code in CUDA/C,C++ will be explained. The primarily steps are as follows:

(1) Having a CUDA-capable GPU

(2) Download and install the NVIDIA device driver

(3) Download and install CUDA toolkit

(4) Having a C compiler

GPUs based on CUDA architecture are released by NVIDIA. A list of CUDA-capable GPUs can be found at NVIDIA website (https://developer.nvidia.com/cuda-gpus). A variety of CUDA-capable GPUs with different compute capabilities, memory size, and CUDA cores are available and can be chosen according to the particular application. NVIDIA device driver is a software that helps the programs to communicate with the CUDA-capable hardware. The latest NVIDIA driver can be found at NVIDIA website. CUDA toolkit is needed to compile a new code. CUDA codes are computed on two different processors (GPU and CPU). Therefore, one compiler is needed to compile the code on GPU and another compiler is required to compile the code on CPU. CUDA toolkit provides the essential compiler for the GPU.

3.4 CUDA Structure

In a CUDA program, input data is introduced to the system's memory and CPU, which is called the *host*. Then, that data is transferred to the GPU and its memory, which is called the *device*. Parallel computation is performed on the device and output data is transferred back to the host. Data copies between device and host can be avoided using mapped memory that is available for the devices of compute capability greater than 1.0 where a block of host memory can be mapped into the address space of the device memory. In this case, the data in the host block has two addresses, one in the host memory and one in the device memory and therefore it can be accessible directly from the device. However, memory synchronization needs to be considered to avoid any read-after-write, write-after-read, or write-after-write problems. Functions on the device are called "kernels" that can be executed in parallel by CUDA threads as opposed to only once as regular functions on the host. Kernels are compiled into binary codes using "nvcc" compiler and then they are ready to be executed on the device. Note that the CUDA kernels and the SPH kernels are not the same.

3.5 GPUSPH

GPUSPH is an open source package that implements the computations of Smoothed Particle Hydrodynamics method on Nvidia graphic cards. GPUSPH was started

by Alexis Hérault (Hérault et al. 2010) in a study of lava cooling. It utilizes CUDA language and was inspired by the Nvidia SDK program Particles (*http* : *//www.ce.jhu.edu/dalrymple/GPUSPH/Home.html*). One of the advantages of GPUSPH is that the model can display real-time results. This ability helps the modelers to see partial results images while the model is running and study the particles' displacement and fluid parameters such as velocity and pressure before the run is completed. Real-time images are provided in GPUSPH using OpenGL program.

GPUSPH is written in an object-oriented platform and consists of several interacting objects. In an Object-Oriented Program (OOP), a set of objects interacts with each other, as opposed to the non-OOP models, in which a program consists of a set of subroutines each performing a particular task. Object-oriented programs are easier to maintain, modify, and expand. New features or physical problems can be added to the existing program by introducing new objects.

GPUSPH consists of several C++ classes that interact with each other. In the following sections, the main GPUSPH classes will be described.

3.5.1 "ParticleSystem" Class

One of the main GPUSPH classes is called "ParticleSystem", which is introduced in "ParticleSystem.cc" and "ParticleSystem.h" files. The following processes are performed in "ParticleSystem" class:

(1) Memory allocation of GPU and CPU variables (ParticleSystem : : allocate)

(2) Specifying the physical parameters of the problem such as gravity, viscous coefficient, etc by interacting with "physparams" structure. (ParticleSystem :: setPhysParams)

(3) Transferring the initial data from CPU to GPU (ParticleSystem : : setArray)

(4) Performing neighboring particles search (ParticleSystem : : BuildNeibList)

(5) Computing the forces, velocities, and position of particles in each time step using a predictor-corrector method (ParticleSystem : : PredcorrTimeStep)

(6) Transferring the computed data from GPU to CPU (ParticleSystem : : getArray)

(7) Writing the essential data to the output files (ParticleSystem : : writeToFile)

3.5.2 "Problem" Class

Initial configurations of the physical problems in GPUSPH are initialized by a C++ class called "Problem" introduced in "Problem.cc" and "Problem.h" files. Several classes in GPUSPH are inherited from "Problem" class such as: "DamBreak3D", "DamBreakGate", "OpenChannel", "SolitaryWave", "Seiche", "TestTopo", and "WaveTank". These classes illustrates a particular physical problem by specifying the following information:

(1) Dimensions and initial configurations

(2) Boundary conditions

(3) Simulation parameters

(4) Physical parameters

(5) The format of the output files

A new class according to the user's specific physical problem can be added to the code by inheriting from the "Problem" class similar to the other inherited classes. Geometry of the physical problem as well as the physical and simulation parameters can be introduced to this new class. The initial geometry of the physical problem can be defined using the "Object" class that will be discussed in the next section.

3.5.3 "Object" Class

An initial geometry of a physical problem can be defined in GPUSPH using a C++ class called "Object". Several classes are inherited from the "Object" class to define different geometrical shapes such as : "Cone", "Cube", "Cylinder", "Disk", "Rect" (rectangle), "Point", "Vector", "Segment", "Circle", "Sphere", "TopoCube", and "Torus" classes. A physical problem can be defined as one or a combination of theses different classes.

3.5.4 Neighboring Particles List

SPH interpolation requires a list of neighboring particles for each particle. Searching for the neighboring particles is performed in "buildneibs_kernel.cu", "buildneibs.cu", and "buildneibs.cuh" files. The "buildneibs_kernel.cu" file includes the device kernels that are being executed on the GPU. A particle sort method, which has been applied

in the CUDA SDK examples, is used to maintain the memory latency and to increase the computational efficiency. The "buildneibs.cu", and "buildneibs.cuh" files include the related functions that are being executed on the host (CPU).

3.5.5 Forces Calculations

Forces for each particle are being computed in "forces_kernel.cu", "forces_kernel.def", "forces.cu", and "forces.cuh" files. The "forces_kernel.cu" and "forces_kernel.def" files include the device kernels that are being executed on the GPU. The "forces.cu" and "forces.cuh" files include the functions that are being executed on the host (CPU).

3.5.6 Velocity and Position of Particles at Each Time Step

Velocity and position of particles at each time step are computed in "euler_kernel.cu", "euler_kernel.def", "euler.cu", and "euler.cuh" files where the time integration occurs. The "euler_kernel.cu" and "euler_kernel.def" files include the device kernels that are being executed on the GPU. The "euler.cu" and "euler.cuh" files include the functions that are being executed on the host (CPU).

3.5.7 Output data

Output data can be stored in the output files using a C++ class called "Writer" in the GPUSPH. Several classes such as "TextWriter", "VTKLegacyWriter", "VTK-Writer", and "CustomTextWriter" are inherited from the "Writer" class. These classes are introduced to save output files in different formats.

3.5.8 OpenGL Graphics

The main program of GPUSPH is located in the "GPUSph.cc" file and is presented as an OpenGL program. OpenGL helps GPUSPH to benefit from the real-time results display. The OpenGL Utility Toolkit (GLUT) is used to set-up an image window and show the real-time results as GPUSPH is running.

3.5.9 Simulation parameters

Simulation parameters such as kernel function formulation and smoothing length are introduced in the "SimParams" data structure in the "simparams.h" file. Table 3.1 shows the simulation parameters and their default values. The user can change the values of the simulation parameters for his own problem. For instance the default method of boundary condition treatment is the Lennard-Jones repulsive forces method (boundarytype(LJ_BOUNDARY)) but the user can specify a different boundary condition treatment such as the Monaghan-Kajtar (2009) method in the

problem file.

Table 3.1: Simulation Parameters in "SimParams" data structure

Simulation Parameters		
Structure Member	Description	Default Value
slength	Smoothing length	—
kerneltype	Kernel function formulation	—
Kernelradius	This parameter is used to build the neighbor list cells. Size of neighbor list cells is equal to "slength" times "Kernelradius" in x,y, and z directions.	2.0
dt	Initial Time Step	0.00013
tend	Simulation End Time	—
xsph	If true, the xsph correction will be applied	False
dtadapt	If true, the time step will be varied during the simulation	True

Simulation Parameters (Continued)		
dtadaptfactor	This factor is used in the computation of the time step during the simulation	0.3
buildneibsfreq	This parameter indicates the frequency of the neighboring list rebuilding	10 (Every 10 iterations)
shepardfreq	This parameter indicates the frequency of the Shepard filtering application	0 (Every 0 iterations)
mlsfreq	This parameter indicates the frequency of the MLS correction application	15 (Every 15 iterations)
visctype	This parameter indicates the method to compute the viscous term of the momentum equation	Artificial viscosity method
displayfreq	This parameter is used to find the frequency of writing and displaying of the data (Seconds)	—

Simulation Parameters (Continued)		
savedatafreq	This parameter indicates the data saving frequency (multiply of displayfreq).	—
saveimagefreq	This parameter indicates the image saving frequency (multiply of displayfreq).	—
mbcallback	If true, moving boundary conditions can be introduced to the problem.	False
callback	If true, variable gravity can be introduced to the problem.	False
periodic bound	If true, periodic boundary condition can be introduced to the problem.	False
usedem	If true, the geometry of the bottom boundary condition can be introduced through an external data file.	False

Simulation Parameters (Continued)		
sph_formulation	The formulation of density and pressure computation can be chosen via this parameter.	SPH_F1
boundary type	The method of boundary condition treatment is chosen via this parameter.	LJ_BOUNDARY
vorticity	If true, vorticity of particles will be computed	False
testpoints	If true, velocity and pressure at fixed-position test points will be computed	False
savenormals	If true, Normals of the particles will be saved	False
surfaceparticle	If true, surface particles will be detected	False
numbodies	Number of floating bodies	0
maxneibsnum	Maximum number of neighboring particles in the neighbor list	128

3.5.10 Physical parameters

Physical parameters such as initial density and gravity are introduced in the "PhysParams" data structure in the "physparams.h" file. Like the simulation parameters, the physical parameters can be chosen or changed in the problem file. Table 3.2 shows the physical parameters and their default values.

Table 3.2: Physical Parameters in "PhysParams" data structure

Physical Parameters		
Structure Member	Description	Default Value
rho0	Initial density of the particles	—
part surf	This parameter is used in the plane boundary condition treatment	0.0
gravity	Gravity acceleration	—
bcoeff	This parameter is used in the equation of state (β)	—
gammacoeff	This parameter is used in the equation of state (γ)	—
sscoeff	This parameter is used to find sound speed	—
sspowercoeff	This parameter is used to find sound speed	—
r0	This parameter is used in the Lennard-Jones repulsive forces boundary condition	—

Simulation Parameters (Continued)		
dcoeff	This parameter is used in the Lennard-Jones repulsive forces boundary condition (D)	—
p1coeff	This parameter is used in the Lennard-Jones repulsive forces boundary condition ($P1$)	12
p2coeff	This parameter is used in the Lennard-Jones repulsive forces boundary condition ($P2$)	6
MK_K	This parameter is used in the Monaghan-Kajtar repulsive forces boundary condition (K)	—
MK_d	This parameter is used in the Monaghan-Kajtar repulsive forces boundary condition (Distance between the boundary particles)	—

Simulation Parameters (Continued)		
MK_beta	This parameter is used in the Monaghan-Kajtar repulsive forces boundary condition (β)	—
kinematicvisc	Kinematic viscosity	—
artvisccoeff	Artificial viscosity coefficient	—
epsartvisc	This parameter is used in the Monaghan-Kajtar repulsive forces boundary condition	—
epsxsph	XSPH correction coefficient	0.5
dispvect	This parameter is used in the periodic boundary condition and indicates the periodic boundary domain	—
minlimit	This parameter is used in the periodic boundary condition and indicates the first limit of the periodic boundary condition	—
maxlimit	This parameter is used in the periodic boundary condition and indicates the second limit of the periodic boundary condition	—

Simulation Parameters (Continued)		
ewres	This parameter is used in "DEM" bottom boundary treatment (east-west resolution)	—
nsres	This parameter is used in "DEM" bottom boundary treatment (north-south resolution)	—
demdx	This parameter is used in the boundary force computations of "DEM" bottom boundary treatment	—
demdy	This parameter is used in the boundary force computations of "DEM" bottom boundary treatment	—
demdxdy	This parameter is used in the boundary force computations of "DEM" bottom boundary treatment	—
demzmin	This parameter is used in the boundary force computations of "DEM" bottom boundary treatment	—

Simulation Parameters (Continued)		
smagfactor	This parameter is used in the SPS term computation ($(C_s\Delta)^2$)	–
kspsfactor	This parameter is used in the SPS term computation ($\frac{2}{3}C_I\Delta^2$)	–
numFluids	Number of fluids in the multi-phase problems	1.0
cosconeanglefluid	Cos of the cone angle for the free surface detection (If the neighboring particles are fluid)	0.86
cosconeanglenonfluid	Cos of the cone angle the for free surface detection (If the neighboring particles are non-fluid)	0.5
objectobjectdf	Damping factor used for the object-object interaction	1.0
objectboundarydf	Damping factor for the object-boundary interaction	1.0

Chapter 4

Three dimensional SPH modeling of a bar/rip channel system

4.1 Introduction

Waves propagating towards shore carry mass, energy and momentum into the near-shore zone. If the nearshore bathymetry is spatially variable, parts of a wave crest in shallower water break sooner and begin dissipating energy and losing momentum, while other parts of the wave crest in deeper water are still propagating towards the shore, eventually breaking further inshore. As a result, alongshore variations of wave amplitude, radiation stresses and mean water level (set-up) occur, which result in a nearshore circulation system, including the rip current.

Rip currents are fast, shore-normal flows that travel in the seaward direction

and can create a natural hazard for beach-goers and swimmers. Rip currents in the nearshore zone are created in a variety of ways that can be classified in three major classes: bathymetric variations, wave-wave interactions, and instabilities of alongshore currents and/or shear instabilities. (See the recent review by Dalrymple et al., 2011). Here we focus on rip currents that occur due to the variations in the bathymetry.

Shepard et al. (1941) discussed that the wave height is an important factor in the development of the rip currents. Shoreline configuration and tide were among the other factors that were considered to be influential to the generation of rip currents. Later Mckenzie (1958) pointed out that the slope and regularity of the near-shore sea floor are factors that affect the way in which the waves are broken and refracted. Bowen and Inman (1969a), (1969b) first developed a theoretical derivation of rip currents using the equations of momentum and continuity including radiation stresses in shallow water. They developed a simplified near-shore circulation model for rip currents, including bathymetric variation, and then they studied rip currents induced by the interaction of edge waves and incident waves (a wave-wave interaction mechanism). Later Dalrymple (1975) showed that the intersecting wave trains of the same frequency create rip currents due to the periodic alongshore variation in the mean water level. Rip currents resulting from bathymetric variations have been studied in numerous field measurements, laboratory experiments, and numerical models. In the field, Wright and Short (1984) observed a quasi-systematic morphodynamics in

the surf zone, studying 4 years of data from the coast of Australia. They clearly showed that the presence of rip currents was tied to the alongshore variability of the bathymetry occasioned by the migration shoreward of an offshore sand bar, created during a storm. Other field observations include Sonu (1972), Lippmann and Holman (1990), Smith and Largier (1995), Aagaard et al. (1997), Brander (1999), Short and Brander (1999), MacMahan et al. (2005), MacMahan et al. (2010) and Sénéchal et al. (2004). Interestingly MacMahan et al. (2010) showed that for some bathymetries the rip currents are confined to the surf zone, rather than extending offshore of the breaker-line.

In the laboratory, Haller et al. (1997) studied rip current systems due to alongshore variations of underlying bed topography. They carried out a series of experiments in a 17 m by 18 m wave basin with three fixed sand bars and two rip channels between them. Interaction of the surface waves with rip currents and the near-shore circulation generated by the wave breaking on a barred beach were investigated. Their measurements included depth-integrated velocities, wave height and mean water level. Haller et al. (1997), and Haller and Dalrymple (2001) showed that these rip currents were unstable, oscillating side to side due to a shear instability. Haas and Svendsen (2002) conducted a laboratory measurement of the vertical structure of rip currents using the bed topography of Haller et al. (1997). Drønen et al. (2002) performed a laboratory study of flow over a single bar and a rip channel, which could be considered a subset of the Haller type experiment. The experiments were per-

formed in a 4 m wide by 30 m long wave tank. The set-up represented one-half of a rip current system, represented by two bars with a rip channel in between (using symmetry about the sidewalls). The two shore-normal sidewalls of the wave tank correspond to the centerline of rip channel and centerline of one of the bars. They measured three-dimensional (3D) velocity profiles and mean water levels. Particle trajectories tests were also performed to track the flow in a rip current system. We chose this experiment to model with SPH as the domain is smaller than in Haller et al. (1997). In terms of numerical studies, most of the numerical models are two-dimensional, involving integration over depth and time-averaging over a wave period (Noda, 1974, Yu and Slinn, 2003). Chen et al. (1999) modeled the Haller et al. (1997) experiment using the FUNWAVE model (Wei and Kirby, 1995), which solves the Boussinesq equations, which as shown by Madsen et al. (1997) can represent not only the phase-dependent incident waves, but also the wave-induced mean flows, to model the unstable rip current system reasonably well. Haas et al. (2003) numerically modeled their previous experimental studies (Haas and Svendsen, 2002) by the use of a quasi-three-dimensional numerical model (SHORECIRC). In their numerical model, the depth-integrated wave-averaged equations are solved and the effect of the vertical variation of the currents is separately included in the depth-integrated wave-averaged 2D equations.

The numerical methods that have been used to model near-shore circulations are mostly 2D or quasi 3D. Three-dimensional modeling of rip current and related near-

shore circulations is important in understanding the physical processes involved in a rip current system. Therefore in the present study, three-dimensional SPH method is used to capture the 3D structure of flow in a bar/rip channel system. In addition, in order to compare the two-dimensional depth-integrated mean flows with experimental results, Eulerian fixed positions are set in the numerical model and fluid variables at those fixed nodes are calculated using SPH interpolation. The final model is capable of finding fluid variables on Eulerian fixed nodes as well as Lagrangian moving particles and comparison of both two-dimensional mean patterns and three-dimensional variations of flow are possible. Numerical results are compared to the laboratory measurements of Drønen et al. (2002), including mean horizontal velocities, mean water level, alongshore and cross-shore currents. The three-dimensional structure of flows has been studied in the different positions of the rip current system. Trajectory tracking of SPH fluid particles revealed the flow paths in different position of the rip current system. Variation of different components of radiation stress and the resulting force that acts as a feeder for the rip current have been examined also. In addition, wave-current interaction and the effect of current on the wave number and wave amplitude variation have been included.

4.2 Bar/rip channel configuration

The bathymetry used in the numerical model was inspired by the wave tank experiment of Drønen et al. (2002), which corresponds to one half of a periodic bar/rip channel system. This experiment was performed in a 4 m wide and 30 m long wave tank. The bar is 4.8 m long, 3 m wide and 0.13 m high and has a slope of in cross-shore direction. The width of the rip channel is 1 m and has the same slope of the beach. Figure 4.1 illustrates the bed topography of the Drønen et al. (2002) experiment.

The three-dimensional structure of wave-induced rip current and surf zone circulations as well as mean currents were measured in this set of experiments. In our numerical model, two different set-ups are considered. In the first one, still water depth at the bar crest is set to 0.15 m, wave height is set to 0.19 m, and wave period is set to 1.5 s (similar to the test 1a of Drønen et al. 2002). In the second one, still water depth at the bar crest is equal to 0.1 m, wave height is set to 0.15 m and wave period is set to 1.5 s (similar to the test 3* of Drønen et al. 2002). The reason behind choosing these two sets of experimental data is that in the first experimental test (test 1a, Drønen et al. 2002) mean horizontal circulations and mean surface elevations were measured, while in the second experimental test (test 3*, Drønen et al. 2002) cross shore velocity components at the position of the rip channel were measured. Therefore, comparisons of different data between numerical and experimental results will be possible. This idealized bathymetry is modeled using GPUSPH model

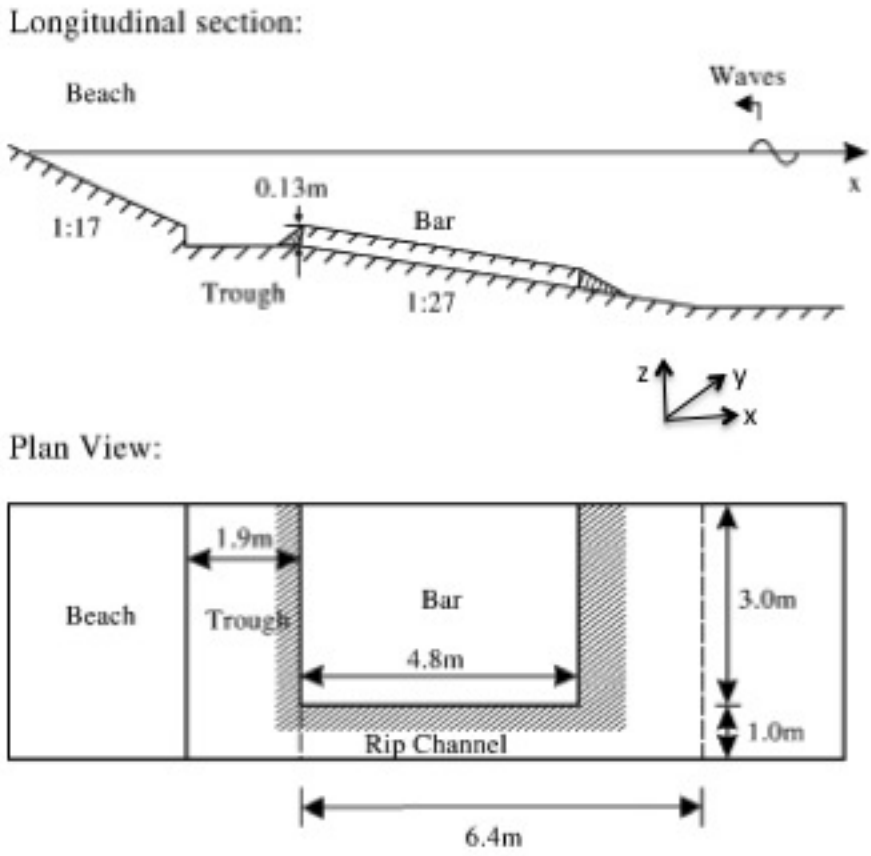

Figure 4.1: Rip current system bathymetry. Top: Side view; Bottom: Plan view (Drønen et al., 2002)

using about three million particles with an initial particle spacing of 0.02 m and a smoothing length of 1.3 times the initial particle spacing. A convergence study has been conducted in order to choose the suitable initial particle spacing that will be discussed in the succeeding sections. A piston produces regular waves normal to the coastline and is located around 6 m from the beginning of the sloping part of the bed topography (around 12.4 m offshore of the crest of the bar). Figure 4.2 shows the bathymetry, where the wave maker is at the right hand side and beach is located on

the left hand side of the figure.

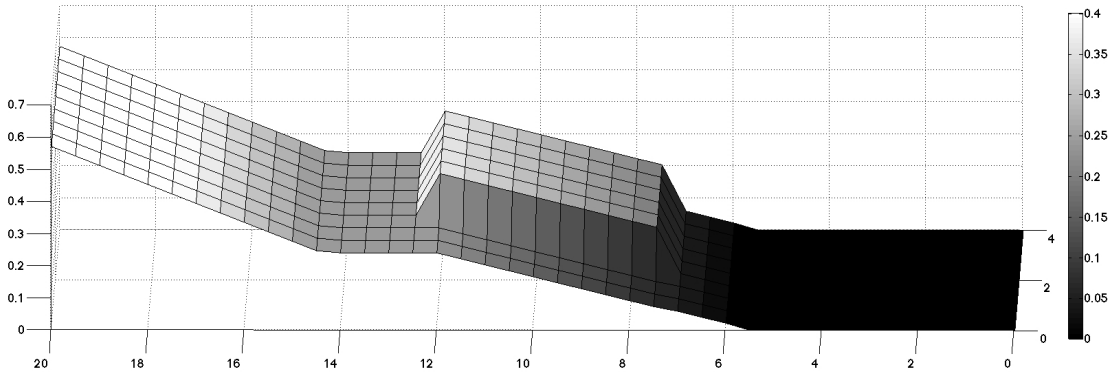

Figure 4.2: Bottom bathymetry applied to the numerical model. Wavemaker is at the right end and the beach is at the left end.

4.3 Fluid parameters on Eulerian nodes

Comparisons of SPH models to Eulerian laboratory data can be problematic since SPH results are known on irregularly-spaced moving particles and it is difficult to compare the results with the experimental results that are measured at fixed positions. In order to solve this problem, a straightforward method is used to interpolate the SPH data to a regular grid. For this purpose, a Cartesian grid, which covers the entire computational domain, is introduced. For each node of this fixed grid, the neighboring moving particles are found and the fluid parameters of the fixed node are calculated using the SPH interpolation:

$$A_n = \sum_p m_p \frac{A_p}{\rho_p} W(|\vec{r_n} - \vec{r_p}|, h) \tag{4.1}$$

where notation n corresponds to a fixed node, notation p corresponds to the moving particles around it, and A can be any fluid parameter such as velocity, pressure or density. The kernel function W restricts the sum to neighboring particles. Figure 4.3 shows the interaction of fixed nodes and moving particles.

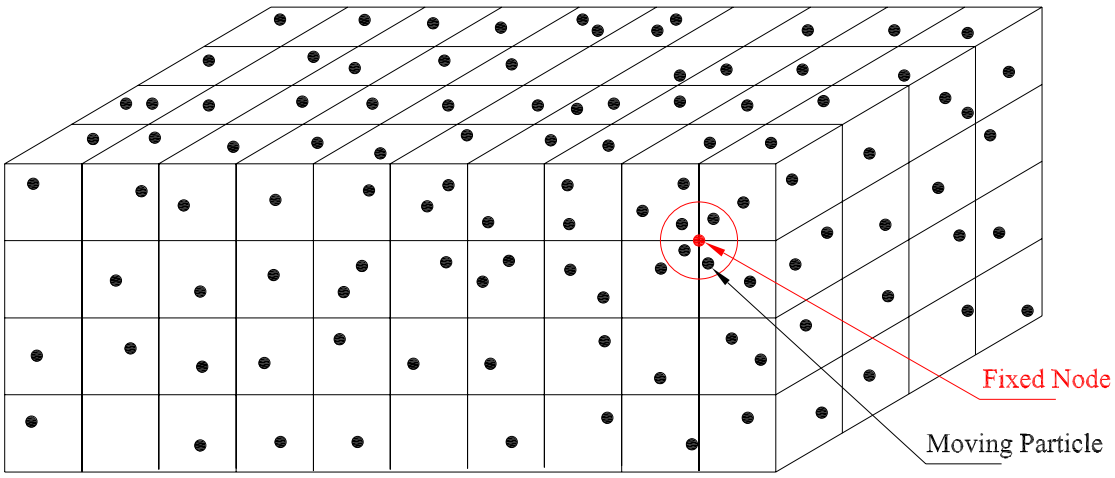

Figure 4.3: Schematic computational domain and the position of the fixed nodes and the moving particles

SPH interpolation of particle data onto a regular Cartesian grid is implemented in GPUSPH package as fixed nodes called TESTPOINTS. TESTPOINTS can act as gages from which velocity, pressure and other flow quantities can be measured at specific locations. In our model, TESTPOINTS are introduced on the entire domain with a resolution equal to the initial particle spacing. Mapping fluid information from scattered particles into Eulerian grid nodes is used to calculate depth-averaged

circulations. In addition, it improves post-processing analysis since it is easier to plot iso-surfaces, contour plots and data slices. The mapping onto the Eulerian grid is applied only periodically (typically every 10 time steps when output data is saved) so it does not impose an appreciable increase to the computational time.

4.4 Free-surface particles detection

A free-surface detection algorithm is used to find the free surface particles. Free surface particles need to be detected in order to accurately calculate the depth-averaged velocity profiles. The algorithm is based on the SPH kernel interpolation, making the method easy to implement and with little computational overhead since it uses the existing neighbor list of particles and the same kernel function for the interpolation. The free-surface tracking technique is similar to the algorithm proposed by Marrone et al. (2010) and Hérault et al. (2011) and is used at each time step of the numerical simulation. The free-surface detection algorithm consists of two steps: In the first step, a local normal vector for each particle is computed using the gradient of the kernel function. The normal vector for particle and components of kernel gradient can be defined as:

$$\vec{n_i} = \frac{\vec{v_i}}{|\vec{v_i}|} \tag{4.2}$$

$$\vec{v_i} = \sum_j \frac{m_j}{\rho_j} \nabla W_{ij} = \begin{cases} \sum_j \frac{m_j}{\rho_j} \frac{dW}{dr} \frac{1}{r_{ij}} (x_j - x_i) \\ \sum_j \frac{m_j}{\rho_j} \frac{dW}{dr} \frac{1}{r_{ij}} (y_j - y_i) \\ \sum_j \frac{m_j}{\rho_j} \frac{dW}{dr} \frac{1}{r_{ij}} (z_j - z_i) \end{cases} \tag{4.3}$$

where $\vec{n_i}$ is the normal vector, i corresponds to the particle of interest, j corresponds to the neighboring particle and r_{ij} is the distance between two particle i, j . In the second step, geometrical properties of free surface particles are used for their accurate detection. For each particle a cone is defined with particle's normal vector as its axis and a cone angle that has been set to be equal to $\frac{\pi}{6}$. Then a control check is applied to find whether or not at least one neighboring particle exists in this cone region. If no neighboring particle is found, then that particle belongs to the set of surface particles. This control condition is given as:

$$\forall_j, \frac{\vec{n_i}.(\vec{r_j} - \vec{r_i})}{r_{ij}} \succ \cos(cone - angle) \Longrightarrow i \in FreeSurfaceParticles \tag{4.4}$$

Figure 4.4 shows a schematic figure of free surface detection. In order to have more accurate detection, cone angle can be varied according to the position of the particle. For instance for the particles that are close to the boundary particles, a larger cone angle is used to avoid misdetection. The free surface computational CUDA kernel is composed of two loops over neighboring particles. In the first loop local normal vectors are computed and in the second loop, cone condition is checked to find whether or not the particle is on the free surface. This CUDA kernel is implemented in the "forces-kernel.cu" file of GPUSPH model.

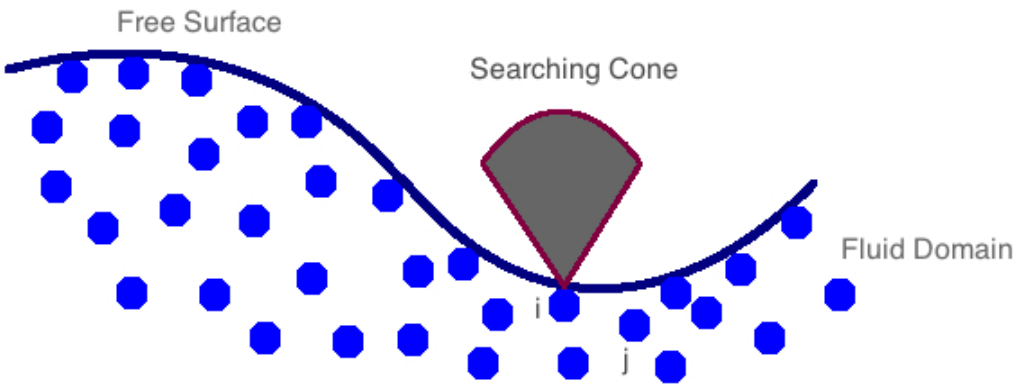

Figure 4.4: Schematic figure of the free surface detection

4.5 Numerical results and comparison with the experimental data

4.5.1 Mean horizontal circulations

The bar/rip channel system mentioned in the previous sections was simulated using the GPUSPH model. GPUSPH provides velocity components and position of moving particles. Other quantities, such as mean water level, three-dimensional

structure of underlying current field, trajectories of water particles, and the vorticity pattern corresponding to the wave-induced surf zone circulation are obtained by post-processing the numerical results. In this section, still water depth at the bar crest is set to 0.15 m, wave height is set to 0.19 m, and wave period is set to 1.5 s (similar to the test 1a of Drønen et al. 2002). The results are examined after the wave generator was running for at least 10 wave periods to eliminate start-up transient errors. Figure 4.5 shows a snapshot of waves computed during the numerical experiment.

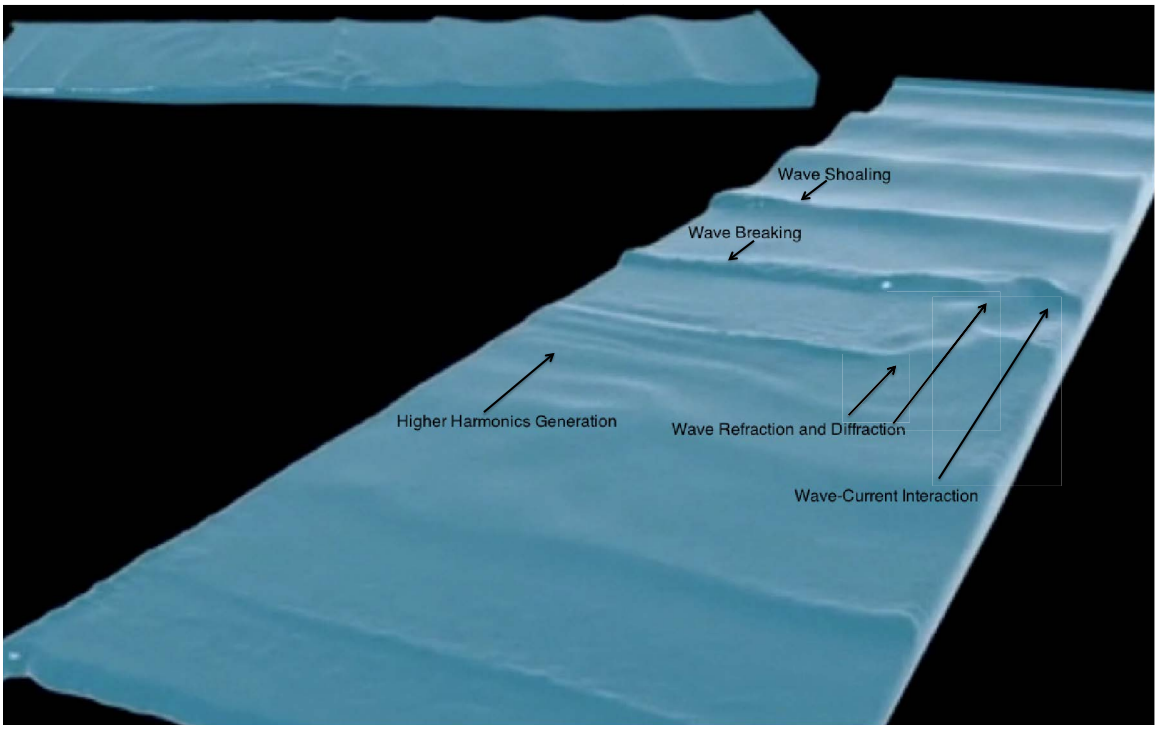

Figure 4.5: SPH numerical modeling of bar/rip channel system

This figure shows a side view (top part of figure) and a plan view (bottom of figure) of rip current system with a bar at almost middle left (bottom figure) and a rip channel at middle right of the wave tank (bottom figure). The wave generator

is located at the right hand side of the wave tank (top figure). Several interesting phenomena are observed from this figure:

1. Wave shoaling offshore of the bar and at the beach,

2. Wave breaking over the submerged bar,

3. Wave-current interaction in the rip channel,

4. Wave diffraction due to the channel,

5. Wave refraction due to depth changes,

6. Higher harmonics generation (Mei and Ünlüata, 1972) over the submerged bar.

Waves travel from the wave generator with nearly uniform crests until they reach the bar. On the sloping bar, wave shoaling and subsequent wave breaking is captured while there is almost no breaking in the rip channel. When the waves break, the change in wave radiation stresses forces a mean water level increase. Therefore the mean water level on the inshore side of the bar is higher than the mean water level in the rip channel and this gradient in setup drives alongshore current from behind the bar toward the channel (Dalrymple, 1978; Dalrymple and Lozano, 1978). Alongshore currents flowing from the bar into the channel act as feeders for the rip current flow, which travels in cross-shore direction towards the wave-maker. In the rip channel, the underlying current affects the surface wave train, leading to wave-current interaction. The numerical results predict alongshore variation of wave height due to the wave refraction by the rip current. The development of rip current and circulation cells causes the wave crest to be refracted as captured in the figure 4.5. When the

waves propagate over the inhomogeneous media and pass the submerged bar, due to nonlinearity, higher harmonics are generated and secondary wave crests appear in the surf zone. A snapshot of sea surface velocity (plan view), after 40 s of simulation time has passed (after about 27 wave periods), is given in Figure 4.6.

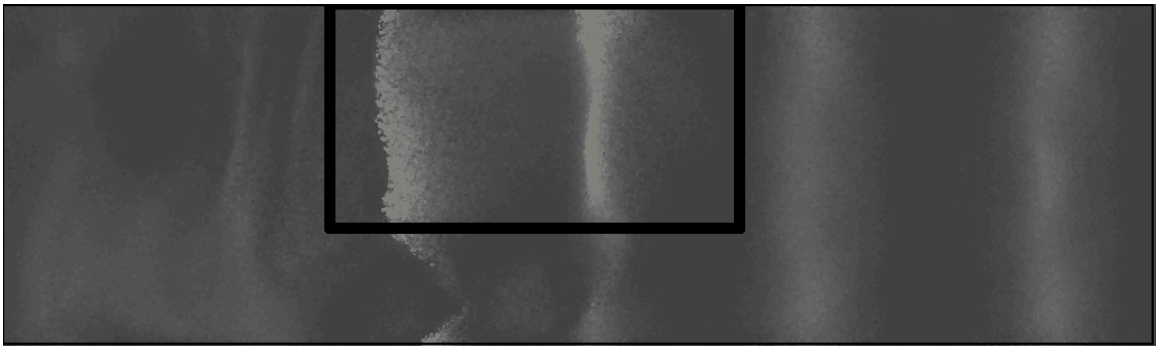

Figure 4.6: Sea surface velocity snapshot of the flow over the bar and over the rip channel at time = 40 s (Light color corresponds to higher velocity than the dark color)

Waves are traveling from the right hand side of the picture and the light color corresponds to higher velocities than the dark color. Breaking waves are shown over the submerged bar (inside the dark lines). As it can be seen in the figure, there is a non-uniform pattern of breaking waves on the bar that leads to differences in set-up and produces the cell circulation over the bar, which will be discussed later. Waves break more towards the landward edge of the bar (left hand side) so the resulting mean water level set-up in this region drives the main feeder of rip current in the channel. To find the horizontal mean velocity circulation, velocities are obtained at fixed, equally distributed positions (the Eulerian grid) over the water depth using

the SPH interpolation over neighboring moving particles. Then the velocities at the fixed nodes are integrated over the depth and also averaged over one wave period. Mean horizontal velocity distribution in both the numerical model and experimental model is given in figure 4.7. Note the experimental model data are only available from figures in the original article.

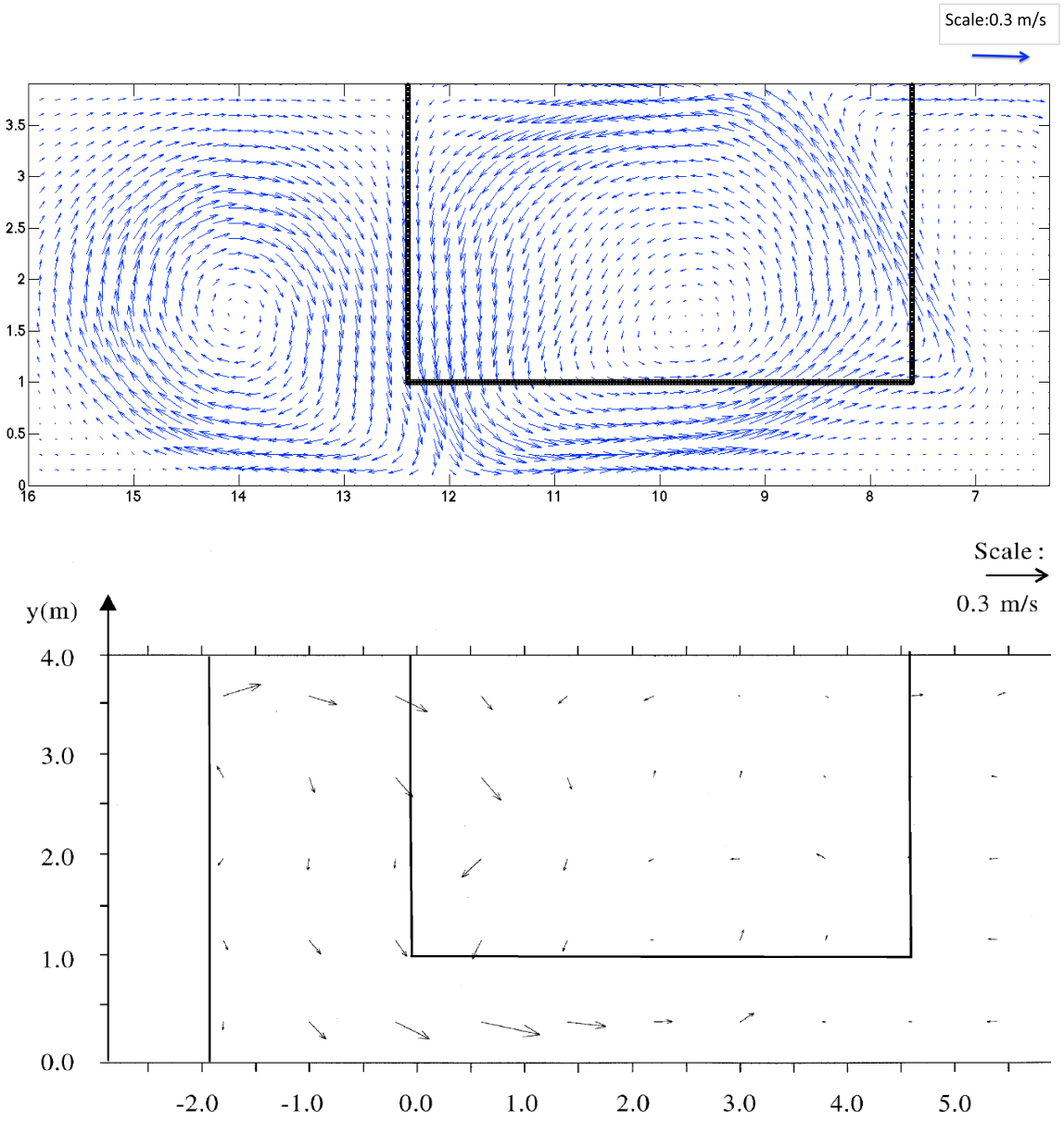

Figure 4.7: Mean horizontal velocity distribution. Top: Numerical results. Bottom: Experimental result (Drønen et al., 2002)–note the experimental data were measured up to 2 m of the onshore edge of the bar but the numerical data are computed up to the shoreline.

The flow pattern predicted by numerical model is similar to the measured velocity field. In this picture, the wavemaker is located outside of the figure to the right hand side and waves are traveling from right to the left. In the Drønen et al. (2002) experiment, the velocity, measured at one third of the depth, is considered to be the mean velocity but in numerical simulation, the actual mean velocity is obtained by taking the average of velocity over the water depth. The rip current system consists of an offshore-directed rip current in the channel, that does not extend beyond the offshore end of the rip channel, a circulation cell over the bar, and an onshore oppositely-rotating circulation cell as shown by the numerical results. The circulation cell over the bar appears due to differences in set-up over the bar and in the rip channel. As the waves travel toward the shore, they break over the submerged bar, while there is almost no breaking over the rip channel. After the bar, in the surf zone, waves at the shoreward end of the rip channel are larger since they have not been broken yet compared to the waves that travel over the bar, since they have already broken over the bar. The larger waves inshore of the channel lead to more intense breaking in the surf zone, creating another setup gradient, this time in the opposite direction as the setup gradient over the bar. Therefore a secondary opposite-rotating circulation occurs in the near-shore area. The second cell on the beach is also captured during the dye injections observations of Drønen et al. (2002) experiments. The rip current at the end of channel tends to move back onto the bar and join in the cell circulation over the bar region. This tendency has been also observed in the

experimental results (Drønen, et al. 2002). The mean water surface elevation is also measured numerically over one wave period after 40 s have elapsed in the simulation time and the results are compared with the experimental data. Mean surface gradients result in pressure gradients providing the driving force for rip currents in bar/rip channel systems as was discussed by Dalrymple et al. (2011). The differences in the wave breaking locations lead to a cross-shore gradient of mean free surface, as well. Figure 4.8 illustrates the mean surface water elevation and corresponding gradients.

On the left hand of the rip channel (onshore end of the rip channel) where the rip current is entering the rip channel, the surface elevation is higher than the surface elevation on the bar crest due to the wave-current interaction and the absence of wave breaking in the channel. The differences between contour plots of numerical and experimental results are related to the resolution differences. (Numerical resolution is equal to 0.02 m, whereas experimental data is measured over an area with a resolution of 0.8 m in the x-direction (cross-shore direction), and 0.6 m in the y-direction (alongshore direction).) In both numerical and experimental results, higher mean surface elevations can be captured at the onshore edge of the bar and the surf zone region. Lower mean surface elevation can be captured at the offshore edge of the bar and offshore edge of the rip channel. Numerical model is able to capture wave-current interaction at the entrance of the rip channel (onshore side of the rip channel), which leads to the higher mean surface elevation at that location. An aerial snapshot of the free surface elevation 40 s after start-up is shown in figure 4.9.

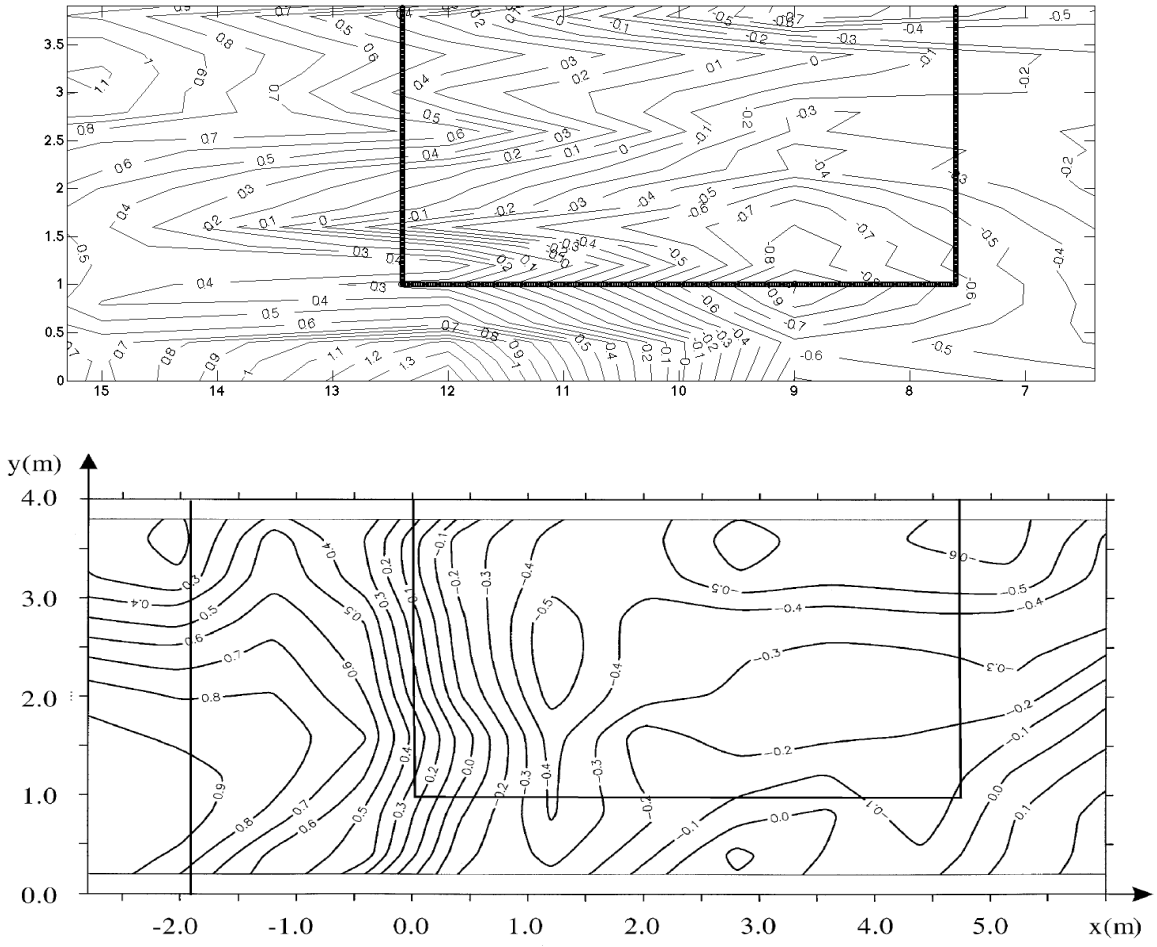

Figure 4.8: Mean surface elevation in cm. Top: Numerical results. Bottom: Experimental results (Drønen et al., 2002)

Waves are traveling from right to the left. The waves start shoaling and breaking on the bar but the waves keep their original shape over the channel until they reach the end of the channel in left hand side (onshore side of the channel). The wave-current interaction can be observed in the channel where the waves are refracted by the current. A pattern of refraction/diffraction caused by rip current can be observed. Waves begin to shoal and break behind the channel in the near-shore area, which

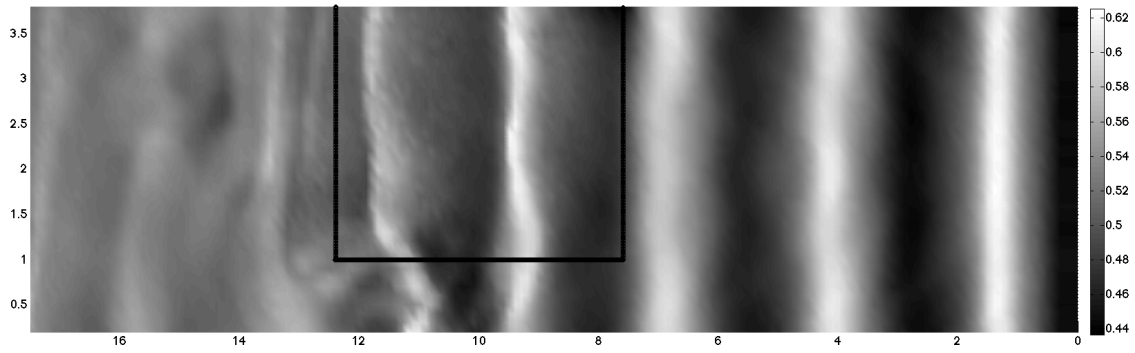

Figure 4.9: Free surface elevation at time = 40 s. Note the influence of the rip current on the wave crest at the bottom of the figure specifically the wave crest near x = 11 m.

lead to the secondary circulation in the surf zone. Figure 4.10 shows the depth- and period-averaged velocity and vorticity (unit of color bar for vorticity is $\frac{1}{s}$).

The black and white colors of vorticity denote clockwise (negative) and counter-clockwise (positive) rotations respectively. Vorticity is defined as $\Omega_\alpha = v_x - u_y$ where u and v are underlying mean current averaged over one wave period and the subscripts refer to the space derivatives. In both of the pictures, two main circulations: one over the bar (rotating counter-clockwise) and one near-shore (rotating clockwise) are observed but their strength and center of rotation are changing with time. Counter-clockwise vorticity, generated on the crest of the bar, is caused by the alongshore non-uniformity of wave breaking patterns on the bar crest. The mechanism of vortex generation is similar to the Peregrine (1997), Bühler and Jacobson (2001), Brocchini et al. (2004), and Kennedy et al. (2006) studies where generation of vorticity due

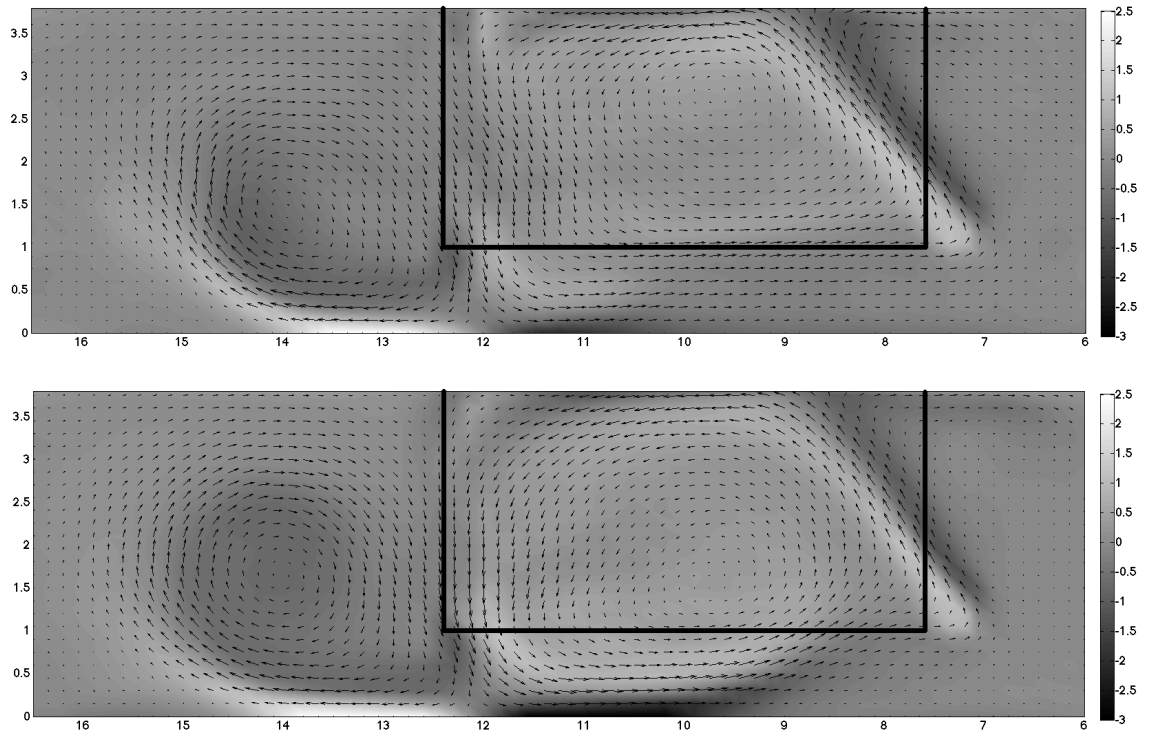

Figure 4.10: Mean vorticity ($s^{-}1$) and mean horizontal velocity vectors ($m.s^{-}1$) at two different times, top: T=20 s, bottom: T =40 s

to the forcing of water waves is studied in the surf zone region. Clockwise vorticity located in surf zone is generated due to larger setup shoreward of the rip channel in comparison with the setup shoreward of the bar. Two minor circulations: one on the up-right hand side of the bar circulation (in the opposite direction of it) and one on the left-down side of near-shore circulation (in the opposite direction of it) can also be observed. Strong vorticity near rip-current sidewall are due to the presence of the tank sidewalls as opposed to a line of symmetry.

4.5.2 Three-Dimensional variation of flow structure, particle trajectories, and cross-shore velocity components

The three-dimensional distribution of wave-averaged horizontal velocity profiles is given in figure 4.11.

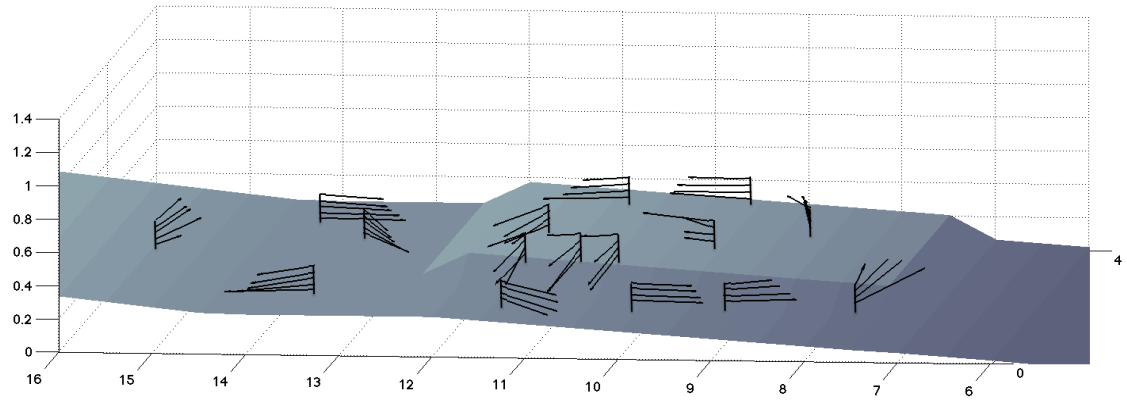

Figure 4.11: Three-dimensional velocity profiles averaged in one wave period, 40 seconds after the start-up of the model.

The figure shows, at inshore side of the bar, the flow is traveling in the alongshore direction from the bar into the rip channel. The lateral flow is non-uniformly distributed in the vertical direction and the reason can be related to the sudden increase in the water depth from the submerged bar into the trough shoreward of the bar. The rip current has a tendency to be stronger closer to the bed in the entrance of the rip channel but the current move toward the surface at offshore end of the

channel due to the increase in depth (Arthur, 1962). On the bar crest and also the entrance point of the rip channel, where trough and rip channel meet, the direction of flow is non-uniform and is dependent on the vertical position, suggesting that three-dimensional effects and rotations are important in the dynamics of rip current system development. The trajectory of several particles that were initially located in different positions over the bar and in the surf zone at the half water depth, have been tracked as figure 4.12.

Particle tracking is started from time = 40 s and has been recorded every 0.1 s. It can be observed that some particles over the bar enter the circulation and then flow into the rip channel, while others flow to the surf zone and enter the secondary circulation. The particle that enters the channel tends to go toward the surface as it approaches the offshore side of the channel due to wave-current interaction. The particle that was initially in the surf zone seems to stay there and keeps rotating in the clock-wise direction indicating little exchange between the inshore and the offshore. Similar field observations were reported by MacMahan et al. (2010) and Reniers et al. (2010). Cross-shore velocities in alongshore direction of the rip channel at the position of x = 11.4 m and one third of the water depth are numerically computed and compared with the experimental results. Numerical results are compared to test 3* of Drønen et al. (2002) experiments, where the still water depth at the bar crest is equal to 0.1 m, wave height is set to 0.15 m and wave period is set to 1.5 s. Test 3* has been chosen since experimental data of alongshore variation of cross-shore velocity

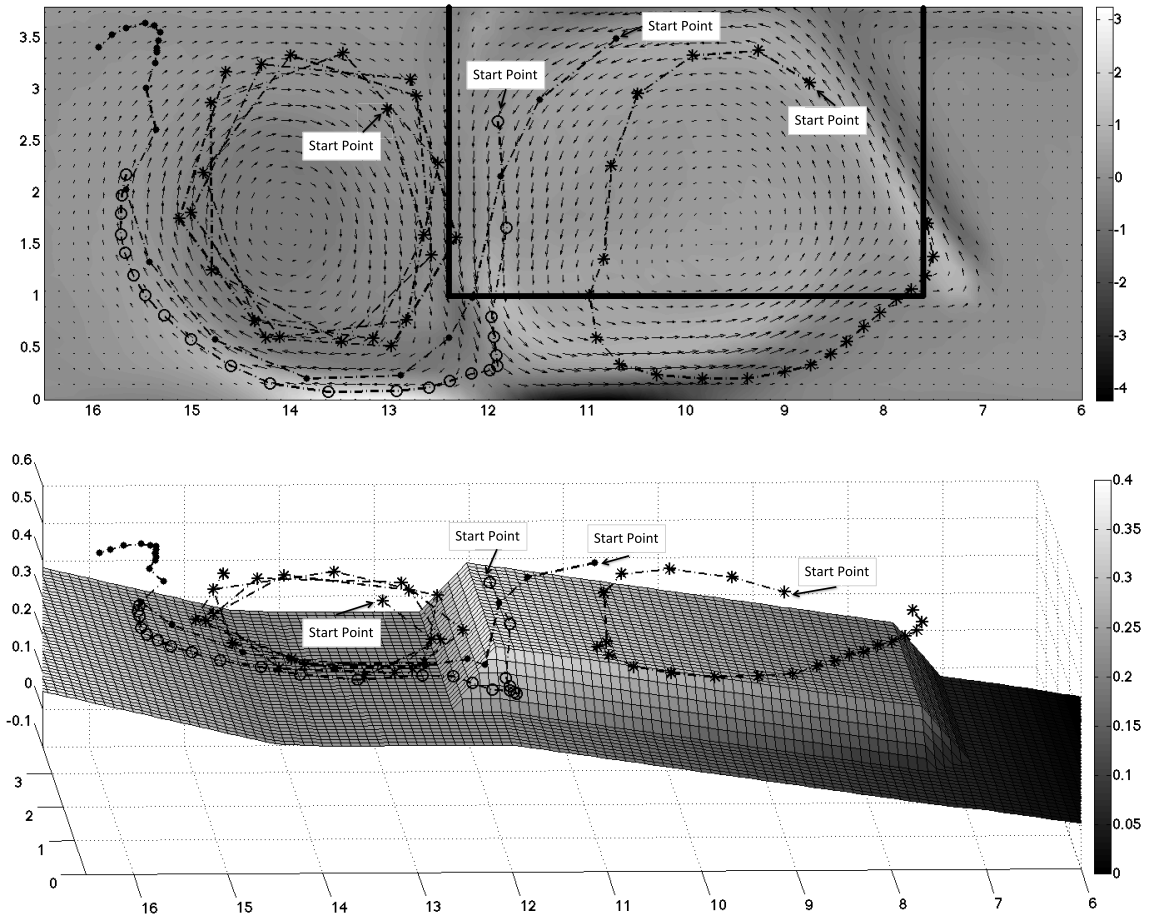

Figure 4.12: Mid-depth Particle Trajectories. Top: Top view; Bottom: Three-dimensional View

in the rip channel are measured in this set of test. Figure 4.13 shows the numerical and experimental results of the cross-shore velocities. Numerical and experimental values show good agreement except the ones very close to the sidewalls (one sidewall is at y = 0 and the bar sidewall is at y = 0.9). The velocity profiles very close to the sidewalls follow the boundary layer problem and need further studies.

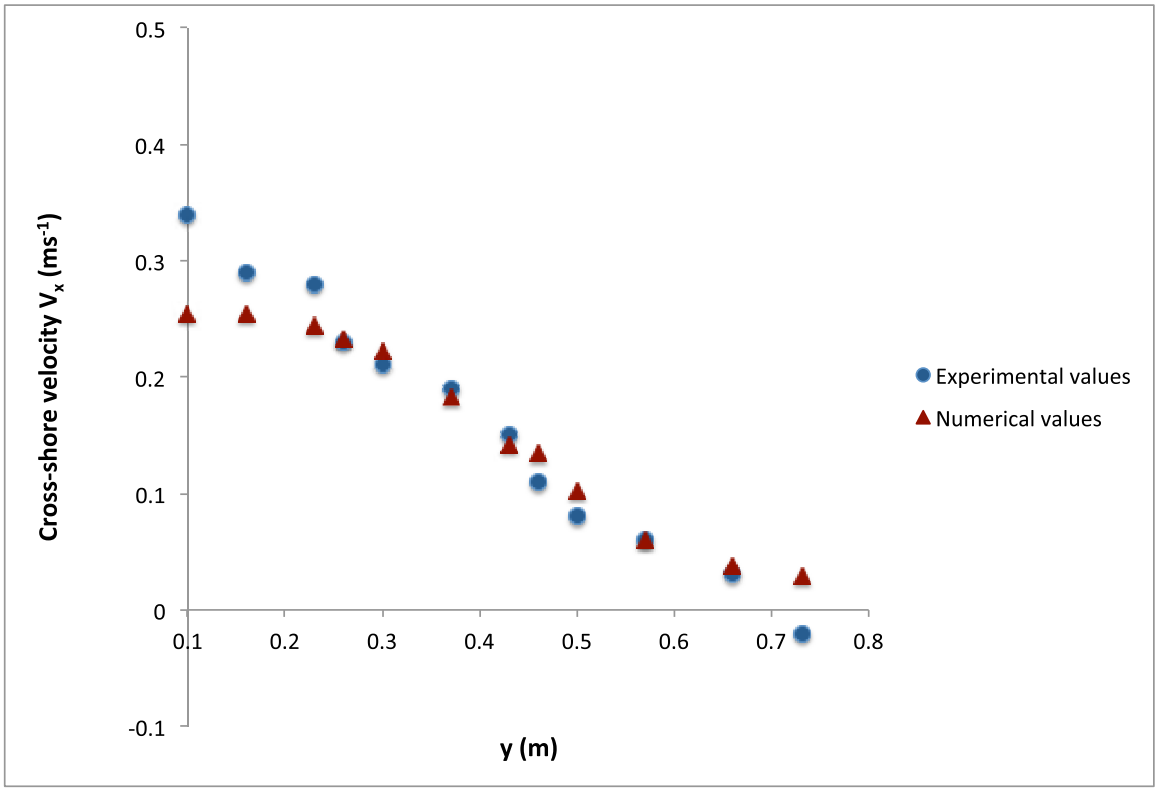

Figure 4.13: The cross-shore velocity as a function of alongshore position at x=11.4 m, at one third of the depth from the bed. Experimental values are from test 3* (Drønen et al., 2002)

4.6 Effect of SPH Particle Resolution

In order to find the effect of SPH initial particle spacing, different particle resolution is used to model the bar/channel rip current system. Particle spacing of 0.02, 0.021, 0.022, 0.023, 0.024, 0.025, 0.03, and 0.04 m are used. In all of the cases, circulations can be observed over the bar and in the surf zone area but rip current intensity is much lower in the cases with 0.03 m and 0.04 m particle spacing. In the case of

0.04 m particle spacing, almost no rip current occurs in the rip channel. In order to have a quantitative comparison, the cross-shore velocities in alongshore direction of the rip channel are numerically computed using different initial particle spacing and the results are compared with the experimental data using mean squared errors. The mean squared errors between the numerical results and experimental results are computed as figure 4.14 using the following equation:

$$MSE = \frac{1}{n}\sum_{i=1}^{n}[(\hat{v_x})_i - (v_x)_i]^2 \tag{4.5}$$

where $\hat{v_x}$ refers to the numerical data of cross-shore velocities shown in figure 4.13, v_x refers to the experimental data of cross-shore velocities shown in figure 4.13, and n is the number of cross-shore velocities data in different y-position of the rip channel. The two data points, which one is very close to the left wall of the rip channel and the other is very close to the right wall, are not considered in this analysis since the current resolution of the numerical simulation is not capable of modeling the boundary layers close to the side walls. The errors decrease by the decrease of particle spacing until the particle spacing is equal to 0.022. Below this magnitude, the mean squared error is nearly constant with the decrease of the particle spacing. Therefore particle spacing equal to 0.022 can be chosen as the maximum particle size for this simulation. The numerical results of cross-shore velocity on different positions along the rip channel show a good agreement with the experimental results and the mean squared error is equal to 0.002.

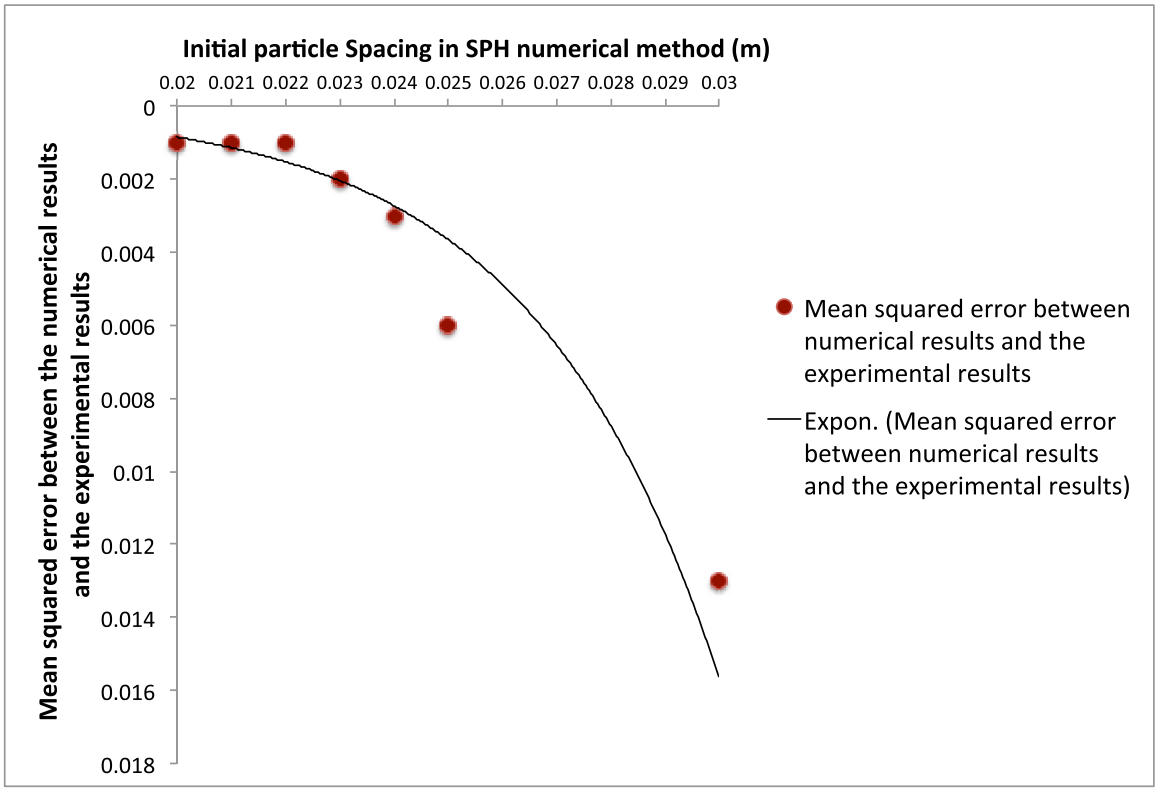

Figure 4.14: Effect of the initial particle spacing on the mean squared error between numerical results and experimental results. Experimental results are obtained from the cross-shore velocity values in test 3* (Drønen et al., 2002)

4.7 Radiation stress in the surf zone and in a bar/rip channel system

Wave set-up and wave-induced circulations are the results of the changes in the wave radiation stresses. In this section variation of radiation stress due to the wave breaking is investigated. First, the radiation stresses correspond to the wave breaking in a wave tank with no alongshore bathymetry variation is studied. Then, different

components of the radiation stresses in a bar/rip channel system will be investigated. At the end, the effect of alongshore bathymetry variation on the radiation stresses is discussed.

4.7.1 Variation of radiation stress in the surf zone

In this section, the propagation of water waves over a bathymetry, which has no variation in the alongshore direction, will be investigated. Longuet-Higgins and Stewart (1960) defined the radiation stress S_{xx} as the excess flow of momentum due to the presence of the waves:

$$S_{xx} = \overline{\int_{-h}^{\zeta} (P + \rho u^2) dz} - \int_{-h}^{0} P_0 dz = \overline{\int_{-h}^{\zeta} (P + \rho u^2) dz} - \frac{1}{2}\rho g h^2 \tag{4.6}$$

where the over-line shows the mean value with respect to a wave period, u is the cross-shore velocity, ζ is the surface elevation, and $-h$ is the bottom elevation. Using the dispersion relation and velocity components equations, Longuet-Higgins and Stewart (1960) showed that the radiation stress associated with the horizontal momentum across a vertical plane could be simplified (correct to second order in ka)

$$S_{xx} = E(\frac{2kh}{\sinh(2kh)} + \frac{1}{2}) \tag{4.7}$$

where k is the wave number, a is the wave amplitude, and E is the total wave energy . In this equation, total energy can be calculated using the wave height (H) at different locations along the wave tank as:

$$E = \frac{1}{8}\rho g H^2 \tag{4.8}$$

Wave number k can be calculated using the dispersion relation as:

$$\sigma^2 = gk\tanh(kh) \tag{4.9}$$

The transverse component of the radiation stress (S_{yy}) is defined as the excess flux of momentum in y-direction (direction parallel to the wave crests) across a plane y = constant

$$S_{yy} = \overline{\int_{-h}^{\zeta}(P+\rho v^2)dz} - \int_{-h}^{0}P_0 dz = \overline{\int_{-h}^{\zeta}(P+\rho v^2)dz} - \frac{1}{2}\rho g h^2 \tag{4.10}$$

where v is the transverse component of velocity in y-direction. Similar to S_{xx}, S_{yy} can be presented (correct to second order in ka) as:

$$S_{yy} = E(\frac{kh}{\sinh(2kh)}) \tag{4.11}$$

The radiation stress component S_{xy}, which indicates excess flow of x-momentum across a plane y = constant is presented as:

$$S_{xy} = \overline{\int_{-h}^{\zeta}(\rho uv)dz} \tag{4.12}$$

Radiation stress component S_{xy} and S_{yx}, which indicates excess flow of x-momentum across a plane y = constant and excess flow of y-momentum across a plane x = constant, are equal to zero in a progressive wave problem where the waves approach the shore in a normal direction to the shore since $\overline{uv}$ vanishes. The variation of radiation stress in a wave breaking system has been studied in a wave tank with the same dimensions mentioned in the previous sections but no bar is located at the

bottom of the tank, representing the propagation of water waves over a bathymetry that has no variation in the alongshore direction. Wave parameters are similar to the test 3* of Drønen et al. (2002) experiment. (Still water depth at the bar crest is equal to 0.1 m, wave height is set to 0.15 m and wave period is set to 1.5 s) The effect of wave reflections from slopes can be observed over the sloping parts of wave tank bottom. Figure 4.15 presents the mean water level over the length of the tank (being ensemble-averaged over the width of the tank). As it is shown in this figure, oscillatory behavior can be observed at the position of bottom slopes. Set-up and set-down is also captured in this figure close to the shoreline.

The SPH numerical method computes velocity and pressure at the Lagrangian particles. Then the fluid parameters are mapped on to the Eulerian grid. Pressure and velocity at the fixed positions along the depth of the tank have been computed. For each position, the total x-momentum flux in the presence of the waves is computed. Then the radiation stress is obtained as the subtraction of total momentum flux in the presence of the waves minus the total momentum flux in the absence of the waves. The numerical results are compared with the theoretical result given by equation 4.7. Figure 4.16 illustrates the comparison of numerical and theoretical result of radiation stress along the length of the tank. The first term of equation 4.7 is the total energy and it is proportional to the wave height, which slightly decreases as it approaches the shore due to the viscous dissipation. On the other hand, the second term of equation 4.7, $(\frac{2kh}{\sinh(2kh)} + \frac{1}{2})$, increases as the wave approaches the shore as the water depth

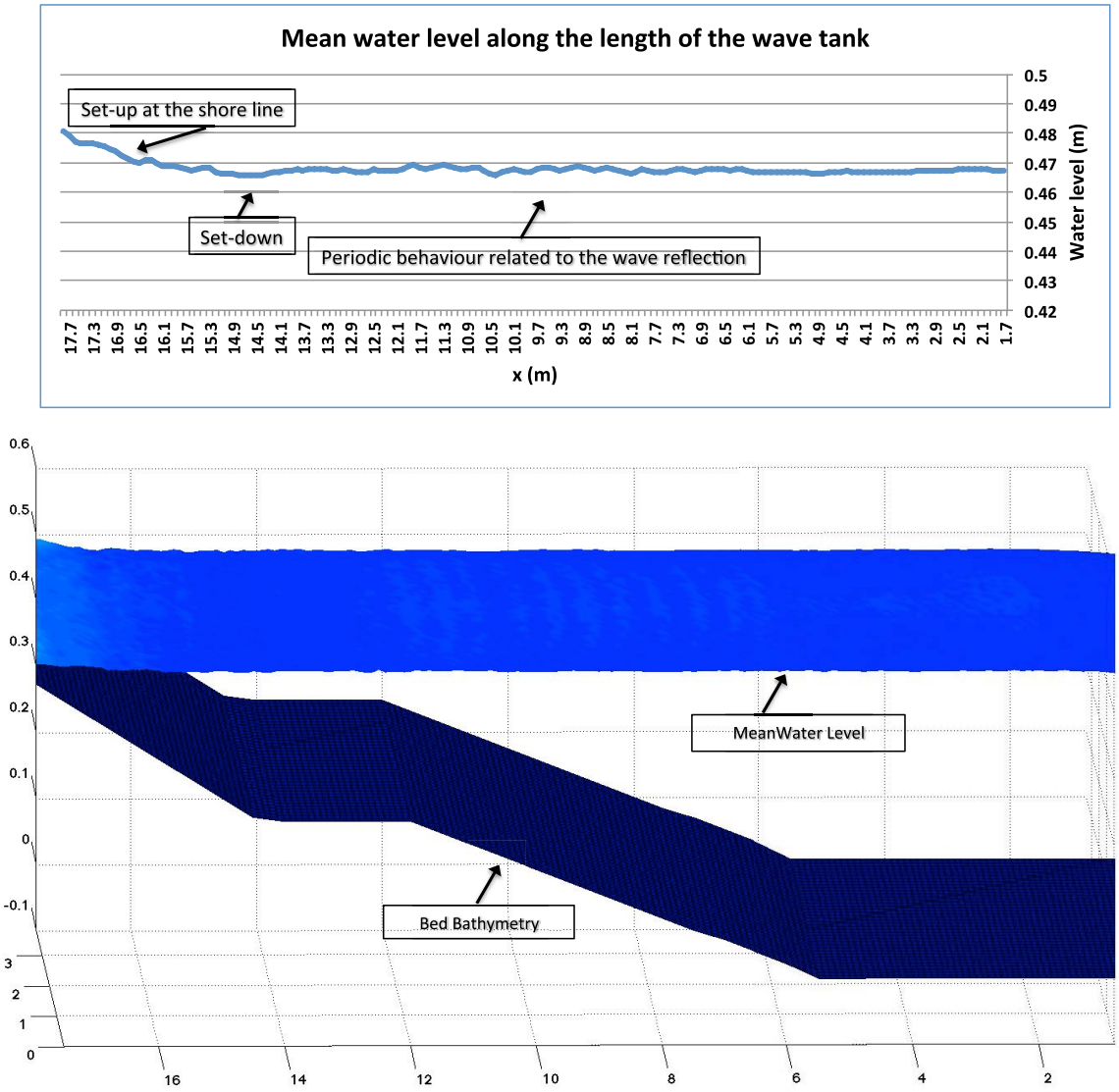

Figure 4.15: Mean water level over one wave period (when 20 s of simulation time has passed). Top: Ensemble-averaged mean water level over the width of the tank. Bottom: Mean Water level and the bed bathymetry

decreases. It can be observed from figure 4.16 that the first term dominates most of the time. The computed radiation stress oscillates some over the slopes, which is related to the reflection of the waves on those regions. At x = 14 m a drop of the

numerical radiation stress is observed that is related to the wave breaking at that position.

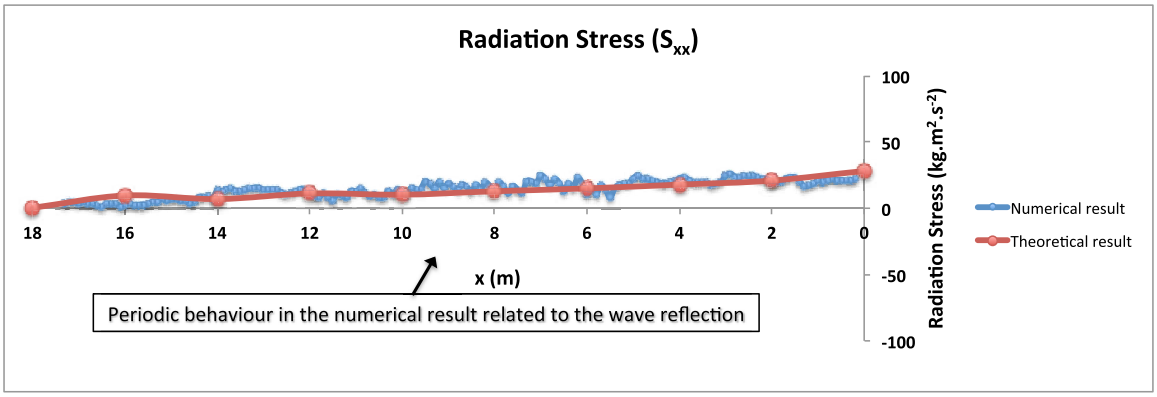

Figure 4.16: Comparison of the numerical and theoretical results of the radiation stress along the length of the tank

4.7.2 Radiation stress in a bar/rip channel system

In the previous section the radiation stresses correspond to the wave breaking in a wave tank with no alongshore bathymetry variation has been studied. In this section, different components of the radiation stresses in a bar/rip channel system will be investigated. This case represents the propagation of water waves on a bathymetry, which has variation in the alongshore direction. Wave parameters are the same as the previous section (Still water depth at the bar crest is equal to 0.1 m, wave height is set to 0.15 m and wave period is set to 1.5 s). The bed bathymetry is shown in figure 4.2. Similar to equation 4.6, numerical values of radiation stress component S_{xx} is computed by taking the time average of the excess flow of momentum due to

the water waves as:

$$\overline{\sum_j (\rho_j (u_j - U_j)^2 + P_j) \times dz} - \frac{1}{2}\rho g h^2 \tag{4.13}$$

where, u_j is the x-component of total velocity and U_j is the x-component of mean velocity (current velocity) at each numerical node. Current velocities are computed by finding time-averaged velocities over one wave period and the current velocities are subtracted from the total velocities. Figure 4.17 presents the radiation stress component S_{xx} along the tank in the position of the rip channel (being averaged from y = 0 to y = 1). It can be observed that at the wave breaking positions, we have a drop in the radiation stress. By comparing figure 4.17 and figure 4.16, one can observe

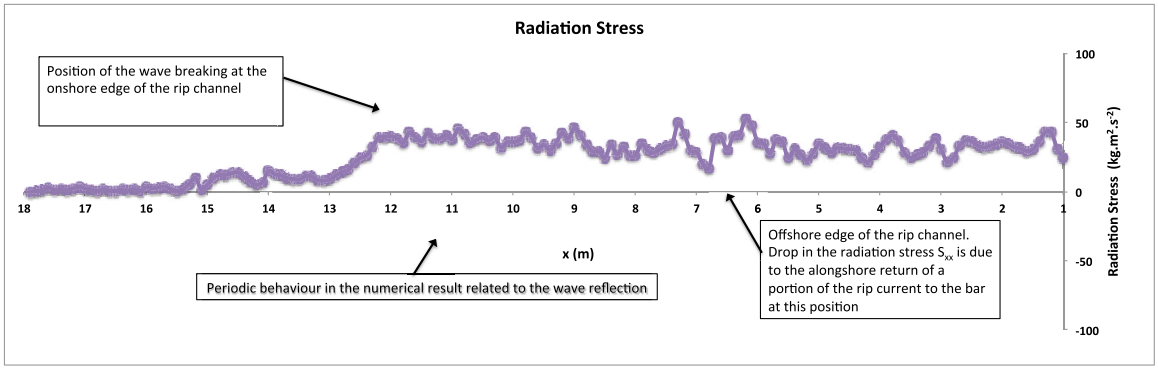

Figure 4.17: Radiation stress S_{xx} along the wave tank at the position of the rip channel (averaged from y = 0 m to y = 1 m)

a different behavior of the radiation stress in the bar/rip channel system because of the wave-current interaction. In the case with no variation of bed bathymetry in the alongshore direction (figure 4.16), radiation stress has a slightly decreasing behavior in x-direction along the tank due to the energy dissipation but in the bar/rip channel

case (figure 4.17) the mean radiation stress increases in the rip channel. This behavior is due to the wave-(rip) current interaction that results in higher wave heights in the rip channel and consequently higher wave energy that increases the radiation stress there. The increase in radiation stress is due to the work that is done by the current on the wave (this concept will be discussed more in the next section). The oscillation observed in the radiation stress is related to partial wave reflection from the bottom slope. At the shoreward end of the rip channel, waves are breaking and we have a drop in radiation stress. When the waves break, they splash up giving an increase in radiation stress until they overturn and break again. That is the reason for the radiation stress fluctuations at the end of the rip channel. Looking at the steady y-component of the conservation of momentum equation, in the absence of wave flow in y-direction, y-component of momentum flux can be presented as (Longuet-Higgins and Stewart (1964)):

$$-g\underbrace{\frac{\partial\bar{\zeta}}{\partial y}}_{\text{Term-one}}-\frac{1}{\rho(\bar{\zeta}+h)}\Big(\underbrace{\frac{\partial S_{yy}}{\partial y}}_{\text{Term-two}}+\underbrace{\frac{\partial S_{yx}}{\partial x}}_{\text{Term-three}}\Big)+R_y=0 \tag{4.14}$$

where R_y corresponds to the viscous term. Alongshore variation of the radiation stress component S_{xx} in the position of the bar/rip channel results in alongshore variation of set-up, which is presented as Term-one in equation 26. Radiation stress component S_{yy} is also calculated using equation 4.10 as:

$$\overline{\sum_j(\rho_j(v_j-V_j)^2+P_j)\times dz}-\frac{1}{2}\rho g h^2 \tag{4.15}$$

where v_j is the y-component of total velocity and V_j is the y-component of mean velocity (current velocity) at each numerical node. Parameter j refers to the discrete numerical nodes laying along the depth of the tank and dz is the vertical distance between two consequent nodes. Variation of S_{yy} along the width of the tank at x = 11 m is presented in figure 4.18. Higher values of component S_{yy} can be captured along the rip channel in comparison to the lower values along the bar.

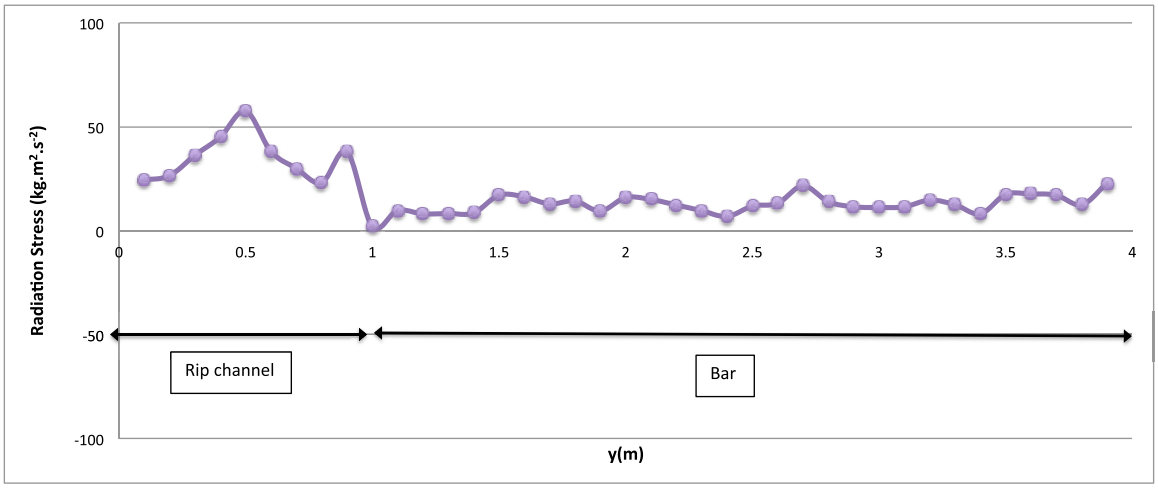

Figure 4.18: Radiation Stress S_{yy} along the width of the tank (x = 11 m)

Radiation stress component S_{yx} and its variation along the length of the tank, which refers to the Term-three of the equation 4.14, have also been calculated as:

$$\overline{\sum_j (\rho_j (v_j - V_j)(u_j - U_j)) \times dz} \tag{4.16}$$

Component S_{yx} has non-zero value at the entrance of the rip channel but its gradient in x-direction is much smaller than Term-one and Term-two of the equation 4.14 and can be neglected. Reduction of S_{xx} over the bar leads to higher set-up and

consequently higher mean water level in that area (Figure 4.18). Therefore alongshore variation of mean water level occurs between bar and rip channel, which is related to the Term-one in the momentum flux equation 4.14. This unbalance of mean water level leads to a change in radiation stress component, which increases towards the rip channel (Term-two of equation 4.14 and figure 4.18) and drives a force to carry water towards the rip channel. This force acts as a feeder for the rip current.

4.8 Wave-Current interactions and variation of wavelength and wave height

When water waves travel over a non-uniform current, changes occur in their length, amplitude and direction. The current does additional work on water waves at a rate of $\gamma_{ij}S_{ij}$, where γ_{ij} is the symmetric strain rate tensor associated with the current and S_{ij} is the radiation stress tensor (Longuet-Higgins and Stewart, 1960). For steady currents, the following energy flux equation is:

$$\nabla.[E(c_g + U)] + \frac{1}{2}S_{ij}(\frac{\partial U_i}{\partial x_j} + \frac{\partial U_j}{\partial x_i}) = 0 \tag{4.17}$$

where c_g is the wave group velocity and U is the current velocity. This equation indicates that in addition to the energy propagation with a velocity of $c_g + U$, an interaction occurs between waves and current with a rate of $\gamma_{ij}S_{ij}$. In order to study

wavelength variations of the water waves due to the rip current, we considered conservation of waves equation, which indicates that temporal variation of wave number vector is balanced by the spatial variation of wave angular frequency:

$$\frac{\partial k}{\partial t} + \nabla\sigma = 0 \tag{4.18}$$

For steady state problems, $\frac{\partial k}{\partial t} = 0$, therefore $\nabla\sigma = 0$ and angular frequency is constant in space. If waves encounter a current:

$$\sigma_0 = \sigma + \vec{k}.\vec{U} \tag{4.19}$$

where σ_0 is computed in an area where no current exists. Using dispersion relation ($\sigma^2 = gk\tanh(kh)$) and considering the fact that rip current is mostly uni-dimensional in the rip channel, equation 4.19 can be written as:

$$\sqrt{gk_0\tanh(k_0h_0)} = \sqrt{gk\tanh(kh)} + k.U \tag{4.20}$$

This equation has been solved for wave number (k) at the middle of the rip channel and results are given in figure 4.19.

Still water depth at the bar crest is set to 0.15 m, wave height is set to 0.19 m, and wave period is 1.5 s. In figure 4.19, wave number stays constant until the rip channel. In the rip channel, interaction of waves and rip current results in an increase in the wave number and therefore a decrease in wavelength. After the rip channel, wave number decreases until it enters the shallow water and increases consequently. The decrease of wavelength in the rip channel can also be observed in the snapshot

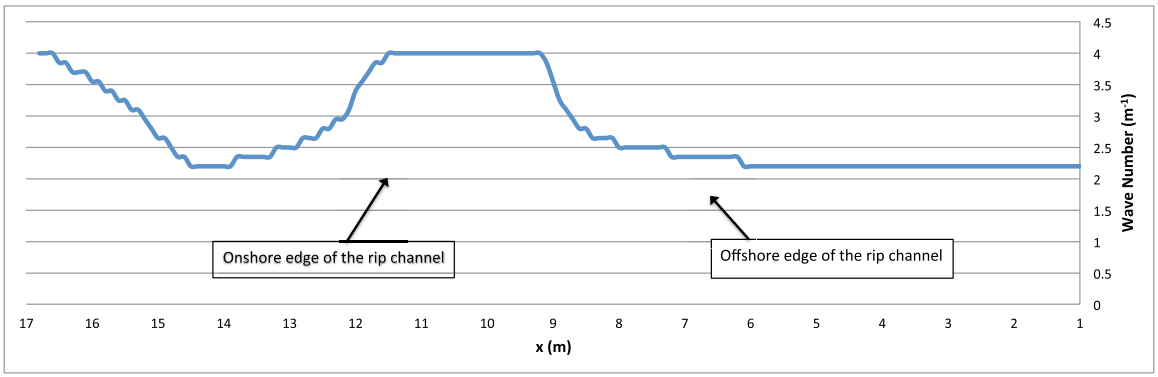

Figure 4.19: Wave-Current interaction and variation of wave number at the middle of the rip channel (y = 0.5 m)

of water wave given in figure 4.9. The wave number variation from equation 32 was compared with the wave number relationship, which was suggested by Longuet-Higgins and Stewart (1960) for deep water. Our result predicts higher wave number since in our problem waves travel over intermediate and shallow water. Variation of wave height in the rip channel has been studied and illustrated in figure 4.20. Wave-current interaction increases the wave height close to the offshore entrance of the rip channel.

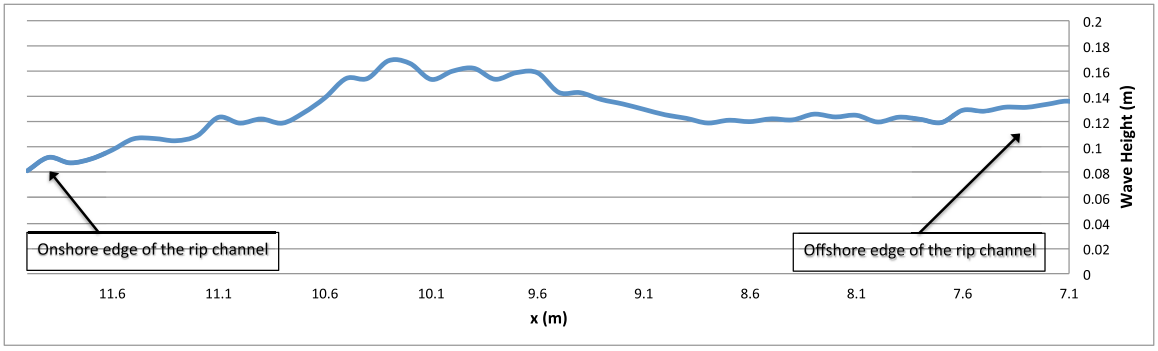

Figure 4.20: Variation of wave height along the rip channel at y = 0.5

Chapter 5

Three-dimensional horseshoe vortex structures under a broken solitary wave

5.1 Introduction

The turbulence associated with water wave breaking can play a crucial role in sediment transport, wave damping and mixing processes beneath the free surface. The transfer of heat and mass due to the mixing processes can be vital for water quality and aquatic life. In addition, the vortex structures and rotations associated to the water wave breaking can have a dominant effect on the safety of vessels and structures located in the surf zone (Banner and Peregrine, 1993).

CHAPTER 5. THREE-DIMENSIONAL HORSESHOE VORTEX STRUCTURES UNDER A BROKEN SOLITARY WAVE

In the laboratory, Nadaoka et al. (1989) performed an experimental study of the periodic spilling waves breaking on a plane beach. The experiments were conducted in a 0.6 m deep, 0.4 m wide, and 20 m long wave channel, equipped with a flap-type wave generator.They found two-dimensional large-scale spanwise vortex structures under breaking waves with axes parallel to the crest line. Behind the wave crest, three-dimensional obliquely descending eddies were observed. The experiments revealed that these vortex structures posses large amounts of vorticity (with non-zero average) in otherwise almost irrotational velocity fields. They called the breaking waves as "pseudowaves" and decomposed the velocity field into two components: irrotational velocity component (wave motion) and rotational mean velocity component (eddying motion). By inversely computing the water surface profile corresponding to the irrotational velocity component only, they found that the water surface elevation decreases in the presence of the rotational velocity component. Flow visualization was conducted using air bubbles entrained through the wave breaking process and strong three-dimensionality of the flow structure was observed behind the wave crest. Ting and Kirby (1994, 1995, 1996) conducted a series of experiments regarding the dynamics of surf-zone turbulence under plunging and spilling breakers. Experimental results revealed that the turbulent kinetic energy is transported landward under a plunging breaker and is dissipated within one wave cycle, whereas the turbulent kinetic energy is transported seaward under a spilling breaker and the dissipation rate is much slower. Chang and Liu (1998, 1999) measured fluid particle velocities for

breaking waves in a laboratory. The results indicated that the turbulence advection, production, and dissipation were equally important, while the turbulence diffusion was almost negligible. Downstream from the breaking point, the turbulence production and dissipation were of the same order of magnitude, but not identical. Cox and Kobayashi (2000) measured the instantaneous horizontal and vertical turbulent velocities induced by spilling waves and concluded that the turbulence generated by wave breaking was an order of magnitude larger than the turbulence generated at the boundary layer. Cox and Anderson (2001) performed particle image velocimetry (PIV) measurements to capture size and vorticity of the coherent structures produced by regular waves breaking on a plane slope in a two-dimensional wave flume. They observed vortices with axis of rotation in the vertical direction at the toe of the broken wave as well as obliquely descending eddies. Melville et al. (2002) performed a digital particle image velocimetry (DPIV) measurement of the velocity field under breaking waves. They found that the breaking wave generates at least one coherent vortex structure, which slowly travels in the wave direction. They also found that the kinetic energy of the flow, turbulent Reynolds stresses and the vorticity decay approximately as t^{-1}, where t is the time. Cox and Shin (2003) conducted laboratory measurements to study the void fraction fluctuation in the aeration region of the breaking waves. The temporal variation of the void fraction was modeled by linear growth followed by exponential decay. Ting (2006) performed an experimental study of large-scale turbulence under a solitary wave. In this study, another type of coher-

ent structures, called downbursts, were detected as well as the obliquely descending eddies. Sou et al. (2010) implemented Particle Image Velocimetry (PIV) measurements for plunging breaking waves. They reported that a shear layer occurs when the uprush of the bore front interacts with the downwash flow. The spatial evolution of turbulence shows that the turbulence generated by the shear layer grows from the outer to the inner surf zone regions but becomes insignificant once the bore collapses in the swash zone.

In terms of numerical studies, Lin and Liu (1998) developed a two dimensional RANS numerical model to study the wave propagation and breaking in the surf zone. They reported the existence of a 'roller' region in the breaking wave front, which is a source region of turbulence generation. Watanabe et al. (1999) used a three-dimensional large-eddy simulation (LES) method to study the large-scale vortex structures under spilling and plunging breakers. Christensen and Deigaard (2001) and Christensen (2006) performed a LES method to model spilling and plunging breakers. The order of magnitude of the turbulent energy was found to be in agreement with experimental results.

As mentioned before, coherent vortex structures under and behind the broken water waves including spanwise rollers, downbursts, and obliquely descending eddies have been investigated in various studies but the physical explanation of their generation, configuration and propagation need further studies. Svendsen (1987) measured the turbulent kinetic energy under surf zone waves and detected a strong vertical

mixing attributed to the large scale turbulent vortices. Battjes (1988), in his review paper, discussed the transition of irrotational flow to rotational flow in the breaking waves region and the role of breaker types (spilling, plunging, and collapsing) on the vortex structures. Banner and Peregrine (1993), in their annual review paper, described the turbulence behind the breaker as a turbulent wake. They indicated that in a wave-moving frame of reference, the turbulence is primarily generated in the toe region, from where it spreads back as a wake that contains the momentum lost from the breaking process. In a fixed frame of reference of surf zone, a shear flow can be observed associated with the shoreward flow above the trough level and an undertow returning water towards the seaward direction. Li and Dalrymple (1998) discussed that the instabilities of the undertow lead to large offshore vortex train previously captured by Matsunaga et al. (1988, 1944). Watanabe et al. (2005) described obliquely descending eddies as rib structures, which have counter-rotating streamwise rotations. The re-orientation of perturbations in the primary vorticity results into the streamwise vortex structures. They described the initiation of the three dimensional instability and the resulting formation of the rib structures.

In this chapter, we studied the coherent vortex structures generated under and at the back of a broken solitary wave in two cases of spilling and plunging breakers. The reason behind studying a single breaking wave is that the wave breaking process and the generation and evolution of the associated three-dimensional vortex structures can be investigated separately from the effect of returning undertow flow and the

residual turbulence induced from previously broken waves in the case of periodic waves discussed in the next chapter. Further, a solitary wave is a first approximation to a tsunami wave.

The three-dimensional Smoothed Particle Hydrodynamics (SPH) method is used to numerically model the broken wave and related turbulent fields. The objectives of this study are to quantify the geometric features of generated coherent structures and to show their role in turbulent momentum and kinetic energy transportation to the deeper portions of the water column. For this purpose the instantaneous flow field is investigated and a coherent structure detection method is applied to capture the organized vortex structures.

5.2 Wave tank set-up

A 3D numerical simulation has been conducted to study the turbulent flow structures under a laboratory-scale solitary breaking wave.The wave tank set-up used in the numerical model was inspired by the solitary wave experiments of Ting (2006). The laboratory experiments were performed in a 25 m long, 0.9 m wide flume on a 1 in 50 plane slope. A piston type wave generator was located at the end of the tank in front of a wave absorber and the water depth was 0.3 m in front of the wave generator. Figure 5.1 illustrates a schematic plot of the experimental set-up. The piston type wave generator was programmed to generate a solitary wave with a wave height of

0.22 m in the water depth of 0.3 m. The solitary wave was reported to break as a spilling breaker, with a small curl-up of the wave crest.

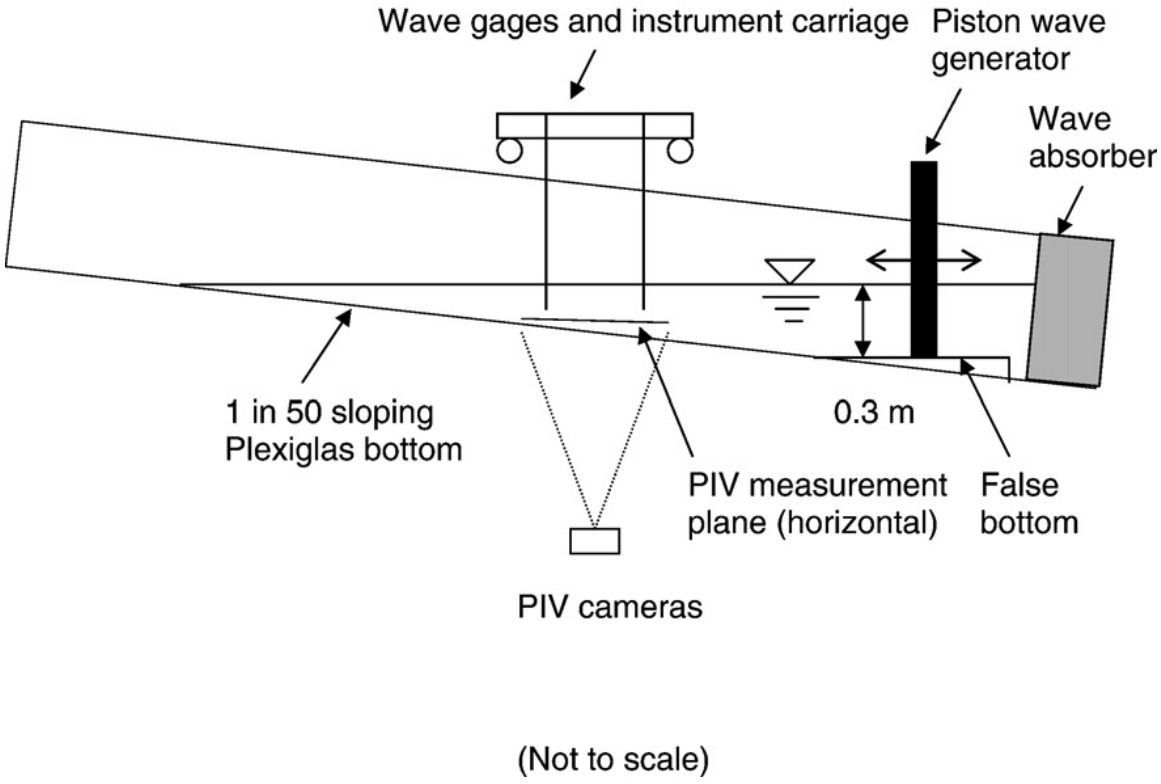

Figure 5.1: Schematic plot of experimental set-up (Ting, 2006)

Numerical simulation is performed using the GPUSPH model. The initial particle spacing of particles is 0.007 m and about seven million particles are used in the simulation. A moving boundary in the model represents a piston wave generator. The Goring and Raichlen (1980) approach is used to generate the waves. The basic concept is to match the velocity of the wave generator to the corresponding velocity of the water particles (depth-averaged velocity). At the surface of the wave generator:

$$\frac{d\zeta}{dt} = \bar{U}(\zeta, t) \tag{5.1}$$

where ζ is the wave generator displacement and $\bar{U}(\zeta, t)$ is the depth-averaged velocity.

From continuity considerations, the depth-averaged velocity can be defined as:

$$\bar{U}(\zeta, t) = \frac{c\eta(\zeta, t)}{h + \eta(\zeta, t)} \tag{5.2}$$

where h is the water depth, η is the free surface displacement, and c is the wave velocity. Therefore:

$$\frac{d\zeta}{dt} = \frac{c\eta(\zeta, t)}{h + \eta(\zeta, t)} \tag{5.3}$$

The free surface displacement can be considered as :

$$\eta(\zeta, t) = H[f(\theta)] \tag{5.4}$$

where H is the wave height and:

$$\theta = k(ct - \zeta) \tag{5.5}$$

In this equation k is the wave number. From equation 5.3, 5.4, and 5.5, Goring and Raichlen (1980) show:

$$\frac{d\zeta}{d\theta} = \frac{H[f(\theta)]}{kh} \tag{5.6}$$

and:

$$\zeta(t) = \frac{H}{kh} \int_0^\theta f(w) dw \tag{5.7}$$

For a solitary wave, wave function $f(\theta)$ is defined as:

$$f(\theta) = \operatorname{sech}^2 \theta \tag{5.8}$$

and the wave number and wave velocity are:

$$k = \sqrt{\frac{3H}{4h^3}} \tag{5.9}$$

$$c = \sqrt{g(H+h)} \tag{5.10}$$

From equation 5.7 and 5.8, $\zeta(t)$ in a solitary wave can be defined as:

$$\zeta(t) = \frac{H}{kh}\tanh k(ct - \zeta) \tag{5.11}$$

For practical purposes, time t_0 is defined as:

$$t_0 = \frac{\tanh^{-1}(0.999)}{kc} = \frac{3.8}{kc} \tag{5.12}$$

The stroke S is obtained by evaluating equation 5.11 at time equal to $+\infty$ and $-\infty$ and subtracting the values from each other.

$$S = \frac{2H}{kh} = \sqrt{\frac{16}{3}\frac{H}{h}}h \tag{5.13}$$

The duration of wave generator motion τ is then computed as:

$$\tau = 2t_0 + \frac{S}{c} = \frac{2}{kc}(3.8 + \frac{H}{h}) \tag{5.14}$$

Substituting equation 5.12, 5.13, and 5.14 in equation 5.11, a generation equation for solitary wave is defined as:

$$\frac{\zeta(t)}{S} = \frac{1}{2}\{1 + \tanh 2[(3.8 + \frac{H}{h})(\frac{t}{\tau} - \frac{1}{2}) - \frac{H}{h}(\frac{\zeta}{S} - \frac{1}{2})]\} \tag{5.15}$$

The solitary wave generation trajectory in our problem is computed using equation 5.15 and presented in the figure 5.2. In our case the wave height is equal to 0.22 m and the water depth is equal to 0.3 m.

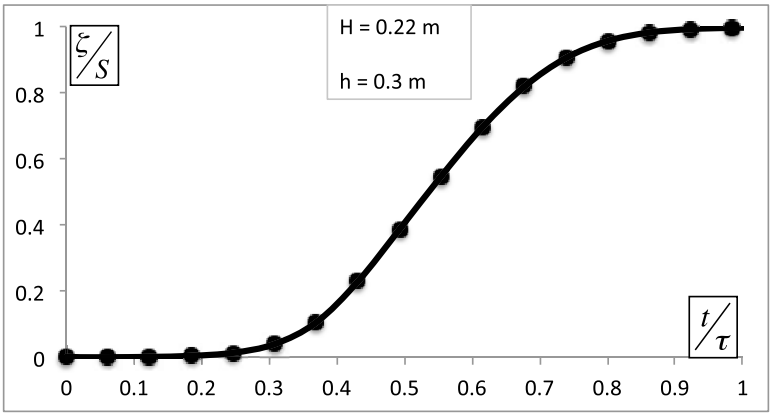

Figure 5.2: Solitary wave piston trajectory

Wave height variations along the flume were measured at 12 stations between the wave generator and the still water shoreline. The distance between adjacent stations was 1 m. Figure 5.3 illustrates the ensemble-averaged water surface profile in both experimental measurements and numerical simulation. In Ting (2006) experimental study, wave measurements were repeated at least five times and were averaged to provide an ensemble-averaged water surface. In the numerical simulation, ensemble averaging is performed over the width of the tank. The numerical resolution used in the ensemble-averaging is considered to be equal to the initial particle spacing.

The instantaneous velocity is decomposed to ensemble averaged velocity and the turbulent velocity as:

$$\vec{u} = < \vec{u} > + \vec{u}' \tag{5.16}$$

Figure 5.4 illustrates a comparison of the numerical results and experimental results of ensemble-averaged horizontal velocity under the solitary wave. The experimental results were measured by both PIV and ADV instruments. The ADV mea-

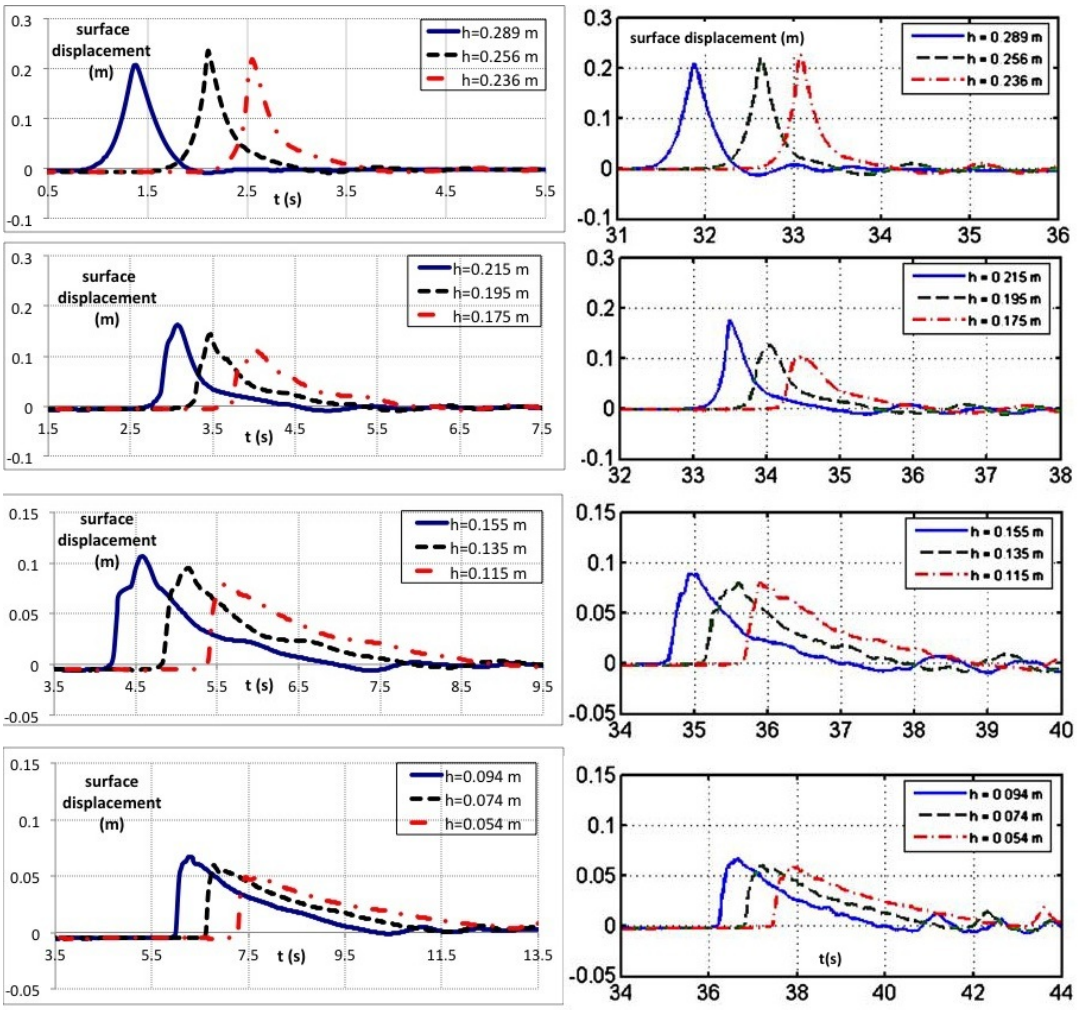

Figure 5.3: Ensembled-averaged wave elevations (Left: Numerical results, Right: Experimental results) - note: The time = 0.5 s of numerical results is equivalent to time = 31 s of experimental results

surements were averaged over 29 test runs. The PIV measurements were averaged over 27 test runs. In the numerical computations, ensemble averaging was performed over the 90 planes over the width of the tank. In this figure the numerical time = 3.5 s is equal to the experimental time = 34 s.

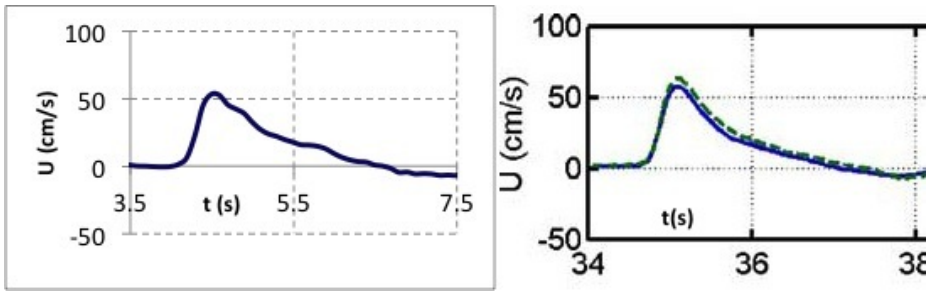

Figure 5.4: Four seconds of ensembled-averaged horizontal velocity under the solitary wave (Left: Numerical result; Right: Experimental result) - note: The dash line in the experimental results corresponds to the ADV measurements and the solid line corresponds to the PIV measurements. The time = 3.5 s of numerical results is equivalent to time = 34 s of experimental results

Instantaneous turbulence velocity components (u', v', w'), corresponding turbulent kinetic energy ($k = (u'^2 + v'^2 + w'^2)/2$), and turbulence stresses (u'^2, v'^2, w'^2, $u'v'$, $u'w'$,$v'w'$) were measured in the experimental results of Ting (2006). The experimental velocity measurements were obtained at the location of $\frac{h}{h_b} = 0.646$ where h is the water depth and the the water depth where the maximum wave height occurs is $h_b = 0.236m$. In our study the numerical results of these parameters have been computed. Figure 5.5 presents the numerical and experimental results at a height of 70 mm above the flume bed. A large event can be observed at t=35.7s of experimental time which is equal to t=5.2 s of numerical time.

Figure 5.6 illustrates the coherent structures detected by λ_2 criterion at t=5.5 s of the numerical simulation. The λ_2 criterion detects the cores of the vortex structures

and was first proposed by Jeong and Hussain (1994). In this method, the tensor $S^2 + \Omega^2$ is considered where S and Ω are the symmetric and antisymmetric components of velocity gradient tensor $\nabla\vec{u}$. The term λ_2 is obtained as the second largest eigenvalue of this tensor and a vortex core is defined as a region with a negative λ_2 threshold. The size of the coherent structures varies using different λ_2 thresholds but the core geometry of the coherent structure is not sensitive to λ_2. A reversed horseshoe vortex structure can be observed at the position of the measurement location. The process of the generation and propagation of the reversed horseshoe coherent structures will be discussed in the following sections.

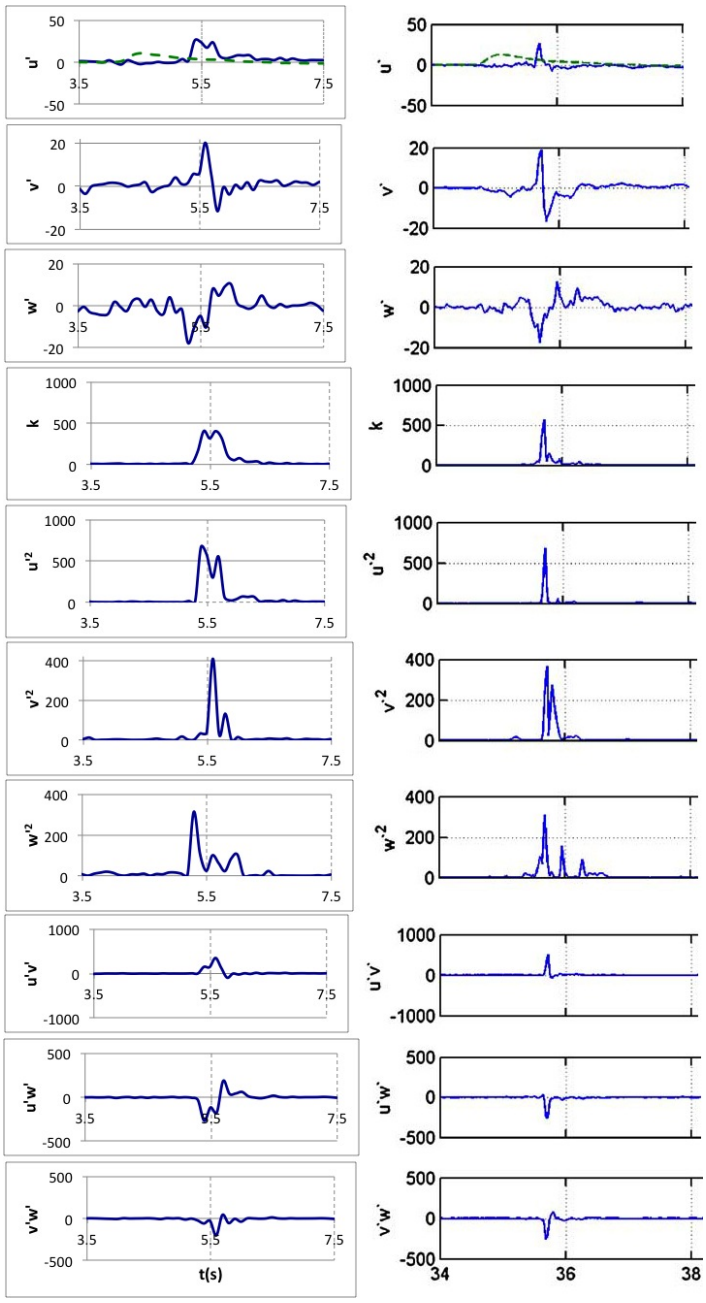

Figure 5.5: Instantaneous turbulence velocities ($\frac{cm}{s}$), turbulent energy($\frac{cm^2}{s^2}$) and turbulent stresses ($\frac{cm^2}{s^2}$) measured at a height of 70 mm above the tank bed. Left: Numerical results, Right: Experimental results. The dashed line in the uppermost plot is $0.2 < u >$

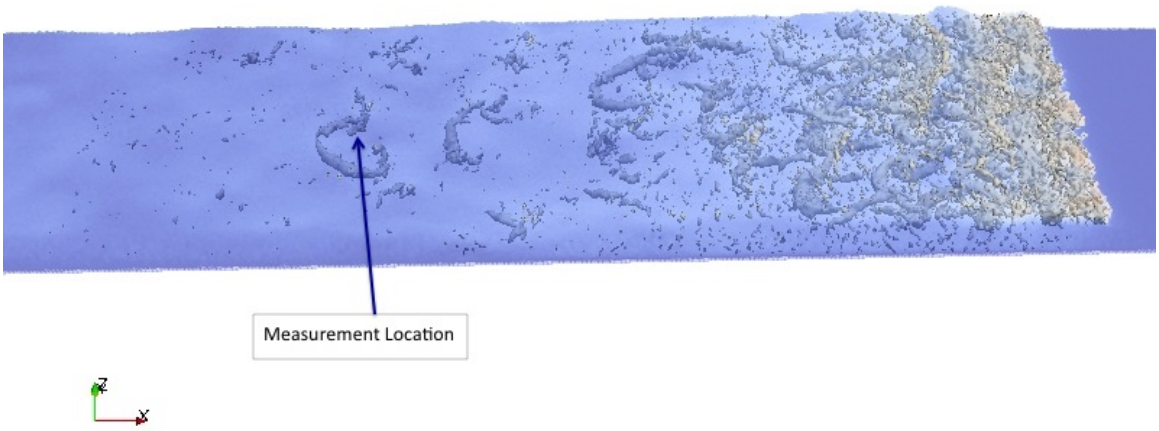

Figure 5.6: Vortex structures identified by the isosurface of $\lambda_2 = -25$ at numerical time=5.5 s

5.3 Generation and evolution of 3D coherent structures behind the breaker

5.3.1 Evolution of reversed horseshoe (hairpin) vortex structures

In the past few decades of study on turbulence, various definitions and detection methods have been proposed for the coherent structures. Hussain (1986) defined a coherent structure as "A connected turbulent fluid mass with instantaneously phase-correlated vorticity over its spatial extent". This concept indicates that in a turbulent field with random, three-dimensional vorticity, organized coherent structures can be detected, which include coherent large-scale vorticity component over the spatial extent of the structures. However, a coherent structure can evolve and the structure size can change by pairing, tearing, cross linking and entrainment. Coherent structures can have various physical configurations such as roller, rib, hairpin, toroidal, helical, bihelical, etc. These structures play an important role in the transport of mass, momentum, and heat and hence a number of various coherent detection schemes have been developed to capture them. In this study, we used λ_2, which is one of the most popular schemes to detect the vortex cores. The solitary wave in our simulation breaks as a spilling breaker. When the wave breaks water spills down the wave crest and hits the water surface ahead. Then it splashes up, overturns and hits the water

surface further ahead as presented in figure 5.7.

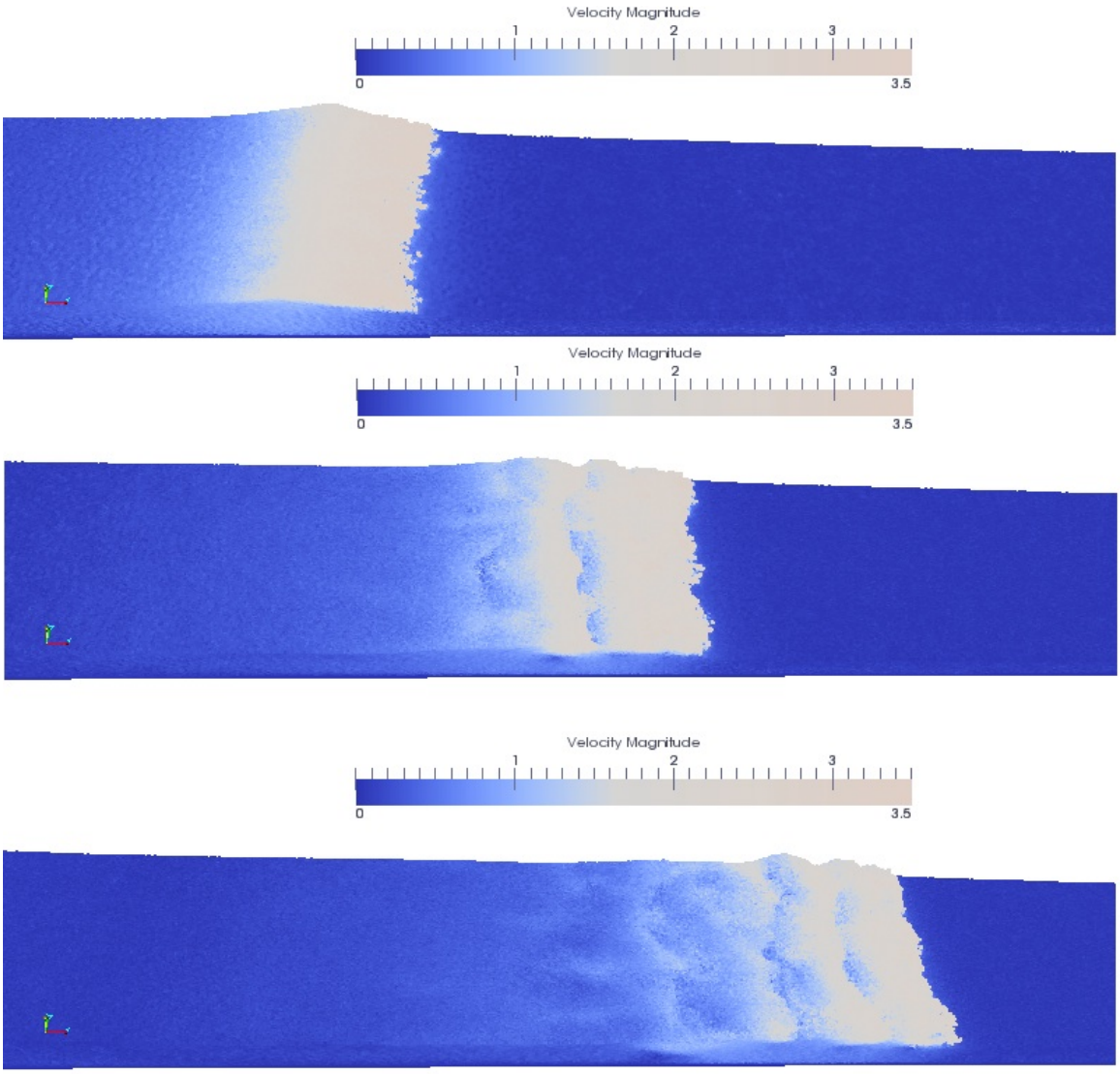

Figure 5.7: Numerical results of solitary wave breaking as a spilling breaker at time = 3, 3.5, 4s

CHAPTER 5. THREE-DIMENSIONAL HORSESHOE VORTEX STRUCTURES UNDER A BROKEN SOLITARY WAVE

When the wave front hits the water surface, spanwise vortex structures are developed at the wave toe. In addition, some vertical vortex structures are also developed at the tow of the broken wave that are known as downbursts. After a short period of time, reversed horseshoe structures begin to develop and travel downward towards the bed bottom.The development of the coherent reversed horseshoe (hairpin) vortex structure initiates from the portions of the spanwise roller where the curvature is relatively high. As the reversed horseshoe(hairpin) develops, larger portion of vortex is converted from spanwise component to vertical and streamwise components. Two legs of the reversed horseshoe structures have counter-rotating vorticities that were previously observed as obliquely descending eddies and were assumed to be two separate vortex structures (Nadaoka et al., 1989). In addition to reversed horseshoe vortices, there exist quasi-streamwise vortices that are primarily in streamwise direction. Figure 5.8 illustrates the time history of the generation and evolution of reversed horseshoe structures. The vortex structures are detected by the isosurface of $\lambda_2 = -50$.

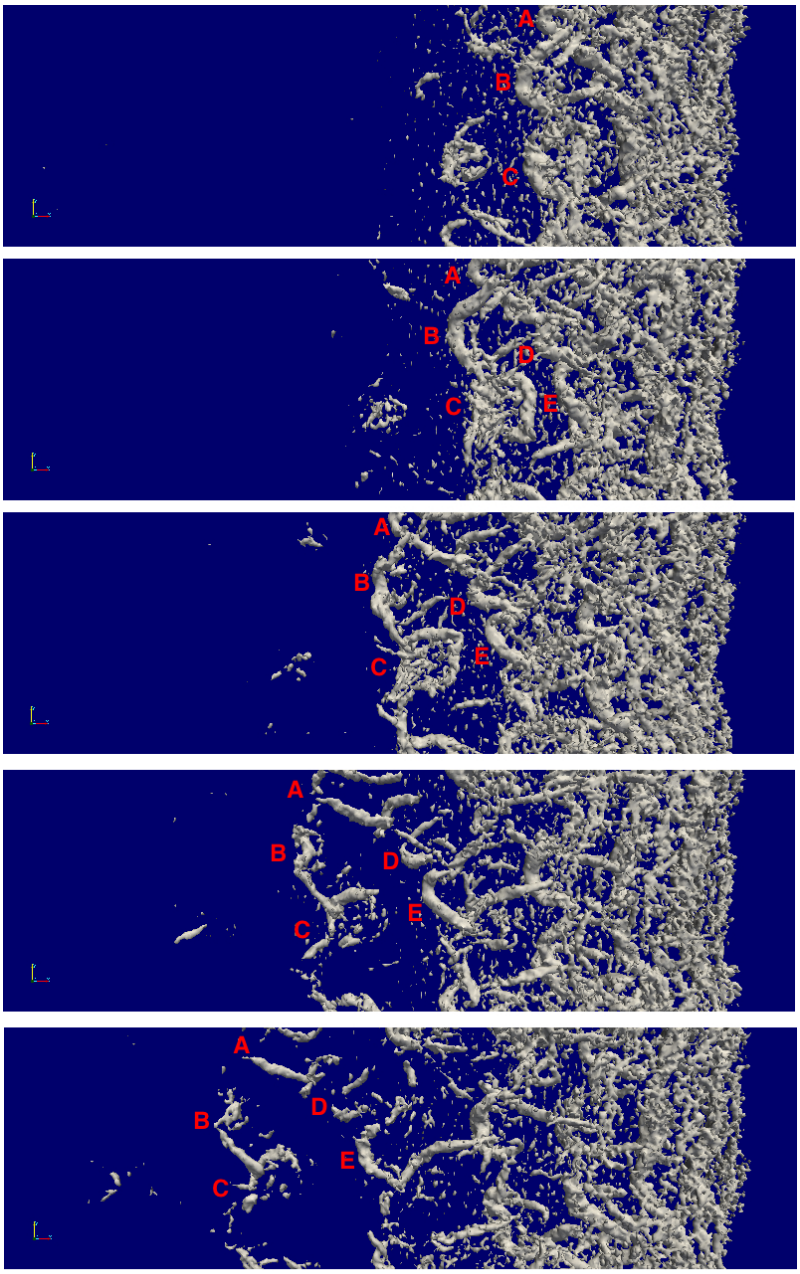

Figure 5.8: Vortex evolution after the broken wave at time = 3.5, 3.7, 3.9, 4.1, 4.3, 4.5, 4.7, 4.9, 5.1, 5.3, 5.5s. The flow field is observed from above in a wave-following frame of reference.The vortex structures are detected by the isosurface of $\lambda_2 = -50$.

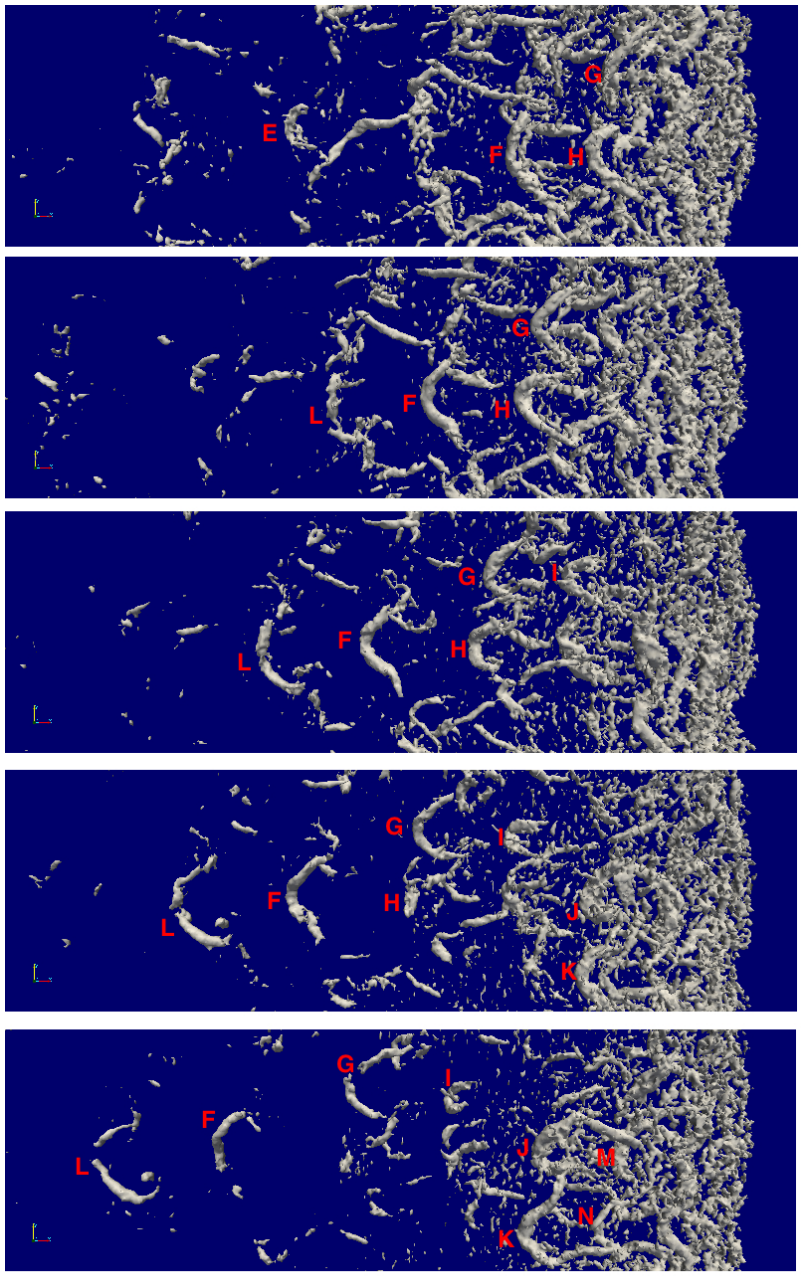

Figure 5.8: (Continued)Vortex evolution after the broken wave at time = 3.5, 3.7, 3.9, 4.1, 4.3, 4.5, 4.7, 4.9, 5.1, 5.3, 5.5s. The flow field is observed from above in a wave-following frame of reference.The vortex structures are detected by the isosurface of $\lambda_2 = -50$.

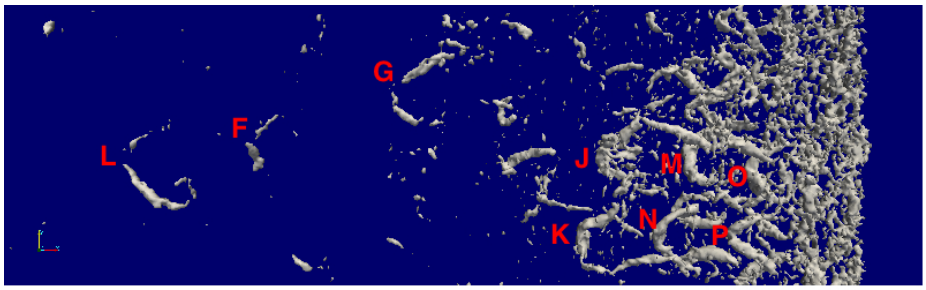

Figure 5.8: (Continued)Vortex evolution after the broken wave at time = 3.5, 3.7, 3.9, 4.1, 4.3, 4.5, 4.7, 4.9, 5.1, 5.3, 5.5s. The flow field is observed from above in a wave-following frame of reference.The vortex structures are detected by the isosurface of $\lambda_2 = -50$.

Reversed horseshoe structures start to be generated from the horizontal spanwise rollers at time = 3.5 s, when the solitary wave is already broken, splashed up, and overturned (Figure 5.7). As the broken wave propagates and continue the cycle of overturning and splashing up cycle, the reversed horseshoe structures are initiated from the locations of the spanwise rollers that have higher curvature. The horseshoe structures continue to evolve and get separated from the spanwise rollers, and hence the spanwise vorticity is turned into streamwise and vertical vorticities. Two or three reversed horseshoe structures are generated from each horizontal spanwise roller. At time = 3.5 s, three reversed horseshoe structures (A, B, C) are initiated from the first horizontal roller. At time = 3.7 s, another two reversed horseshoe structures (D, E) are generated from the second horizontal roller. As time passes by, these structures evolve and propagate in -x-direction (from right to left) in the wave-following frame

of reference. Some of the reversed horseshoe structures undergo tearing or pairing (vortex structure A, tears up at time = 4.1 s). New horseshoe structures are generated at time = 4.5 s (F, G, H), time = 4.9 s (I, L), time = 5.1 (J,K), time = 5.3 s (M,N), and time = 5.5 s (O,P).

To understand the generation and evolution of the reversed horseshoe structures, we consider a frame traveling at the wave speed in the +x-direction (from left to right). In the wave-following frame, the fluid particles under the wave surface travel in the -x-direction (from right to left) as is shown in figure 5.9.

The development of the characteristic reversed horseshoe structures behind the broken waves is analogous to the development of horseshoe structures in the wall-bounded shear flows (Green, 1995), except that the velocity profile is reversed. In the wave-following frame, the horizontal velocity profile under the wave surface is in the -x-direction and the horizontal velocities increases as the distance from the wave surface increases. Therefore, the direction of the horseshoe configuration and the direction of the horseshoe legs rotations are reversed in comparison to the wall-bounded shear flows. Similar to the horseshoe structures in the wall-bounded shear flows, the reversed horseshoe structures are initiated from the portions of the spanwise vortex where the curvature of the vortex is relatively high. As the reversed horseshoe develops, larger portions of the vortex are turned and converted from spanwise to streamwise and vertical vorticities.

5.3.2 Reynolds shear stresses and the turbulent momentum flux

Reynolds shear stresses can be categorized by the quadrant analysis (Willmarth and Lu 1972; Wallace et al. 1972; Alfredsson and Johansson 1984). The second ($u' < 0, w' > 0$) and the fourth ($u' > 0, w' < 0$) quadrants are of particular interest since they have a positive contribution to the turbulent energy production. The second quadrant (QD-2) is known as sweep and the fourth quadrant (QD-4) is known as ejection. Figure 5.10 presents the vortex structures behind the broken wave at time = 4.7 s.

One of the reversed horseshoe structures (vortex H in figure 5.8) is selected and turbulent velocities (v', $'w'$), streamwise vorticity (ω_x), turbulent momentum flux ($-u'w'$), and kinetic turbulent energy ($k = (u'^2 + v'^2 + w'^2)/2$) are computed. The streamwise vorticity profile and the turbulent velocities indicate that the reversed horseshoe vortex structure is associated with the downwelling motion (sweep). Large amount of turbulent momentum flux and turbulent kinetic energy are generated at the middle of the two counter-rotating legs and at the outer corner of the legs. The results are consistent with Kim and Moin (1986) and Yang and Shen(2009) results. Variation of turbulent velocities (v', $'w'$) and the turbulent momentum flux ($-u'w'$) over time for the reversed horseshoe structure H is presented in figure 5.11. As the time passes, the reversed horseshoe travels downward to the deeper layers of the water column

and spreads the turbulence toward the bottom. As the horseshoe travels downward, the intensity of the turbulent momentum flux decreases due to the spreading and dissipation.

Conditional averaging is performed on the reversed horseshoe structures of the same age. Figure 5.12 presents the conditionally averaged turbulent velocities (v', w') and the turbulent momentum flux ($-u'w'$), which were computed by applying conditional averaging on vortex structure G and H at time = 4.7 s (figure 5.8). For conditional averaging, vertical planes are passed over vortex structure G and H with the same relative distance from the end of the vortex structures and the turbulent velocities (v', w') and the turbulent momentum flux ($-u'w'$) are calculated on these planes and then are being averaged. The same sweep event is detected in the conditional-averaged profiles.

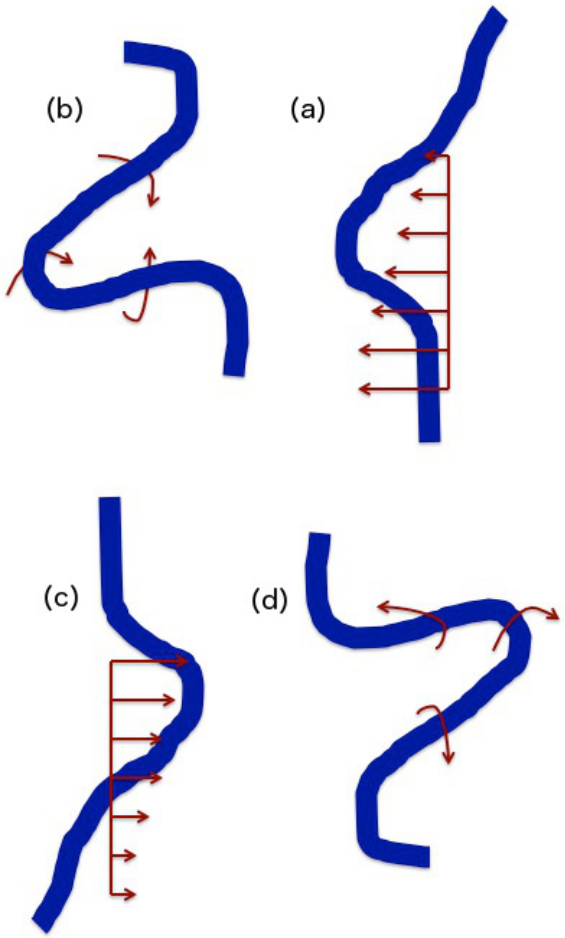

Figure 5.9: Schematic illustration of a horseshoe (hairpin) vortex evolution in a turbulent flow. Top: Wave breaking problem in a wave-following frame of reference (reversed horseshoe structure), Bottom: Boundary layer problem (horseshoe structure) (a): vertical velocity profile in a wave-following frame of reference of a wave breaking problem and the generation of a reversed horseshoe structure (b): a reversed horseshoe structure in a wave breaking problem (c): vertical velocity profile in a boundary layer problem and the generation of a horseshoe structure (d): a horseshoe structure in a boundary layer problem

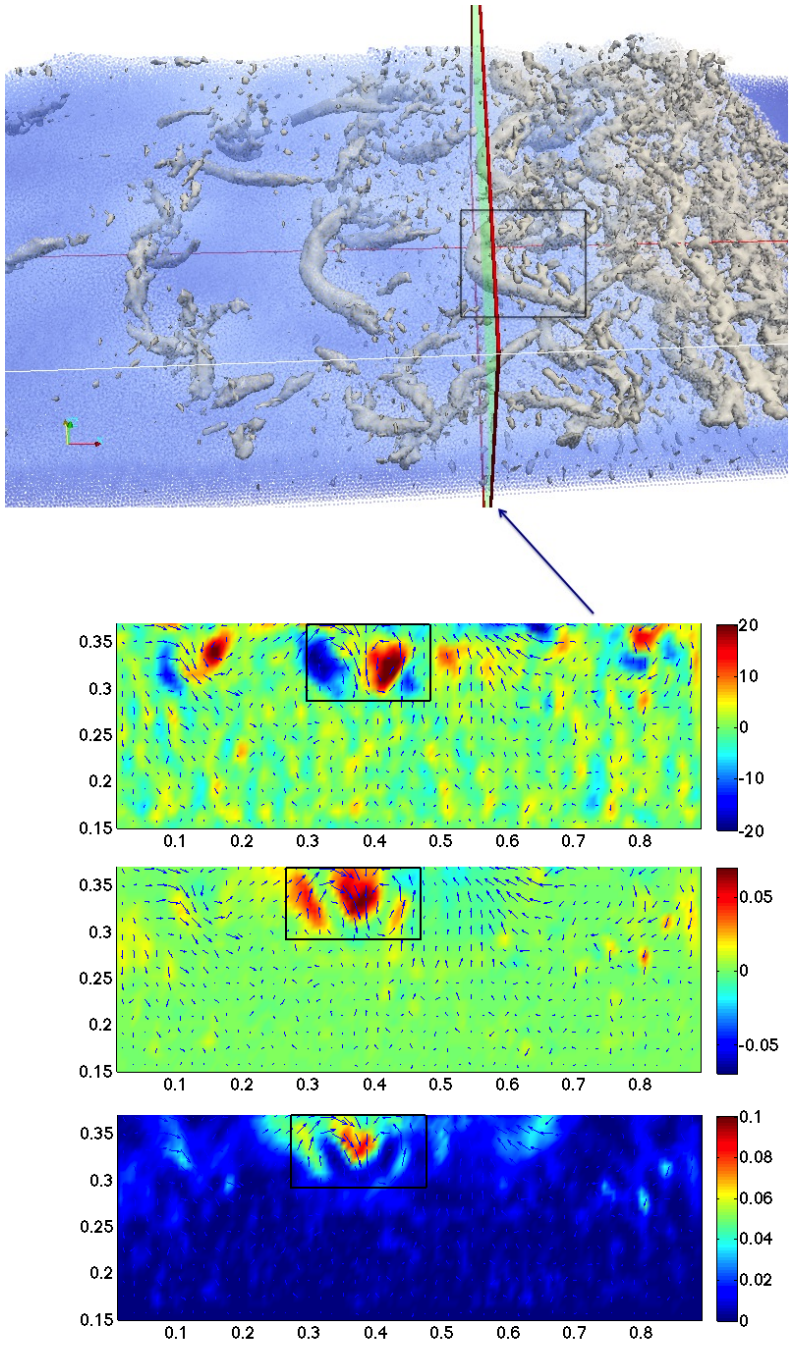

Figure 5.10: Reversed horseshoe structures at time = 4.7 s. From top to bottom: (a) Streamwise vorticity profile (ω_x) and turbulent velocity vectors (v', w'), (b) turbulent momentum flux ($-u'w'$), (c) Turbulent kinetic energy

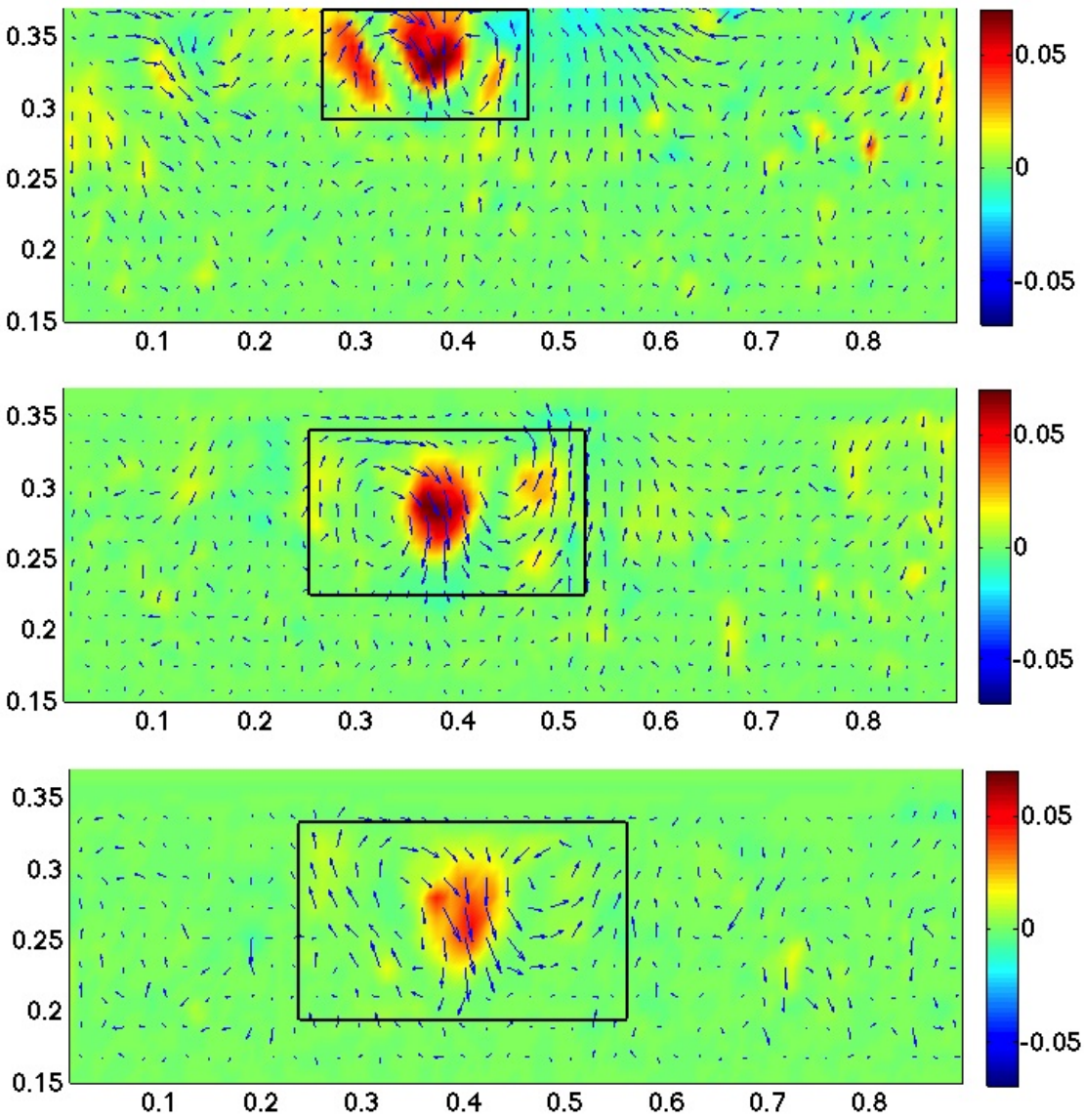

Figure 5.11: Turbulent momentum flux ($-u'w'$) and turbulent velocity vectors (v', w') at time = 4.7, 5.1, 5.5 s

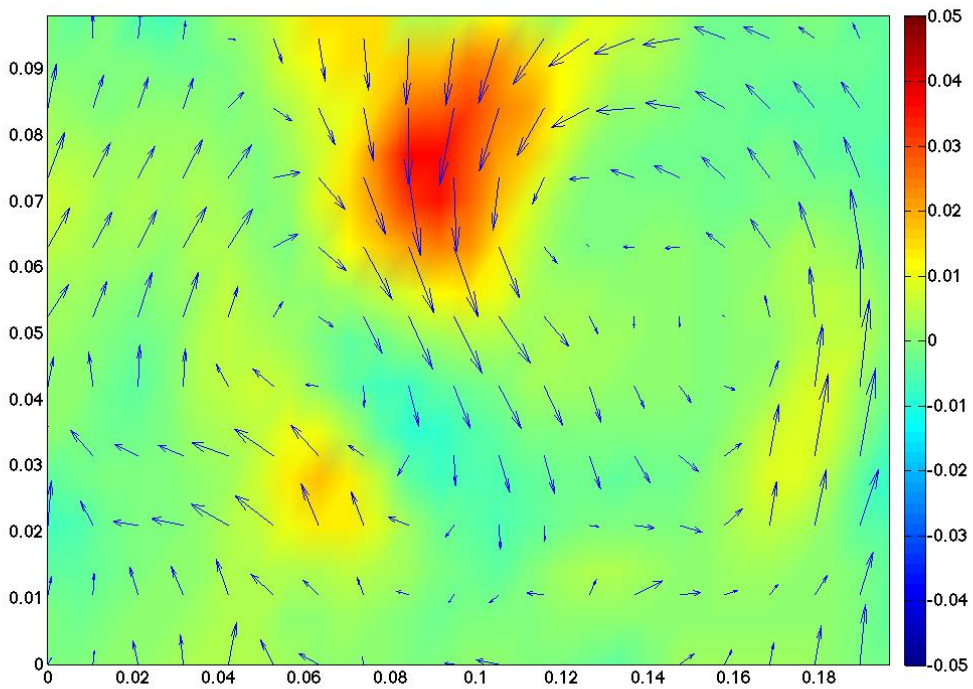

Figure 5.12: Conditionally averaged turbulent momentum flux ($-u'w'$) and turbulent velocity vectors (v', w') at time = 4.7 (Conditional averaging has been applied to vortex structure G and H of figure 5.8)

5.4 Evolution of the vortex structures and the vortex stretching

In the previous section the generation and evolution of the horseshoe structures at the back of the broken solitary wave were illustrated using the instantaneous snapshots of λ_2 criterion. In this section, the cause for the formation of these vortical structures will be discussed by studying the vorticity equation and the vortex stretching and turning. The vorticity equation is obtained by taking the curl of the momentum equation. Obliquely horseshoe structures contain both vertical and spanwise vorticities. For a flow of constant density, negligible viscosity, and with only potential body forces, the spanwise and vertical components of the vorticity equation are written as:

$$\frac{D\omega_x}{Dt} = \underbrace{\omega_x \frac{\partial u}{\partial x}}_{\text{Term one}} + \underbrace{\omega_y \frac{\partial u}{\partial y}}_{\text{Term two}} + \underbrace{\omega_z \frac{\partial u}{\partial z}}_{\text{Term three}} \tag{5.17}$$

$$\frac{D\omega_z}{Dt} = \underbrace{\omega_x \frac{\partial w}{\partial x}}_{\text{Term one}} + \underbrace{\omega_y \frac{\partial w}{\partial y}}_{\text{Term two}} + \underbrace{\omega_z \frac{\partial w}{\partial z}}_{\text{Term three}} \tag{5.18}$$

where ω_x, ω_y, and ω_z are the vorticity in x, y, and z directions. Term one of equation 5.17 is associated to the vortex stretching of streamwise vorticity ω_x. Term two and three of equation 5.17 are associated to vortex turning from spanwise vorticity ω_y and vertical vorticity ω_z to streamwise vorticity ω_x. Similarly, term one and two of equation 5.18 correspond to vortex turning and term three corresponds to the vortex stretching.

CHAPTER 5. THREE-DIMENSIONAL HORSESHOE VORTEX STRUCTURES UNDER A BROKEN SOLITARY WAVE

In a spilling breaker, water spills over the wave crest towards the water surface ahead. Streamwise perturbations of the original surface grow rapidly as the water stretches forward and irregularities occur at the forward-moving water surface. The disintegration of a plunging breaker jet was studied in theory by Longuet-Higgins, 1995 and in an experimental study by Perlin and He, 1996. In our study, the solitary wave breaks as a spilling breaker. The spilling water hits the water surface ahead, splashes up, jump forward, and hits the water surface further ahead (figure 5.7). The irregularities at the head of the broken wave, cause a gradient of the vertical velocity over the width of the tank ($\frac{\partial w}{\partial y}$). Figure 5.13 illustrates the variation of vertical velocity over the width of the tank, on a plane that is parallel to the x-y plane, at the position of $z = 0.42m$, and at time = 4 s.

When the spilling wave breaks, spanwise vorticity (ω_y) has a nonzero value. Therefore term two of equation 5.18 ($\omega_y \frac{\partial w}{\partial y}$) will have a nonzero value at the locations where $\frac{\partial w}{\partial y}$ has value and consequently positive and negative components of vertical vorticity (ω_z) will be produced at those locations (left hand side of equation 5.18). In other words, spanwise vorticity produces vertical vorticity at the positions of nonzero $\frac{\partial w}{\partial y}$. The counter-rotating vertical vortex structures have been observed at the location where the broken wave hit the water surface ahead and have been named as downbursts (Ting 2006, 2008). When vertical vorticity is produced, term three of equation 5.17 ($\omega_z \frac{\partial u}{\partial z}$) will have a nonzero value at the locations where $\frac{\partial u}{\partial z}$ has value. Figure 5.14 presents the velocity vectors and velocity magnitude under the broken wave.

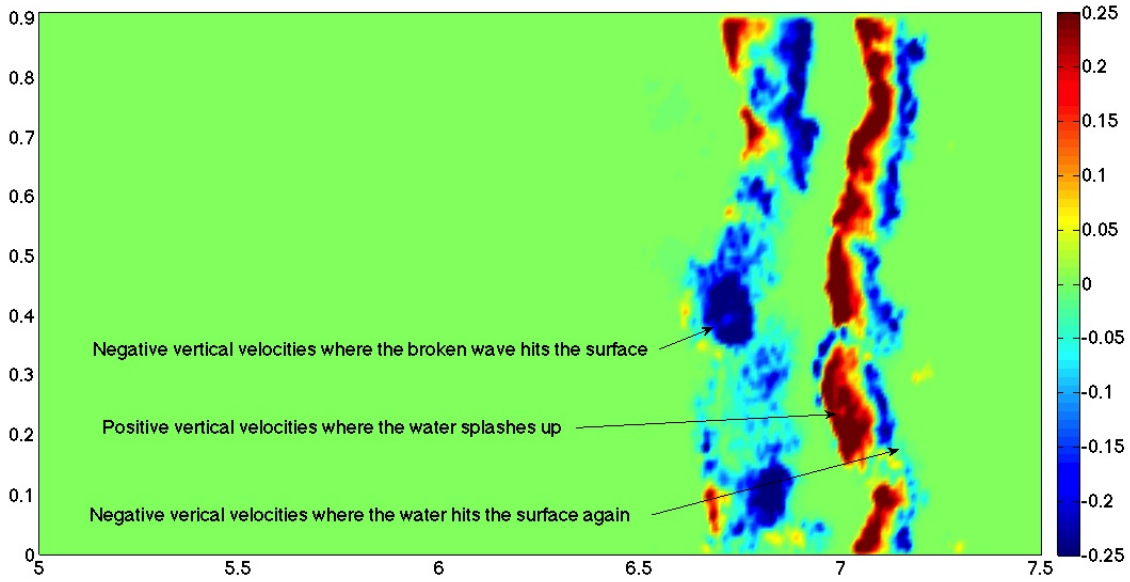

Figure 5.13: Vertical velocity on a plane that is parallel to the x-y plane, at the position of $z = 0.42m$, and at time = 4 s, showing the variation of vertical velocity over the width of the tank

Vertical gradient of streamwise velocity ($\frac{\partial u}{\partial z}$) has nonzero value beneath the broken wave. Term two of equation 5.17 ($\omega_y \frac{\partial u}{\partial y}$) will have a nonzero value at the locations where $\frac{\partial u}{\partial y}$ has value. Figure 5.15 illustrates the variation of streamwise velocity over the width of the tank, on a plane that is parallel to the x-y plane, at the position of $z = 0.42m$, and at time = 4 s. The variation in the streamwise velocity over the width of the tank is due to the irregularities at the head of the broken wave that was discussed previously. In equation 5.17 , both term two and three have nonzero values and contribute in the generation of spanwise vorticity ω_x (left hand side of equation 5.17).

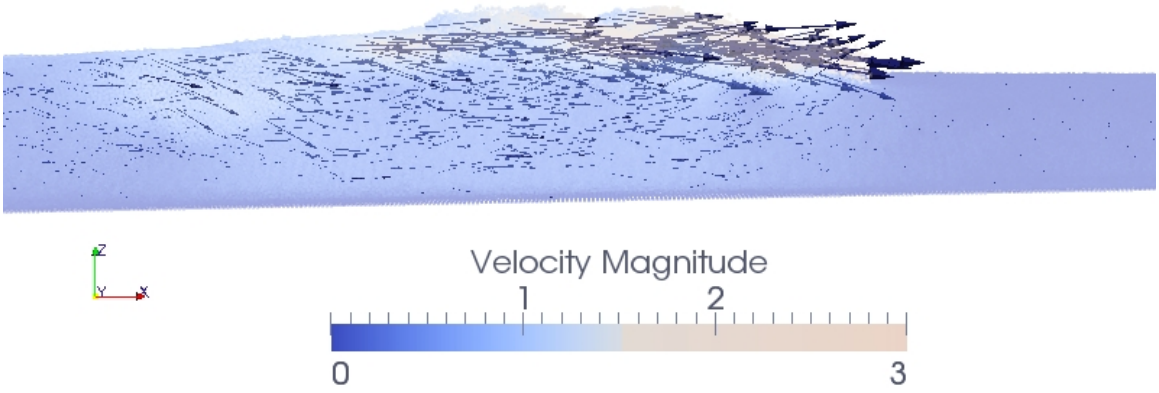

Figure 5.14: Velocity vectors and velocity magnitude under the broken wave

The vorticity equation terms have been calculated separately to study the importance of each term. Figure 5.16 presents the different terms of equation 5.17 and 5.18. Terms two and three of equation 5.17 ($\omega_y \frac{\partial u}{\partial y}$, $\omega_z \frac{\partial u}{\partial z}$) are the largest and are associated to vortex turning from spanwise vorticity to streamwise vorticity and vertical vorticity to streamwise vorticity respectively. Term one and two of equation 5.18 ($\omega_x \frac{\partial w}{\partial x}$, $\omega_y \frac{\partial w}{\partial y}$) also have large values, which are associated to vortex turning from streamwise vorticity to vertical vorticity and spanwise vorticity to vertical vorticity respectively. Term one of equation 5.17 and term three of 5.18 ($\omega_x \frac{\partial u}{\partial x}$ and $\omega_z \frac{\partial w}{\partial z}$), which are associated to vortex stretching in x and z directions, have smaller values.

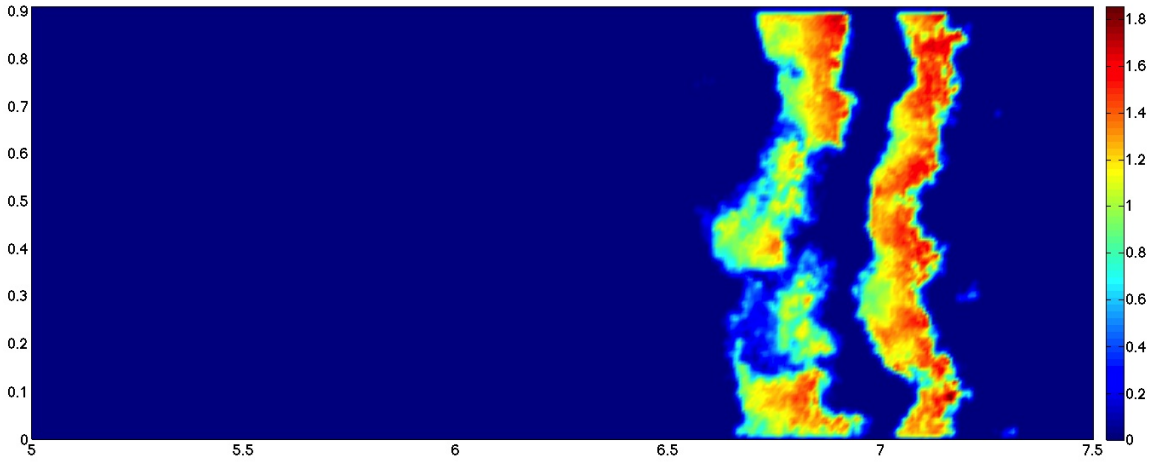

Figure 5.15: Streamwise velocity on a plane that is parallel to the x-y plane, at the position of $z = 0.42m$, and at time = 4 s, showing the variation of streamwise velocity over the width of the tank

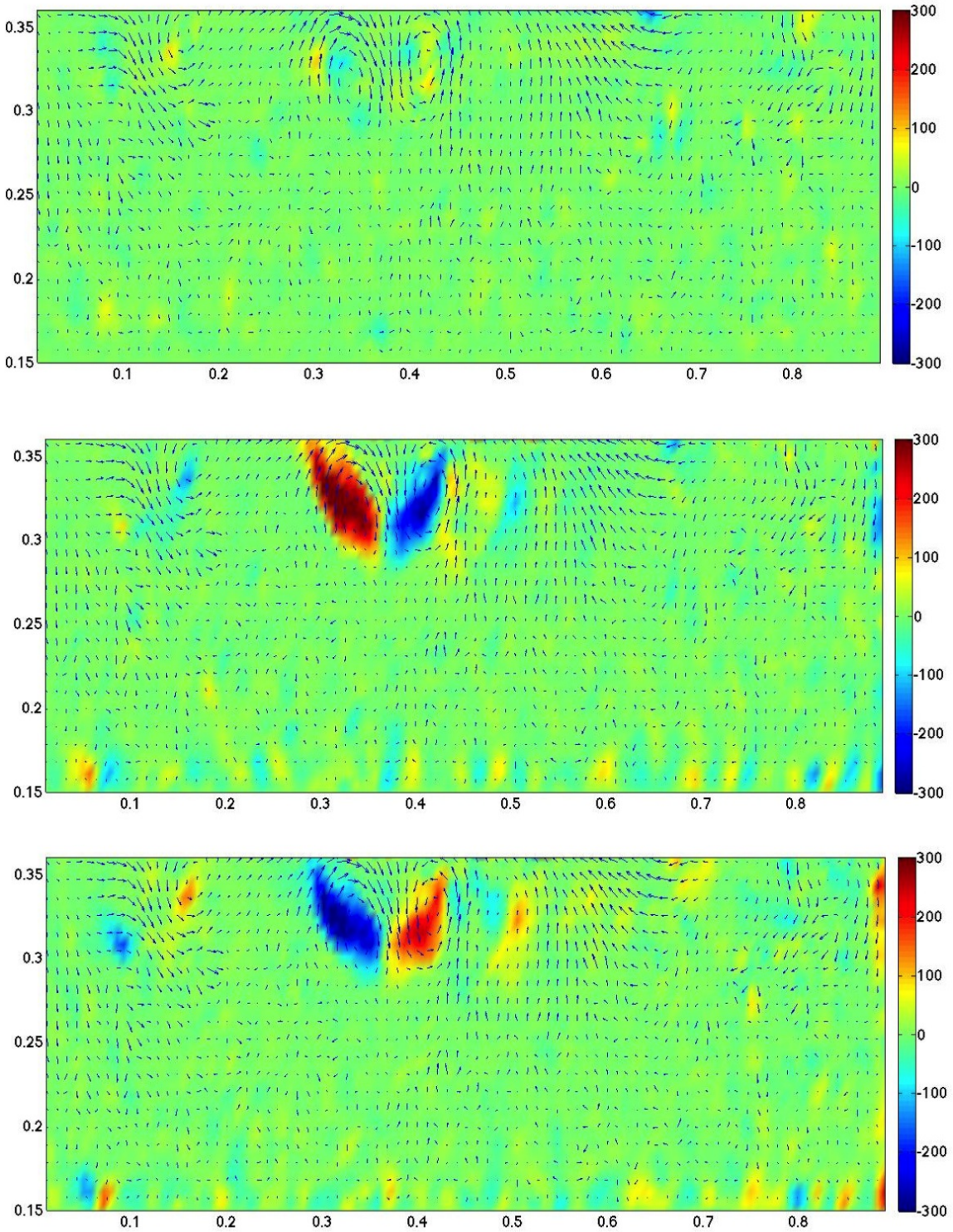

Figure 5.16: Vorticity equation terms. From top to bottom: $\omega_x \frac{\partial u}{\partial x}$, $\omega_y \frac{\partial u}{\partial y}$, $\omega_z \frac{\partial u}{\partial z}$, $\omega_x \frac{\partial w}{\partial x}$, $\omega_y \frac{\partial w}{\partial y}$, $\omega_z \frac{\partial w}{\partial z}$

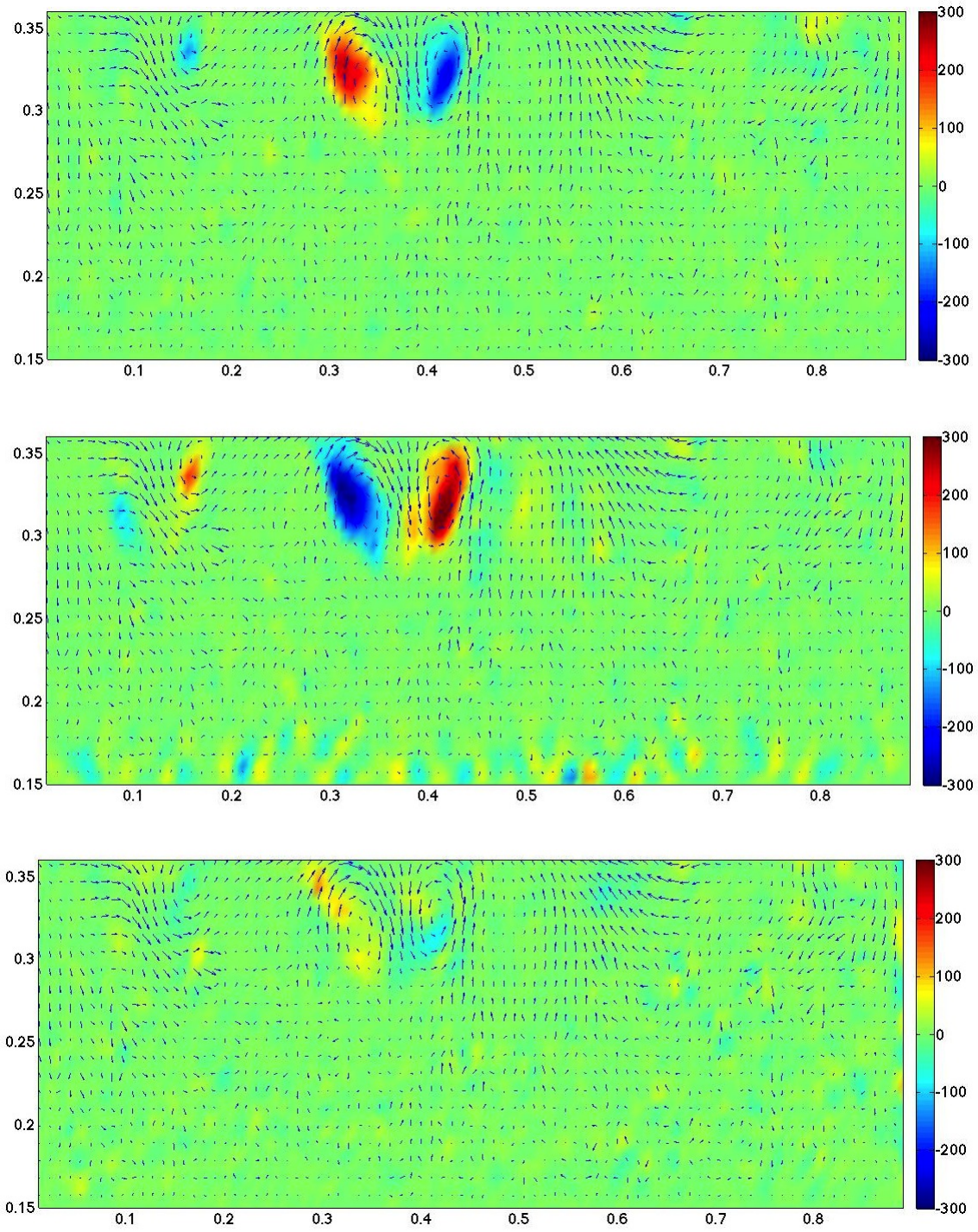

Figure 5.16: (Continued)Vorticity equation terms. From top to bottom: $\omega_x \frac{\partial u}{\partial x}$, $\omega_y \frac{\partial u}{\partial y}$, $\omega_z \frac{\partial u}{\partial z}$, $\omega_x \frac{\partial w}{\partial x}$, $\omega_y \frac{\partial w}{\partial y}$, $\omega_z \frac{\partial w}{\partial z}$

5.5 Vortex structures under a broken plunging solitary wave

In this section, a plunging solitary wave and the vortex structures under the broken wave will be studied. Different types of waves can be categorized as follows:

$$\zeta_0 = \frac{tan\beta}{\sqrt{\frac{H_0}{L_0}}} \tag{5.19}$$

where β is the beach slope, H_0 is the wave height, L_0 is the wave length, and ζ_0 is a criterion to show the breaker type. A wave is a spilling breaker if $\zeta_0 < 0.5$, a plunging breaker if $0.5 < \zeta_0 < 3.3$, and a surging beaker if $\zeta_0 > 3.3$. In the previous sections, in case of the spilling breaker ζ_0 was equal to 0.099. In the following section a plunging wave with ζ_0 equal to 0.55 will be numerically modeled.

In this section the same wave tank, which was introduced in the section 5.2, is used, only the beach slope is changed from 1 in 50 to 1 in 9. The wave height is equal to 0.22 m and the water depth close to the wave generator is equal to 0.3 m. Figure 5.17 illustrates the plunging solitary wave breaking at the beach and the corresponding run-up. The vortex structures are generated under the broken wave and are carried towards the shore by the run-up but no reversed horseshoe structure is observed at the back of the broken wave. The horizontal rollers that are generated under the broken wave hit the bottom by the plunging breaker and no reversed horseshoe structure is generated.

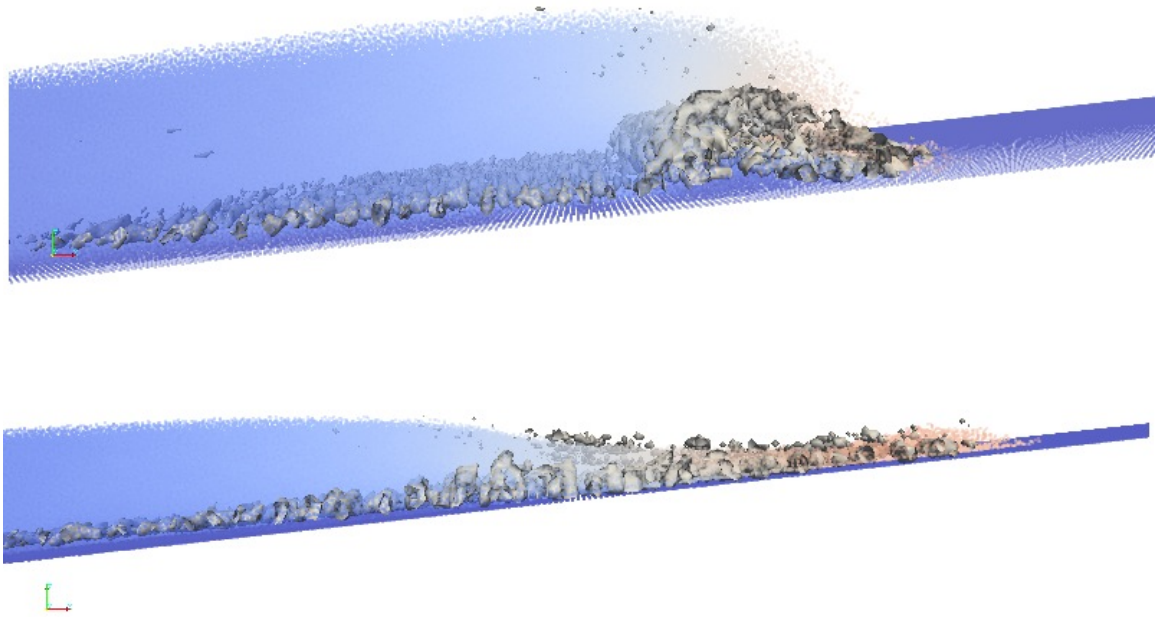

Figure 5.17: Plunging solitary wave breaking and vortex structures detected by the isosurfaces of $\lambda_2 = -50$. Top: time = 3.1 s, Bottom: time = 3.3 s

5.6 Conclusion

The SPH three-dimensional numerical model predicts the free surface evolution and wave height profiles well in comparison to the laboratory results. The model is also capable of detecting three-dimensional coherent structures under breaking waves including reversed horseshoe structures and the downward transportation of turbulent kinetic energy (TKE) and momentum flux. The obliquely descending eddies were found at the back of the broken waves in the previous studies but in this study, we showed that the observed obliquely descending eddies are the counter-rotating legs of the reversed horseshoe structures. The reversed horseshoe structures play a significant role on TKE and momentum transportation. The high levels of TKE and Reynolds stresses were captured at the regions between the two counter-rotating legs of the reversed horseshoe structures and the outer core of them. The reversed horseshoe structures tend to move downward into the water column and consequently transport momentum and TKE to the lower layer of the water column.

The physical mechanism of the generation and evolution of reversed horseshoe coherent structures were discussed by analyzing the vorticity equations and the vortex stretching and vortex turning terms. The spanwise vorticity (w_y) is stretched and generates vertical vorticity (w_z) at the locations with nonzero values of spanwise gradient of vertical velocity. Spanwise vorticity and vertical vorticity both contribute in the generation of streamwise vorticity (w_x).

Chapter 6

Three-dimensional vortex structures under periodic plunging waves

6.1 Introduction

In the previous chapter broken solitary waves both spilling and plunging, have been studied. In this chapter SPH numerical modeling of periodic plunging waves will be conducted and the vortex structures under the broken waves will be investigated. Periodic plunging waves play an important role in the equilibrium of beaches. When a plunging wave breaks, the front face of the wave becomes vertical and then jumps ahead as a plunging jet. The plunging jet overturns and hits the water surface ahead

with considerable force. Vortex structures under the broken plunging waves play a role in sediment transportation and beach erosion. In this chapter first the wave tank set-up of the numerical model is described. Then the vortex structures under the broken periodic waves and the water particle trajectories are studied. The water particle trajectories illustrate the rotation pattern in the vortex structures.

6.2 Wave tank set-up

A three-dimensional SPH numerical simulation has been performed to study the breaking periodic plunging waves. The wave tank is 5.5 m long, with a 1 m horizontal section and a 4.5 m slopping beach with a plane slope of 1 in 5.6 m. The width of the tank is equal to 2 m and the height is equal to 3 m. The periodic waves are generated by a flap wavemaker. The water depth close to the wavemaker is equal to 0.45 m. The wave period is 1 s. A floating ball is located at the water surface to track the surface variations during the wave generation, propagation, and breaking. Figure 6.1 illustrates a schematic plot of the wave tank.

Numerical simulation is performed using the GPUSPH model. The initial particle spacing of particles is equal to 0.01 m and about three and half million particles are used in the simulation. A moving boundary in the model represents a flap wavemaker and generates the periodic waves. Figure 6.2 illustrates a snapshot of the numerical results at time = 4.26 s (fifth wave period). This picture shows a wave that has been

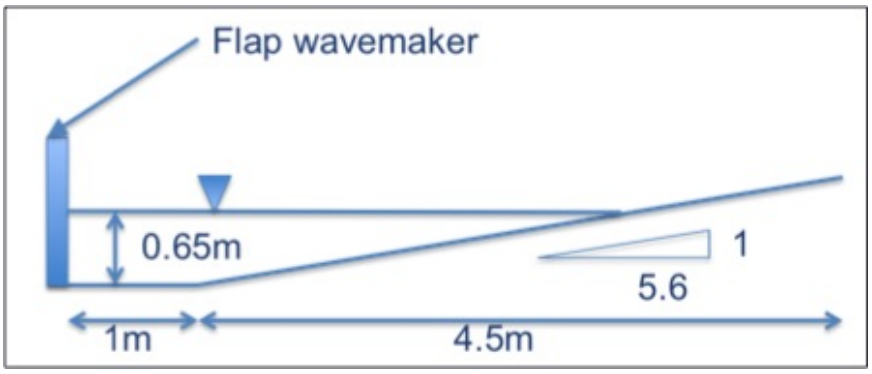

Figure 6.1: Schematic plot of the wave tank set-up

broken and hit the water surface ahead. Then the water splashed up and overturned further ahead as a rebounding jet.

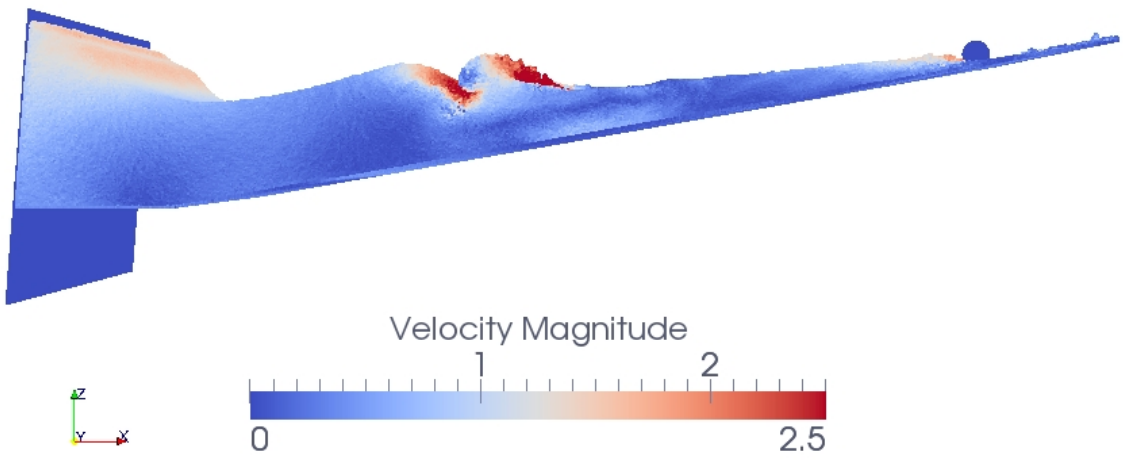

Figure 6.2: A snapshot of numerical results of periodic waves at time = 4.26 s (fifth wave period)

6.3 Vortex structures under broken periodic waves

The evolution and propagation of vortex structures under the broken periodic waves are investigated using λ_2 method. Figure 6.3 shows snapshots of the broken waves and the vortex structures detected by λ_2 method. As a plunging wave breaks and the plunging jet hits the water surface, a horizontal roller is generated beneath the toe of the broken wave. When the overturning jet hits the water surface, it splashes up, overturns, and another plunging jet is generated. The second overturning jet hits the water surface further ahead and another horizontal roller is created beneath the toe of the second jet. The horizontal rollers have an axis of rotation parallel to the wave and travel in the wave direction.

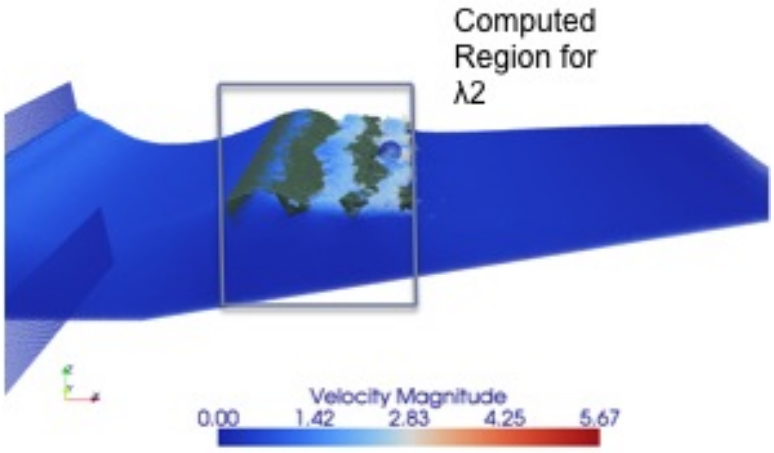

Figure 6.3: Broken water waves and the vortex structures detected by $\lambda_2 = -0.2$ isosurfaces at time $= t_p + \frac{4}{10}$, where t_p is the time when the first plunger hits the water surface

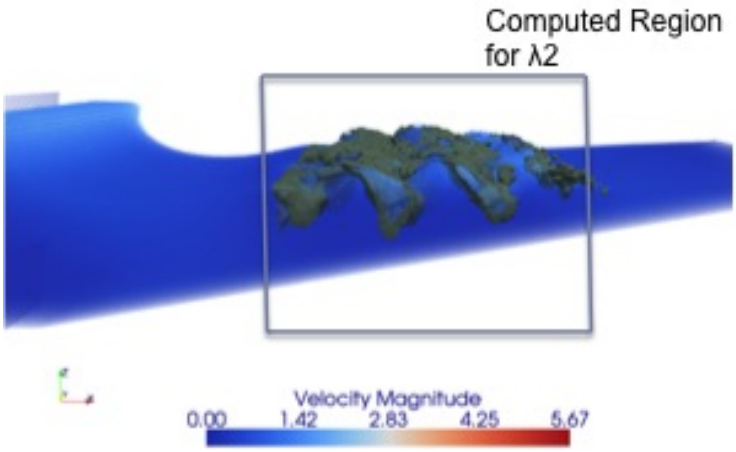

Figure 6.3: (continued)Broken water waves and the vortex structures detected by $\lambda_2 = -0.2$ isosurfaces at time $= t_p + \frac{8}{10}$, where t_p is the time when the first plunger hits the water surface

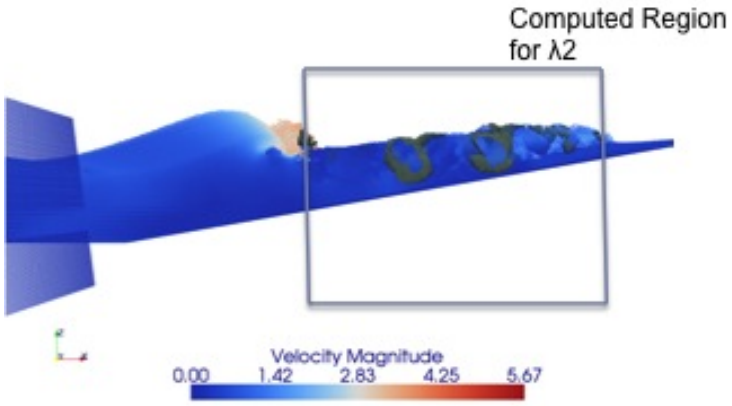

Figure 6.3: (continued)Broken water waves and the vortex structures detected by $\lambda_2 = -0.2$ isosurfaces at time $= t_p + \frac{12}{10}$, where t_p is the time when the first plunger hits the water surface

In order to study the rotations of the vortex structures at the toe of the plunging jet, a horizontal slide has been passed over the tank as is given in figure 6.4. Vorticity plot illustrates counter-rotating vertical vortices beneath the toe of the jet. These vertical structures are known as downbursts and were observed in Ting (2006, 2008) experiments.

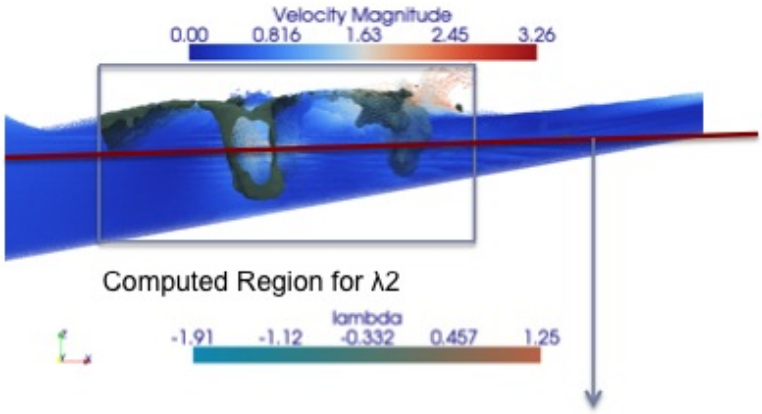

Figure 6.4: Vortex structures detected by by $\lambda_2 = -0.2$ isosurfaces at time $= t_p + \frac{28}{10}$, where t_p is the time when the first plunger hits the water surface.

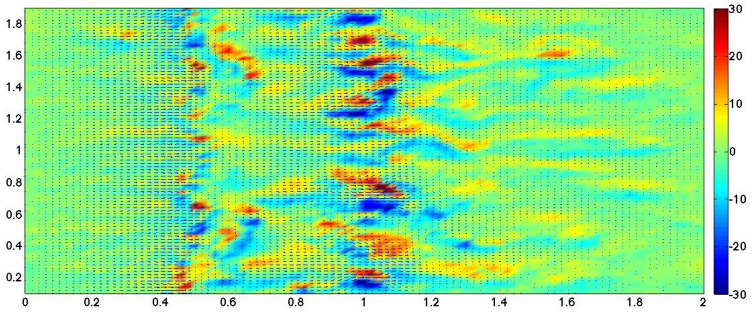

Figure 6.4: (Continued)Vorticity profile on a horizontal plane

Horseshoe structures are observed at the back of the broken waves. Figure 6.5 illustrates the vortex structures detected by isosurfaces of $\lambda_2 = -15$. These horse shoe structures have a spiral obliquely descending motion that will be investigated in the next section. The process of the generation of the horseshoe structures from the horizontal rollers are discussed in chapter 5. In general, three types of vortex structures are detected under broken periodic plunging waves:

1. Horizontal rollers with axis of rotation parallel to the waves,
2. Vertical counter-rotating vortex structures at the toe of the plunging jets (Known as downbursts),
3. Horseshoe structures at the back of the broken waves.

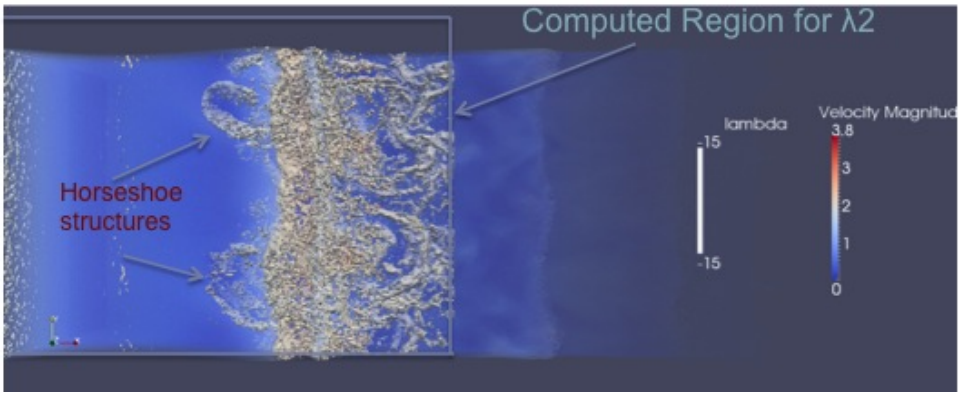

Figure 6.5: A snapshot of numerical results of periodic waves at time = 8.1 s (ninth wave period)

6.4 Particle trajectories

As mentioned in the previous section, a ball was located at the water surface close to the wavemaker to track the surface variations. figure 6.6 shows the ball trajectory as the wave breaks, hits the water surface ahead, splashes up, and overturns again.

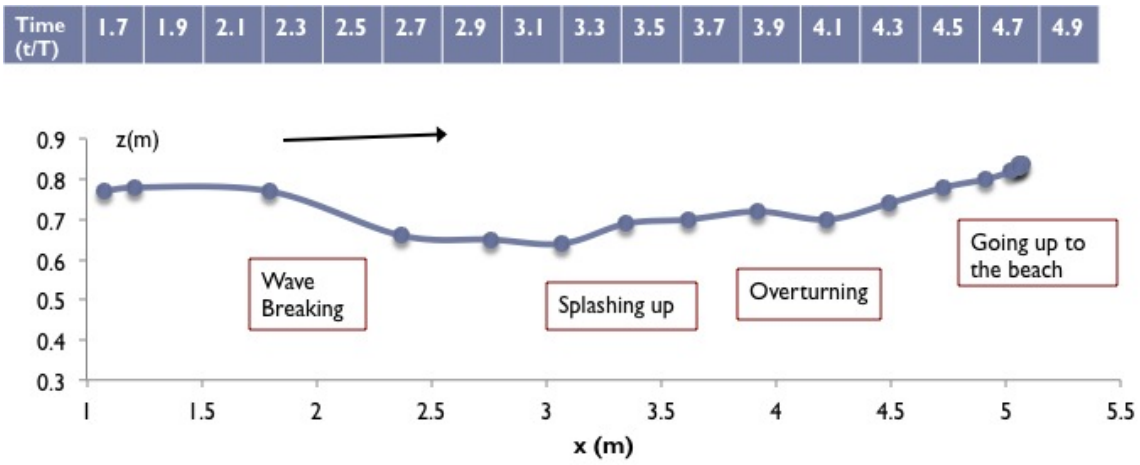

Figure 6.6: Ball trajectory

In addition, the trajectory of several particles at different locations of the tank was tracked as shown in figure 6.7. Particle tracking is started from $\frac{t}{T} = 1.7$ and continues until $\frac{t}{T} = 5.5$, where t is the time and T is the wave period. The particle tracking interval is equal $0.2\frac{t}{T}$. Particle A is selected at the half of the water depth (figure 6.7) at the back of the broken wave. As time passes, particle A creates a spiral obliquely descending motion. Particle B is chosen in the surf zone and at the half of the water column depth (figure 6.7). This particle presents a water particle motion under progressive waves. Particle C is chosen in the surf zone but close to

the water surface (figure 6.7). This particle experiences motion in y-direction as well as x-direction and z-direction. This motion can be related to the horizontal rollers. Particle C is chosen more close to the shoreline and at the water surface (figure 6.7). This particle moves offshore for a short distance but travels back to the shoreline and represents the water surface particles, which travel in onshore direction.

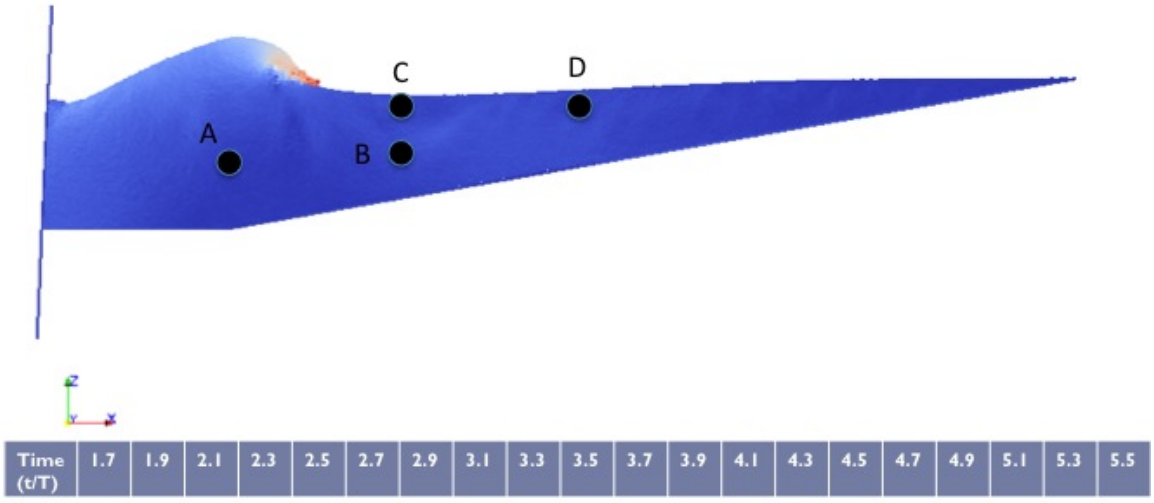

Figure 6.7: Water particle Trajectories

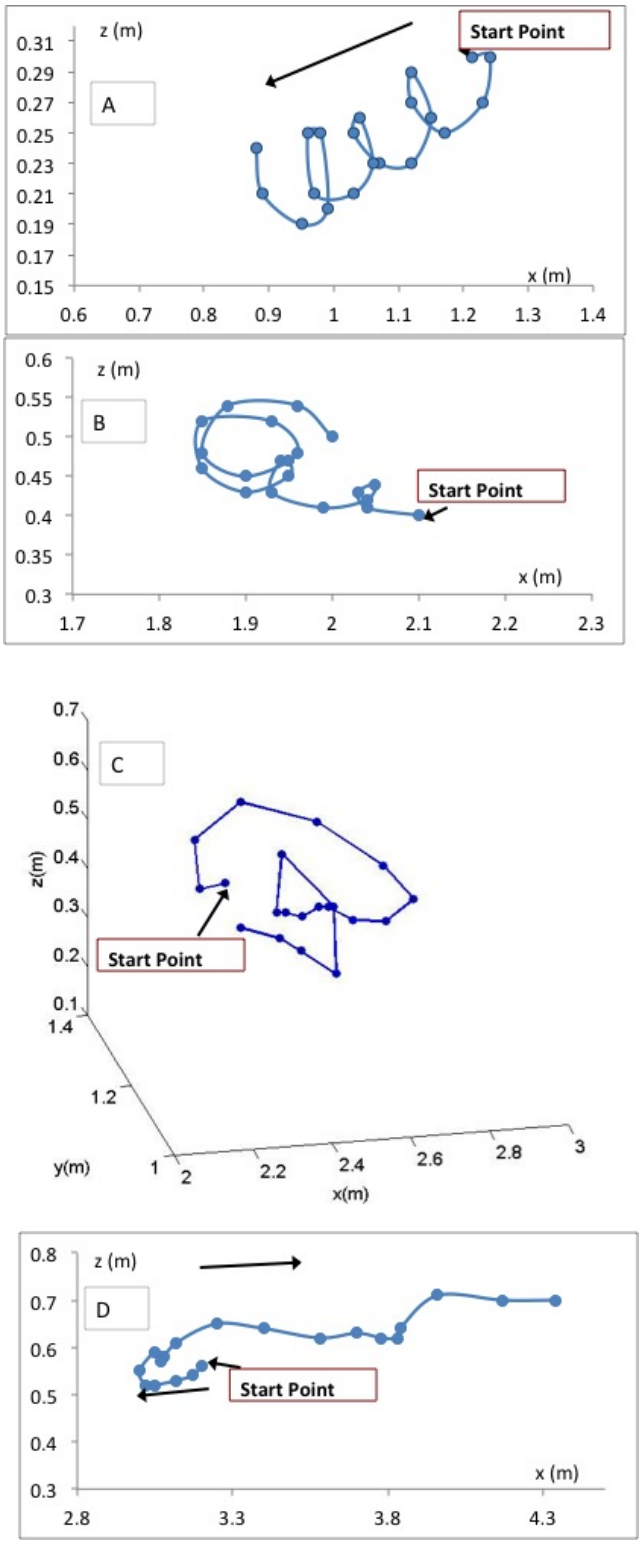

Figure 6.7: (Continued) Water particle Trajectories

Another set of water particle tracking is performed from $\frac{t}{T} = 5.7$ and continues until $\frac{t}{T} = 9.5$, where t is the time and T is the wave period. The particle tracking interval is equal $0.2\frac{t}{T}$. Figure 6.8 illustrates the initial position of the water particles and their motion during the particle tracking. Particle E, which is initially at the same position as particle A in figure 6.7, follows the same spiral obliquely descending motion. Particle F, which is located at the middle of the water depth and in the surf zone area experiences motion in y-direction as well as x-direction and z-direction. This motion can also be related to the horizontal rollers (similar to particle C in figure 6.7).

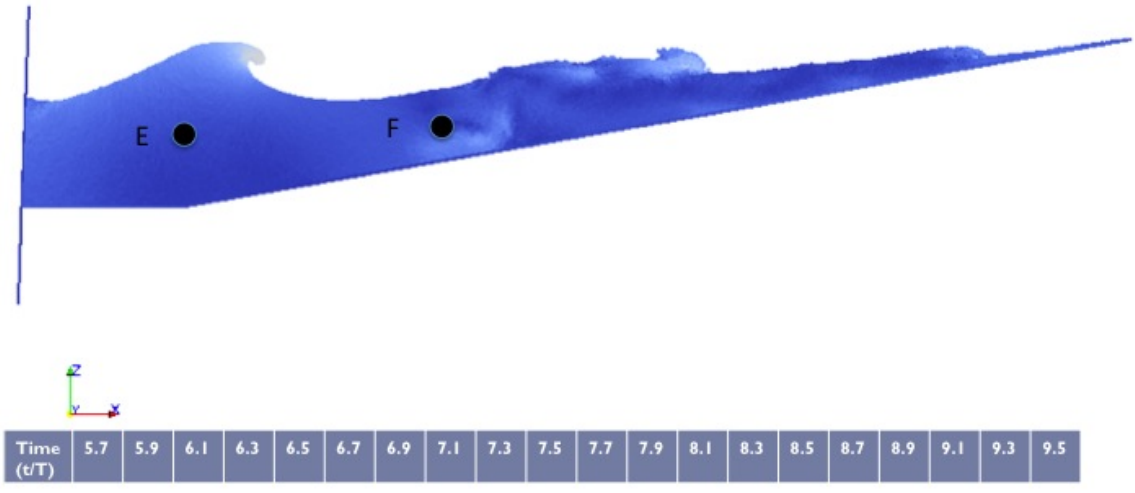

Figure 6.8: Water particle Trajectories at next wave period

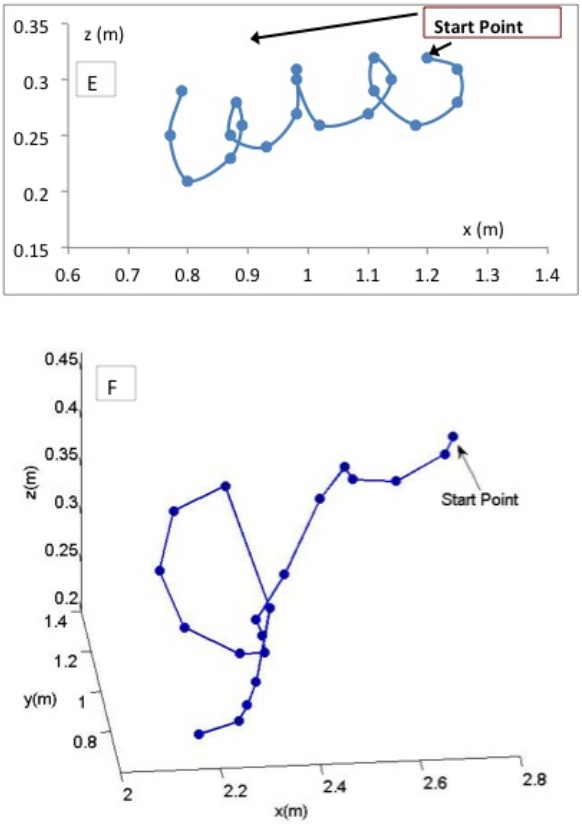

Figure 6.8: (Continued) Water particle Trajectories at next wave period

A massive particle tracking is performed to study the mixing of water layers due to the vortex structures and rotations. In this figure particles are numbered and colored according to the particle ID from 1 at the bottom right of the wave tank to 3240987 at the upper left of the tank. The Lagrangian nature of the SPH method enables us to perform a massive particle tracking and obtain the water layers mixing. Figure 6.9 illustrates the results of the particle ID tracking at two different times of 0 s and 4.9 s (fifth wave period). At time = 4.9 s the water layers are mixed in the nearshore area due to the vortex structures and three-dimensional rotations.

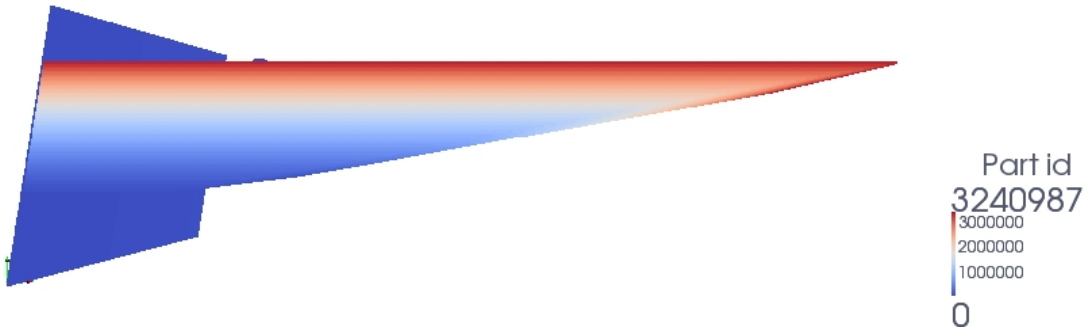

Figure 6.9: Massive Particle tracking at time =0 s

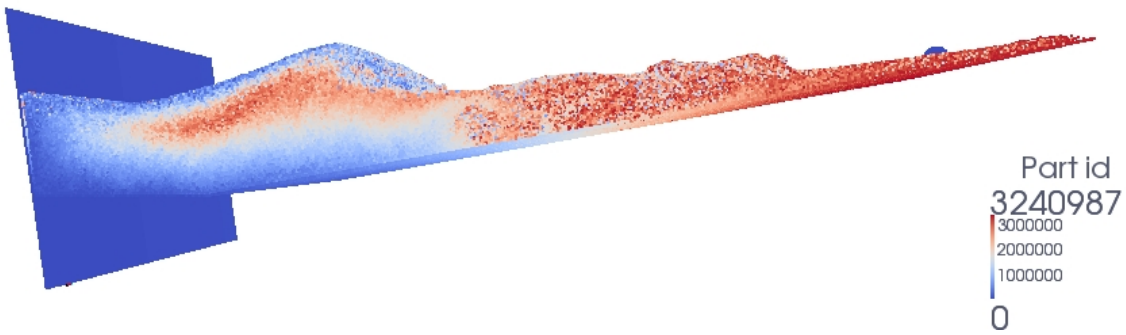

Figure 6.9: (Continued) Massive Particle tracking at time= 4.9 s (fifth wave period)

6.5 Conclusion

Periodic plunging waves are numerically modeled by three-dimensional GPUSPH model. Waves are generated by a flap wavemaker and propagate towards a plane beach with a slope of 1 in 5.6 m. Initial particle spacing is chosen to be equal to 0.01 m and about 3.5 million particles are used in the computation. Vortex structures, generated under broken waves, are detected using λ_2 method. Three types of vortex structures are observed: (1) Horizontal rollers generated beneath the broken waves with axis of rotations parallel to the wave. These vortex structures travel shoreward with the wave. (2) Vertical counter-rotating vortex structures at the toe of the plunging jets known as downbursts. These vortex structures can play a role in sand drift and sediment transportation. (3) Horseshoe structures generated at the back of the broken waves. Particle trajectory has been captured to study the fluid motion at different location of the wave tank. At the back of the wave spiral obliquely descending motion is observed that is related to the horseshoe structures. A floating ball is located at the water surface close to the wavemaker at time = 0 s and its trajectory has been tracked as the periodic waves are generated, propagated and break. The ball trajectory illustrates the cycle of overturning jets and splashing ups. At the end massive particle tracking is performed using particle ID and mixing of water layers due to the rotations and vortex structures is investigated.

Chapter 7

Conclusions and future works

7.1 Conclusions

This dissertation includes the three dimensional numerical modeling of the following coastal processes:

1. Rip current system due to the alongshore bed variation and related nearshore circulations

   Smoothed Particle Hydrodynamics (SPH), which is a mesh-free Lagrangian numerical method, is used to model a rip current system due to the alongshore bed variation. In the previous studies, SPH has been shown to model waves and wave breaking but in this study, we showed that SPH also models depth-integrated, time-averaged wave quantities, such as radiation stresses and mean water level changes, including wave setup at beaches. We also showed that SPH

is able to predict the wave-induced nearshore circulation system, including rip currents. The Lagrangian GPUSPH model, which uses graphics cards to do the heavy numerical calculations associated with SPH, is extended to calculate fluid parameters on fixed Eulerian nodes in addition to Lagrangian moving particles. This has been done to compare depth- and wave-averaged currents at a point to experimental data. The GPUSPH is used to model wave propagation in the surf zone and the associated wave-induced near-shore circulation over a bathymetry consisting of a bar intersected by a rip channel. The pattern of rip current and two cell circulations, one rotating anti-clockwise over the bar and the other rotating clockwise in the surface zone, is successfully modeled. The non-uniformity of breaking waves over the bar leads to different set-ups and elevation gradients on the submerged bar that force the circulation. As the waves are mostly breaking over the bar and there is almost no breaking in the rip channel, differences in the set-ups lead to a radiation stress gradient in cross-shore direction that acts as a driving force for the rip current. Different wave phenomena such as wave shoaling, wave breaking, diffraction-refraction pattern, wave-current interaction and higher harmonic generation in the surf zone were observed. The model is capable of capturing near-shore nonlinear surface waves as well as underlying rip current flow. Current field and wave-current interactions are investigated by looking at mean horizontal velocities profiles (depth- integrated and time-integrated) and vorticity field. Vorticity

generation over the bar results from non-uniformity of breaking waves caused by topography perturbations. Three-dimensional structure of flow is studied in different parts of the region. On the bar crest, three-dimensional effects lead to non-uniformity in the flow direction depending on the vertical position. Wave refraction-diffraction caused by underlying rip current, is also studied. Changes in different components of radiation stress and the resulting force are investigated and the role of alongshore variation of transverse component of radiation stress as a feeder for the rip current is illustrated. The effect of wave-current interaction on the increase of wave number and the wave height over the rip channel is given. The model results are compared with the observations of laboratory experiments of Drønen et al. (2002) on rip current generated in a region of a single bar and a rip channel. Good agreement is obtained between numerical results and experimental data in terms of mean velocity distribution, mean surface elevation, and three-dimensional development of the currents. The laboratory experiments of Drønen et al. (2002) were chosen since the experimental set-up was numerically feasible to be modeled by the 3D SPH numerical method. In addition, 3D structure of flow is also studied in these laboratory experiments.

2. Solitary water waves both spilling and plunging in the surf zone and the three-dimensional vortex structures generated under broken water waves

   Smoothed Particle Hydrodynamics (SPH) is used to model solitary water waves

both spilling and plunging in the surf zone region. Numerical results are compared with the experimental measurements of Ting (2006) including water surface profiles at different locations of the tank, mean horizontal velocity, and turbulent velocities. Vortex structures under the broken waves were detected using λ_2 method. Unique organized vortical structures were observed at the back of the broken spilling wave in the form of reversed horseshoe(hairpin) vortices. These structures have reversed head and legs position in comparison to the horseshoe structures observed in a turbulent boundary layer. The reversed horseshoes generate downwelling motion (sweep event) with their head and two counter-rotating legs. In the previous studies obliquely descending motions were reported at the back of the broken waves but in our study for the first time, we investigated and characterized the vortex structures as reversed horseshoe structures. The legs of the reversed horseshoe structures appear to be the obliquely descending eddies that Nadaoka (1989) and Watanabe (2005) denoted in their studies. The evolution process of generation, transportation, and attenuation of reversed horseshoe structures has been investigated. As the time passes, the reversed horseshoe structure travels downward to the deeper layers of the water column and spreads the turbulence toward the bottom. As the horseshoe travels downward, the intensity of the turbulent momentum flux decreases due to the spreading and dissipation. In the case of a plunging solitary wave, vortex structures are generated under the broken wave but no reversed

horseshoe structure is observed at the back of the broken wave.

3. Periodic plunging water waves in the surf zone and the three-dimensional vortex structures generated under broken water waves

   Smoothed Particle Hydrodynamics (SPH) is used to model periodic plunging water waves. Vortex structures, generated under broken waves, are detected using λ_2 method. Three types of vortex structures are observed: (1) Horizontal rollers generated beneath the broken waves with axis of rotations parallel to the wave. These vortex structures travel shoreward with the wave. (2) Vertical counter-rotating vortex structures at the toe of the plunging jets known as downbursts. These vortex structures can play a role in sand drift and sediment transportation. (3) Reversed horseshoe structures generated at the back of the broken waves. Particle trajectory has been performed to study the fluid motion at different location of the wave tank. At the back of the wave spiral obliquely descending motion is observed that is related to the reversed horseshoe structures.

7.2 Future works

Numerical modeling of the rip current system has been inspired by experimental study of Drønen et al. (2002), which represented one-half of a rip current system, represented by two bars with a rip channel in between (using symmetry about the

sidewalls). In this set-up, the two shore-normal sidewalls of the wave tank correspond to the centerline of rip channel and centerline of one of the bars. In terms of mean velocity profiles and mean surface elevations, the experimental data were only available from the figures in the original article. For the future studies, using the latest techniques of GPU programming and multi-GPU programming, 3D SPH numerical modeling of rip current experiment set-up of Haller et al. (1997) or similar experiments with more available experimental data are recommended. The suggested future works can be summarized as:

- Perform a 3D numerical study of the whole rip current system using the latest techniques of GPU programming and multi-GPU programming and compare the numerical results with more available experimental data. Our numerical study was performed on an idealized bathymetry that models half of a periodic bar/rip channel system. This bathymetry is chosen due to the computational limitations but in future using the multi-GPU programming technique, the whole bar/rip channel system can be studied.

- Study the effect of distance between the sand bars on the rip current generation and the 3D structure of flow in the rip current system.

- Study the effect of wave parameters such as wave height on the intensity of the rip current and the 3D vertical variation of rip current flow.

In terms of vortex structures detected under the broken water waves the following future works are suggested:

- Study the size of the reversed horseshoe structures and the effect of wave parameters on the frequency and size of the reversed horseshoe structures.
- Study the effect of bed bathymetry and water depth on the generation and evolution of the reversed horseshoe structures.
- Perform a numerical study of previously occurred tsunami waves using the latest techniques of GPU programming and multi-GPU programming and study the influence of vortex structures on the safety of vessels and other structures located in the surf zone region.

Bibliography

[1] Aagaard, T., Greenwood, B., and Nielsen, J. (1997). "Mean currents and sediment transport in a rip channel." Journal of Marine Geology, 140, 25-45.

[2] Alfredsson, P. H., and Johansson, A. V., (1984). "On the detection of turbulence-generating events." Journal of Fluid Mechanics, 139, 325-345.

[3] Amicarelli, A., Fang, L., Marongiu, J., Leboeuf, F., Caro, J., and Leduc, J. (2010)."SPH truncation error in 3D simulation." Proceeding of 5th International SPHERIC Workshop, Manchester, UK, 1-8.

[4] Arthur, R. S. (1962). "A note on the dynamics of rip currents." Journal of Geophysical Research, 67(7), 2777-2779.

[5] Banner M. L., and Peregrine, D. H. (1993). "Wave Breaking in deep water." Annual Review of Fluid Mechanics, 25, 373-379.

[6] Battjes, J. A., (1988). "Surf-zone dynamics." Annual Review of Fluid Mechanics, 20, 257-293.

BIBLIOGRAPHY

[7] Bowen, A. J., and Inman, D. (1969a). "Rip currents 1. Theoretical investigation." Journal of Geophysical Research, 74(23), 5467-5478.

[8] Bowen, A. J., and Inman, D. (1969b). "Rip currents 2. Laboratory and field observations." Journal of Geophysical research, 74(23), 5479-5490.

[9] Brander, R. W. (1999). "Field observations on the morphodynamic evolution of a low-energy rip current system." Journal of Marine Geology, 157, 199-217.

[10] Brocchini M., Kennedy A., Soldini L., and Mancinelli A. (2004) "Topographically-controlled, breaking wave-induced macrovortices. Part 1. Widely separated breakwaters." Journal of Fluid Mechanics, 507, 289-307.

[11] Bhler, O., and Jacobson, TE. (2001). "Wave-driven currents and vortex dynamics on barred beaches." Journal of Fluid Mechanics, 449, 313-339.

[12] Chang, K., Liu, P. L. F., (1998). "Velocity, acceleration and vorticity under a breaking wave." Physics of Fluids, 10(1), 327-329.

[13] Chang, K., Liu, P. L. F., (1999). "Experimental investigation of turbulence generated by breaking waves in water for intermediate depth." Physics of Fluids, 11(11), 3390-3400.

[14] Chen, Q., Dalrymple, R. A., Kirby, J., Kennedy A., and Haller M. (1999). "Boussinesq modeling of a rip current system." Journal of Geophysical Research, 104(C9), 20617-20637.

BIBLIOGRAPHY

[15] Christensen, E. D., and Deigaard, R. (2001). "Large eddy simulation of breaking waves." Coastal Engineering, 42, 53-86.

[16] Christensen, E. D. (2006). "Large eddy simulation of spilling and plunging breakers." Coastal Engineering, 53, 463-485.

[17] Cleary, P. W., and Monaghan, J. J. (1999). "Conduction modeling using Smoothed Particle Hydrodynamics", Journal of Computational Physics, 148, 227-264.

[18] Colagrossi, A., and Landrini, M. (2003). "Numerical simulation of interfacial flows by smoothed particle hydrodynamics." Journal of Computational Physics, 191, 448-475.

[19] Cox, D. T., and Kobayashi, N., (2000). "Identification of intense, intermittent coherent motions under shoaling and breaking waves." Journal of Geophysical Research, 105, 14223-14236.

[20] Cox, D. T., and Anderson, S. L., (2001). "Statics of intermittent surf zone turbulence and observation of large eddies using PIV." Coastal Engineering Journal, 43, 121-131.

[21] Cox, D. T., and Shin, S., (2003). "Laboratory measurements of void fraction and turbulence in the bore region of surf zone waves." Journal of Engineering Mechanics, ASCE, 129, 1197-1205.

BIBLIOGRAPHY

[22] Dalrymple, R. A., and Knio, O. (2001). "SPH modeling of water waves." Proc. of Coastal Dynamics, 779-787.

[23] Dalrymple, R. A. (1975). "A mechanism for rip current generation on an open coast." Journal of Geophysical Research, 80(24), 3485-3487.

[24] Dalrymple, R. A. (1978). "Rip currents and their causes." Proc. 16th Conference on Coastal Engineering, Hamburg, 1414-1427.

[25] Dalrymple, R. A., and Lozano, C. J. (1978). "Wave-current interaction models for rip currents." Journal of Geophysical Research, 83(C12), 6063-6071.

[26] Dalrymple, R. A., Knio, O., Cox, D. T., Gómez-Gesteira, M., and Zou, S. (2002). "Using a Lagrangian particle method for deck overtopping." Proc. of Waves, ASCE., 1082-1091

[27] Dalrymple, R. A., and Rogers, B. D. (2006a). "Numerical modeling of water waves with SPH method." Coastal Engineering, 53, 141-147.

[28] Dalrymple, R.A. and Rogers, B. D. (2006b). "A note on wave celerities on a compressible fluid." In Proceeding 30th International Conference on Coastal Engineering, World Scientific Press, 3-13.

[29] Dalrymple, R. A., MacMahan J., Reniers A., and Nelko V. (2011). "Rip currents." Annual Review of Fluid Mechanics, 43, 551-581.

BIBLIOGRAPHY

[30] Drønen, N., Karunarathna, H., Fredsoe, J., Sumer, B., and Deiggard, R. (2002). "An experimental study of rip channel flow." Coastal Engineering, 45, 223-238.

[31] Gingold, R. A., Monaghan, J. J. (1977) "Smoothed particle hydrodynamics: Theory and application to non-spherical stars." Monthly notices of the royal astronomical society, 181, 375-389.

[32] Goring, D., Raichlen, F., (1980). "The generation of long waves in the laboratory." Coastal Engineering, 763-783.

[33] Gómez-Gesteira, M., and Dalrymple, R. A. (2004). "Using a three-dimensional Smoothed Particle Hydrodynamics method for wave impact on a tall structure." Journal of Waterway, Port, Coastal and Ocean Engineering, ASCE, 130(2) 63-69.

[34] Gómez-Gesteira, M., Cerqueiro, D., Crespo, C., and Dalrymple, R. A. (2005). "Green water overtopping analyzed with a SPH model." Ocean Engineering, 32, 223-238.

[35] Green, S. I., (1995). "Fluid Vortices." Kluwer Academic Publishers.

[36] Haas, K. A., and Svendsen, A. (2002). "Laboratory measurements of the vertical structure of rip currents." Journal of Geophysical Research, 107(C5), 15-1, 15-19.

[37] Haas, K. A., Svendsen, A., Haller, M. C., and Zhao, Q. (2003). "Quasi-three-dimensional modeling of rip current systems." Journal of Geophysical Research, 108(C7), 10-1, 15-21.

BIBLIOGRAPHY

[38] Haller, M., Dalrymple, R. A., and Svendsen, I. (1997). "Rip channels and nearshore circulation: experiments." ASCE, 594-603.

[39] Haller, M. C. and Dalrymple, R. A. (2001). "Rip current instabilities." Journal of Fluid Mechanics, 433, 161-192.

[40] Hérault, A., Bilotta, G., and Dalrymple, R. A. (2010). "SPH on GPU with CUDA." Journal of Hydraulic Research, 48, 74-79.

[41] Hérault, A., Bilotta, G., Vicari, A., Rustico, E., and Negro, C. D. (2011) "Numerical simulation of lava flow using a GPU SPH model." Annals of Geophysics, 54(5), 600-620.

[42] Huschke, R. E. (1959). "Glossary of Meteorology." American Meteorological Society, Boston, Massachusetts, 484.

[43] Hussain A. K. M. (1986). "Coherent structures and turbulence." Journal of Fluid Mechanics, 173., 303-356.

[44] Jeong J., and Hussain F., (1994). "On the identification of a vortex." Journal of Fluid Mechanics, 285, 69-94.

[45] Johnson, G. R., Stryk R. A., and Beissel S. R. (1996). "SPH for high velocity impact computations." Computer methods in applied mechanics and engineering, 139, 347-373.

BIBLIOGRAPHY

[46] Kajtar J., Monaghan J. (2007). "SPH simulations of swimming linked bodies.", Journal of Computational Physics, 227, 8568-8587

[47] Kennedy, A., Brocchini, M., Soldini L., and Gutierrez E. (2006). "Topographically-controlled, breaking wave-induced macrovortices. Part 2. Changing geometries." Journal of Fluid Mechanics, 559, 57-80.

[48] Kim, J., and Moin, P., (1986). "The structure of the vorticity field in turbulent channel flow. Part 2. Study of ensemble-averaged fields." Journal of Fluid Mechanics, 162, 339-363.

[49] Landrini M., Colarossi A., Greco M., and Tuline M. P., (2007). "Gridless simulation of splashing processes and near-shore bore propagation." Journal of Fluid Mechanics, 591, 183-213.

[50] Li, L., and Dalrymple, R. A., (1998). "Instabilities of the undertow." Journal of Fluid Mechanics." 369, 175-190.

[51] Lippman, T. C., and Holman, R. A. (1990). "The spatial and temporal variability of sand bar morphology." Journal of Geophysical Research, 95(C7), 11,575-11,590.

[52] Liu, G. R., and Liu, M. B. (2003). "Smoothed Particle Hydrodynamics, a mesh free particle method." World Scientific Publishing Co. Pte. Ltd.

[53] Lo, E. Y. M., and Shao S. (2002). "Simulation of near-shore solitary wave mechanics by an incompressible SPH method." Applied Ocean Research, 24, 275-286.

BIBLIOGRAPHY

[54] Longuet-Higgins, M. S., and Stewart, R. W. (1960). "Changes in the form of short gravity waves on long waves and tidal currents." Journal of Fluid Mechanics, 8, 565-583.

[55] Longuet-Higgins, M. S., and Stewart, R. W. (1964). "Radiation stresses in water waves; a physical discussion, with application." Deep-Sea Research, 11, 529-562.

[56] Longuet-Higgins M. (1995). "On the disintegration of the jet in a plunging breaker." Journal of Physical Oceanography, 25, 2458-2462.

[57] Lucy, L.B. (1977). "A numerical approach to the testing of the fission hypothesis." Astronomical Journal, 82, 1013-1024.

[58] Lushine, J. B. (1991). "A study of rip current drownings and related weather factors." National Weather Service Forecast Office, Miami, Florida.

[59] MacMahan, J. H., Thornton, Ed B., Stanton, T. P., and Reniers Ad. J. H. M. (2005). "RIPEX: Observations of a rip current system." Journal of Marine Geology, 218, 113-134.

[60] MacMahan, J., Brown, Jef., Brown, Jen., Thronton, Ed., Reniers, Ad., Stanton, T., Henriquez, M., Gallagher, E., Morrison, J., Austin, M. J., Scott, T. M., and Senechal, N. (2010). "Mean Lagrangian flow behavior on an open coast rip-channeled beach: A new perspective." Journal of Marine Geology, 268, 1-15.

[61] Madsen, P. A., Sørensen, O. R., and Schäffer, H. A. (1997). "Surf zone dynamics

simulated by a boussinesq type model. Part 1. Model description and cross-shore motion of regular waves." Journal of Coastal Engineering, 32, 255-287.

[62] Marrone, S., Colagrossi A., Touze, D. Le, and Graziani G. (2010). "Fast free-surface detection and level-set function definition in SPH solvers." Journal of Computational Physics, 229, 3652-3663.

[63] Matsunaga, N., Takehara, K., and Awaya, Y., (1988). "Coherent eddies induced by breakers on a sloping bed." Proceeding of 21st Coastal Engineering Conference, ASCE, 234-245.

[64] Matsunaga, N., Takehara, K., and Awaya, Y., (1994). "The offshore vortex train." Journal of Fluid Mechanics, 276, 113-124.

[65] Mckenzie, P. (1958). "Rip current systems." The Journal of Geology, 66, 103-113.

[66] Mei, C. C., and Ünlüata U. (1972). "Harmonic generation in shallow water waves." Waves on Beaches and Resulting Sediment Transport, 181-202.

[67] Melville, W. K., Veron, F., and White, C. J., (2002). "The velocity field under breaking waves: coherent structures and turbulence." Journal of Fluid Mechanics, 454, 203-233.

[68] Meneveau C., Lund, T. S., and Cabot, W. H. (1996) "A Lagrangian dynamic subgrid-scale model of turbulence." Journal of Fluid Mechanics, 319, 353-385.

[69] Monaghan, J. J., and Gingold, R. A. (1983) "Shock simulation of multi-phase flow." Computer Physics Communication, 87, 225-235.

[70] Monaghan, J. J., and Lattanzio, J. C. (1985) "A refined particle method for astrophysical problems." Astronomy and astrophysics, 149, 135-143.

[71] Monaghan, J. J. (1992) "Smoothed Particle Hydrodynamics." Annual review of astronomical and astrophysics, 18, 233-237.

[72] Monaghan, J. J., (1994). "Simulating free surface flows with SPH." Computational Physics, 110, 399-406.

[73] Monaghan, J. J., and Kos, A. (1999). "Solitary waves on a certain beach." Journal of Waterway, Port, Coastal and Ocean Engineering, 145-154.

[74] Monaghan, J. J., and Kos, A., (2000). "Scott Russells wave generator." Physics of Fluids, 12(3), 622-630.

[75] Monaghan, J. J., and Kos, A., Issa, N. (2003). "Fluid motion generated by impact." Journal of Waterway, Port, Coastal and Ocean Engineering, 129(6) 250-259.

[76] Monaghan, J. J. (2005). "Smoothed Particle Hydrodynamics." Reports on Progress in Physics, 68, 1703-1759.

[77] Monaghan J. J., and Kajtar J. (2009) "SPH particle boundary forces for arbitrary boundaries." Computer Physics Communications, 180, 1811-1820.

BIBLIOGRAPHY

[78] Monaghan, J. J., (2012). "Smoothed Particle Hydrodynamics and its diverse applications." Annual Review of Fluid Mechanics, 44, 323-346.

[79] Morris, J. P. (1996). "Analysis of smoothed particle hydrodynamics with applications." Ph.D. thesis, University of Monash, Melbourne, Australia.

[80] Morris, J. P., Fox, P. J., and Zhu, Y. (1997). "Modeling low reynolds number incompressible flows using SPH." Journal of Computational Physics, 136, 214-226.

[81] Nadaoka, K., Hino M., and Koyano, Y., (1989). "Structure of the turbulent flow field under breaking waves in the surf zone." Journal of Fluid Mechanics, 204, 359-387.

[82] Noda E. K. (1974). "Wave-induced nearshore circulation." Journal of Geophysical Research, 79, 4097-4106.

[83] Perlin M., J. He (1996). "An experimental study of deep water plunging breakers." Physics of fluid, 8, 2365-2374.

[84] Randles P. W., and Libersky L. D. (1996). "Smoothed particle hydrodynamics some recent improvements and applications." Computer Methods in Applied Mechanics and Engineering, 138, 375-408.

[85] Reniers, A. J. H. M., MacMahan, J. H., Beron-Vera, F. J., and Olascoaga, M. J. (2010). "Rip-current pulses tied to Lagrangian coherent structures." Journal of Geophysical Research, 37, 1-5.

BIBLIOGRAPHY

[86] Sénéchal, H., Dupuis, H., Bonneton P. (2004). "Preliminary hydrodynamic results of a field experiment on a barred beach, Truc Vert beach on October 2001." Ocean Dynamics, 54(3-4), 408-414(7).

[87] Shepard, D. (1968). "A two dimensional function for irregularly spaced data." Proceeding of 23rd ACM National Conference, New York, USA, 517-524.

[88] Shepard, F. P., Emery K. O., and Fond E. C. La. (1941). "Rip currents: A process of geological importance." The Journal of Geology, 49, 337-369.

[89] Sénéchal, H., Dupuis, H., Bonneton P. (2004). "Preliminary hydrodynamic results of a field experiment on a barred beach, Truc Vert beach on October 2001." Ocean Dynamics, 54(3-4), 408-414(7).

[90] Short, A.D., and Brander, R. W. (1999). "Regional variations in rip density." Journal of Coastal Research, 15, 813-822.

[91] Smagorinsky, J. (1963). "General circulation experiments with the primitive equations. I. The basic experiment." Weather Bureau, 91(3), 99-164.

[92] Smith, J. A., and Largier, J. L. (1995). "Observations of nearshore circulation: Rip currents." Journal of Geophysical Research, 100, 10,967-10,975.

[93] Sonu, C. J. (1972). "Field observations of nearshore circulation and meandering currents." Journal of Geophysical Research, 77, 3232-3247.

[94] Sou, I. M., Cowen, E. A., Liu, P. L. F., (2010). "Evolution of the turbulence structure in the surf and swash zones." 644, 193-216.

[95] Svendsen, I. A., (1987). "Analysis of surf-zone turbulence." Journal of Geophysical Research, 92(C5), 5115-5124.

[96] Ting, F. C. K., and Kirby, J. T., (1994). "Observation of undertow and turbulence in a laboratory surf zone." Coastal Engineering, 24, 52-80.

[97] Ting, F. C. K., and Kirby, J. T., (1995). "Dynamics of surf zone turbulence in a strong plunging breaker." Coastal Engineering, 24, 177-204.

[98] Ting, F. C. K., and Kirby, J. T., (1996). "Dynamics of surf zone turbulence in a spilling breaker." Coastal Engineering, 27, 131-160.

[99] Ting, F. C. K., (2006). "Large-scale turbulence under a solitary wave." Coastal Engineering, 53, 441-462.

[100] Violeau, D. (2012). "Fluid mechanics and the SPH method, theory and applications." Oxford University Press.

[101] Wallace, J. M., Eckelmann, H., and Brodkey, R. S., (1972). "The wall region in turbulent shear flow." Journal of Fluid Mechanics, 54, 39-48.

[102] Watanabe and Y., Saeki, H., (1999). "Three-dimensional large eddy simulation of breaking waves." Coastal Engineering, 41, 281-301.

BIBLIOGRAPHY

[103] Watanabe, Y., Saeki, H., and Hosking, R. J., (2005). "Three-dimensional vortex structures under breaking waves." Journal of Fluid Mechanics, 545, 291-328.

[104] Wei, G, and Kirby, J. T. (1995). "Time-dependent numerical code for extended Boussinesq equations." Journal of Waterway, Port, Coastal and Ocean Engineering, 121, 251-61.

[105] Wendland, H. (1995). "Piecewise polynomial, positive definite and compactly supported radial functions of minimal degree." Advances in Computational Mathematics, 4, 389-396.

[106] Willmart, W. W., and Lu, S. S., (1972). "Structure of the Reynolds stress near the wall." Journal of Fluid Mechanics, 55, 65-92.

[107] Wright, L. D., and Short, A. D. (1984). "Morphodynamic variability of surf zones and beaches: a synthesis." Marine Geology, 56, 93-118.

[108] Yang, D., Shen, L., (2009). "Charactristics of coherent vortical structures in turbulent flows over progressive surface waves." Physics of Fluids, 21, 125106, 1-23.

[109] Yu, J., Slinn D. (2003). "Effects of wave-current interaction on rip currents." Journal of Geophysical Research, 108(C3), 33-1:33-19.

[110] Yoshizawa, A. (1986). "Statistical theory for compressible turbulent shear flows, with application to subgrid modeling." Physics of Fluids, 29 (7), 2152-2164.

Vita

Rozita Jalali Farahani received the B.S. degree in Civil Engineering (Water-resource Engineering) from Iran Science & Technology University (IUST), Tehran, Iran on 2001. After that she worked as a coastal/hydraulics engineer for four years and became interested to deepen her knowledge of coastal processes and fluid dynamics. She went back to school and received M.Sc. in Civil Engineering (Hydraulics Engineering) from Sharif University of Technology, Tehran, Iran on 2007, and enrolled in the Civil Engineering (Coastal Engineering) Ph.D. program at Johns Hopkins University on 2007. She also received the M.S.E. degree in Mechanical Engineering from Johns Hopkins University on 2012. Her research focuses on three dimensional numerical modeling of free surface flows and coastal processes using GPU parallel programming.